MATEMATICKO-FYZIKÁLNÍ
FAKULTA
Univerzita Karlova

# MASTER THESIS

Kristián Šalata

## Structure parameters of martensite in Ti alloys modified by presence of oxygen atoms

Department of Physics of materials

Supervisor of the master thesis: RNDr. Dalibor Preisler

Study programme: Physics

Specialization: Physics of Condensed Matter and Materials

Prague 2023

I declare that I carried out this master thesis independently, and only with the cited sources, literature and other professional sources.

I understand that my work relates to the rights and obligations under the Act No. 121/2000 Coll., the Copyright Act, as amended, in particular the fact that the Charles University has the right to conclude a license agreement on the use of this work as a school work pursuant to Section 60 paragraph 1 of the Copyright Act.

In Prague date 2.5.2023 Kristián Šalata

First of all, I would like to thank my supervisor, Dalibor Preisler, who showed me all available experimental methods and was always at hand in any case. I could not have undertaken this journey without his help. Furthermore, I want to thank Jiří Kozlík and Lukáš Horák for their help in creating a script for reciprocal map indexing. It was a long and exhausting journey, but the destination was successfully reached.

I would like to thank Prof. Václav Holý for his valuable advice in solving the crystal structure. I would also like to extend my appreciation to my colleague, Lucia Bajtošová, for her assistance with the measurement of TEM and preparation of the samples. Finally, I am grateful to my family for their unwavering support throughout my studies and to Antonín Boháč for providing beautiful pictures and a steady supply of Indian cuisine."

Title: Structure parameters of martensite in Ti alloys modified by presence of oxygen atoms

Author: Kristián Šalata

Department / Institute: Department of Physics of Materials

Supervisor of the master thesis: RNDr. Dalibor Preisler, Department of physics of materials

Abstract:

This study discusses the influence of beta-stabilizing elements and oxygen on the martensitic structure in metastable β titanium alloys. The introduction describes the crystallographic nature of the metastable martensitic phase and its relation to the bcc and hcp phases. Additionally, the study presents the results of a measurement of transmission X-ray diffraction, by which we determined two components involved in the formation of the martensitic phase - shear and shuffle. The analysis of the first component, shear, was carried out quantitatively using lattice parameters. The second component, shuffle, was analyzed by determining the crystal structure of the martensitic phase and all atomic positions. Finally, the study also demonstrates a HRTEM measurement with subsequent image processing to confirm or disprove the presence of O' phase nanodomains.

Keywords: Titanium alloys, Crystal structure, Martensite, Oxygen interstitials

# Content

# 1 Introduction

## 1.1 Comparison of titanium with other metals

Titanium alloys are a group of perspective structural materials. Due to their high specific strength and exceptional corrosion resistance, titanium alloys have been widely used in engineering, aerospace, automotive and biomedical fields [1]. A simple comparison of Ti with other commonly used structural metals (Table 1) shows some of their main advantages and disadvantages. As we can see, titanium has half the density of iron and nickel, but almost twice that of aluminium. Its melting point is the highest among the selected elements, which makes it suitable for high-temperature applications. Furthermore, it has very good corrosion resistance due to a stable protective surface film, which consists basically of $TiO_2$. This thin oxide film passivates titanium as long as the integrity of the film is maintained and thus can be used in the chemical industry [2]. On the other hand, titanium and titanium alloys are very expensive compared to iron or aluminium alloys, which is the main problem behind their global use.

Table 1. Selected physical properties of titanium compared to competitor metals [1]

| | Ti | Al | Fe | Ni |
|---|---|---|---|---|
| Density [g/cm$^3$] | 4.5 | 2.7 | 7.9 | 8.9 |
| Melting point [°C] | 1670 | 660 | 1538 | 1455 |
| Thermal conductivity [W/mK]* | 15-22 | 221-247 | 68-80 | 72-92 |
| Elastic modulus [GPa] | 115 | 72 | 215 | 200 |
| Reactivity with oxygen | high + | high | low | low |
| Corrosion resistance | high + | high | low | medium |
| Metal price | high + | medium | low | high |

## 1.2 General applications of titanium alloys

Because of their pros and cons, titanium alloys are mostly used in applications where material properties are more important than price. These include for example biomedical field, where titanium alloys are used for the production of joint implants, surgical instruments or stents that prevent the clogging of blood vessels. The main advantage of titanium alloys here is their biocompatibility, thanks to which they can be used in a biological environment and, unlike iron alloys, are inert to the surrounding

environment. The second place that makes extensive use of the excellent ratio between mechanical properties and low density is the aerospace industry. Ti alloys are mainly used for the production of airframe structures, such as landing gears, window frames, springs and some parts of gas turbine engines, for example, blades. Due to the stable nature of titanium, it is also suitable for the storage of reactive chemicals in factories or as a material for high-pressure tubes. The less important part but not least consists of jewellery, sports equipment, and application in the automotive industry, where the main drawback is high price and difficulty of processing.

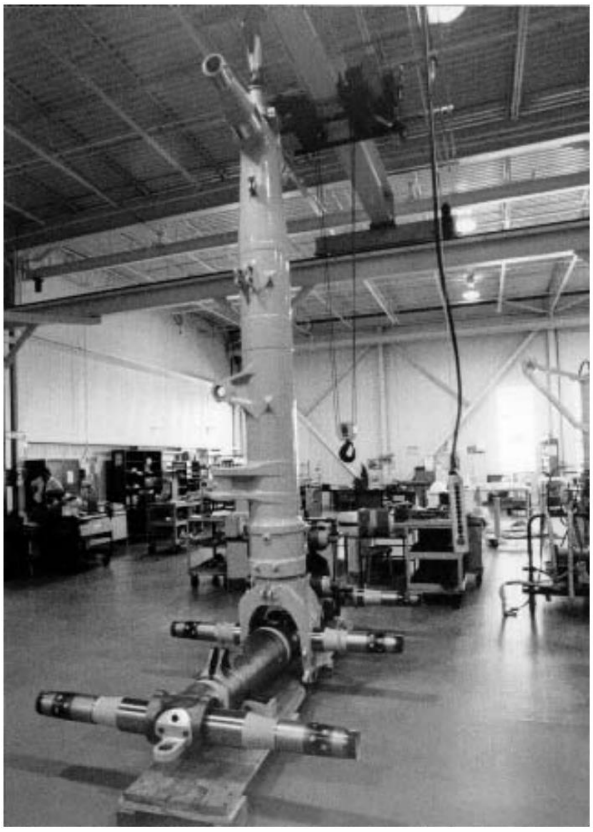

Figure 1-1 Aircraft landing gear of the Boeing 777, from [2]

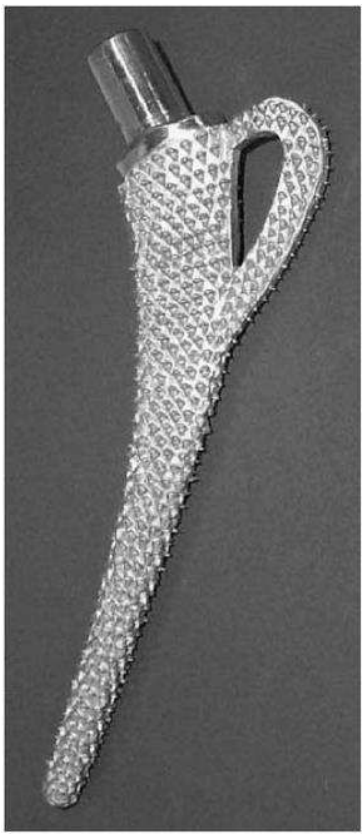

Figure 1-2 Hip joint stem made from Ti6Al4V alloy, from [2]

## 1.3 Production of titanium

In 1791, William Gregor, a clergyman and geologist, made the discovery of titanium in Cornwall, Great Britain. He identified a new element in ilmenite, which he found as an inclusion in a mineral in black sand near a stream. Gregor became aware of the element's presence when he noticed the sand was drawn to a magnet. Titanium can be found in the Earth’s crust as abundant element with a concentration around 0.57

wt.%. Despite its prevalence, it is not found in its pure form but rather as a component in minerals such as rutile ($TiO_2$) or previously mentioned ilmenite ($FeTiO_3$), with the latter being the primary source of titanium ore. Its high cost in the market is mainly due to the complicated and intensive processing required to extract pure metal from the titanium ore.

Its extraction from its various ores was a big issue and is currently still a laborious and costly process. The reduction process must be different than in case of iron smelting, due to the fact that titanium combines with carbon and creates titanium carbide. The first successful isolation of titanium was done in 1910 by Matthew A. Hunter by heating $TiCl_4$ with sodium under great pressure at 700-800°C. However, it was not until 1932 that William Justin Kroll refined the process by reducing titanium tetrachloride with Ca, and later with Mg and Na [3]. This became known as the Kroll process, and it is currently the predominant method for the commercial production of titanium.

It is a two-step process, which starts with the production of titanium tetrachloride through a Fluidized bed chlorination process [4] described by following formula:

$$TiO_2(s) + 2Cl_2(g) + C(s) \rightarrow TiCl_4(g) + CO_2(g)$$

The resultant titanium tetrachloride is fed into vertical distillation tanks where it is heated to remove the impurities. Thereafter, the purified liquid titanium tetrachloride is transferred to a reactor vessel in which Mg is added and the container is heated to slightly above 1000°C. At this stage, the argon is pumped into the container to remove the air and prevent the contamination of the titanium with oxygen or nitrogen. During this process, the magnesium reacts with the chlorine to produce liquid magnesium chloride, thereby leaving the pure titanium solid. The process can be described as [5]:

$$TiCl_4(l) + 2Mg(l) \rightarrow Ti(s) + 2MgCl_2(l)$$

Despite ongoing research to find cheaper and more efficient methods such as the FFC Cambridge process, where titanium dioxide ($TiO_2$) can been reduced electrolytically in solution of molten $CaCl_2$[6], the Kroll process still remains the primary method for commercial production of Ti.

# 2 Crystal structure of titanium and titanium alloys

The mechanical properties of metallic materials are closely related to their crystal structure. Starting with elastic properties that are closely related to the electronic structure dependent on atomic arrangement, ending with the plastic behaviour which is in most materials determined by dislocation slip and thus the movement of individual atoms at distances greater than interatomic distances. Understanding the change in crystal structure under various conditions (thermos-mechanical treatment, the addition of alloying elements…) thus plays a key role in tuning their mechanical properties.

Pure titanium exists in two crystal arrangements depending on the temperature at ambient pressure. At room temperature, it has a hexagonal close-packed structure (hcp), which is also called the α phase. When heating pure titanium above the so-called β-transition temperature, a phase transformation to a body centered cubic structure (bcc), the so-called β phase, will occur. As schematically shown in Figure 1-3, for pure titanium this temperature is 882 °C [2], but in the case of titanium alloys it is strongly dependent on the content of alloying elements.

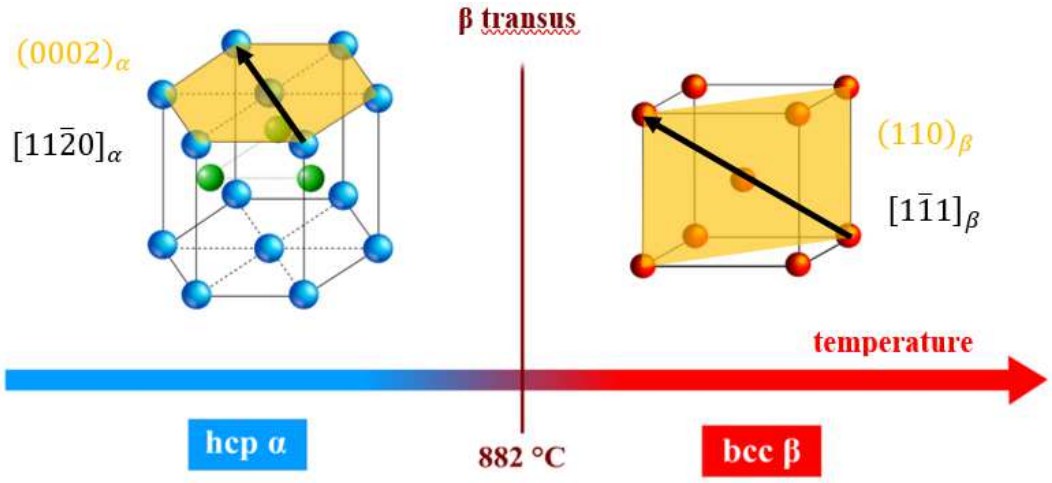


Figure 2-1 Scheme of crystal structure change from hcp to bcc phase upon heating

## 2.1 Titanium alloys - Equilibrium phases

Investigating the influence of alloying elements on the crystal structure is a difficult task. Since we can classify titanium alloys as multi-particle systems, basic thermodynamic rules (such as the second law of thermodynamics and the resulting

theorem on the minimalization of the Gibbs free energy) must apply on them. The competition between different phases is then based on the respective values of the Gibbs free energy: $G = H - TS$. Correct prediction of the crystal structure primarily depends on the correct calculation of the entropy and enthalpy of the system, which depends on pressure, composition, magnetic field, electric field, stress field etc.

One approach to qualitatively estimate the behaviour of alloying elements is based on the observation of their effect on the beta transition temperature. If alloying element increases the β-transus temperature, we classify it as an α stabilizing element. These elements are generally non-transition metals (Al) or interstitial elements (O, C or N). Elements which lower the β-transus temperature on alloying with Ti are termed β-stabilizers. These are further divided into β-isomorphous and β-eutectoid forming elements, depending on the details of the resulting binary phase diagrams. It can be seen from Fig.1-4 that β-eutectoid elements (Fe, Cr, Co…) have low solid solubility in the α phase and therefore usually form intermetallic compounds. On the other hand, β-isomorphous elements dissolve in both α and β matrix and don't form intermetallic compounds. The most important elements from this group are Mo, Nb, V and Ta. Sufficient concentrations of these elements make it possible to stabilize the β phase at room temperature.

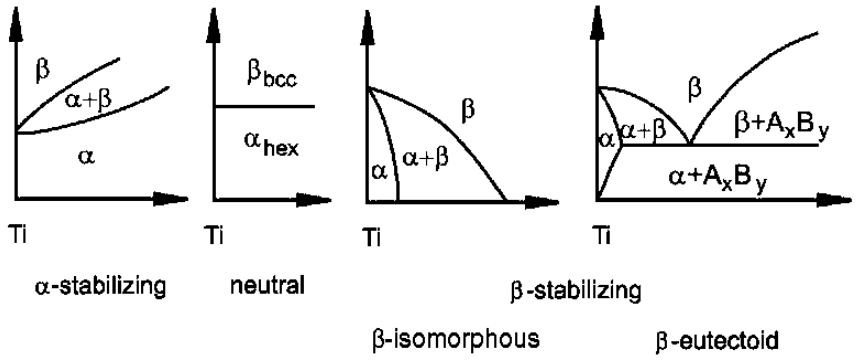


Figure 2-2 Schematic phase diagrams of titanium with different alloying elements. Taken from [2].

Unlike in pure Ti, the single-phase regions are separated by a two-phase α+β region where the mechanical mixture of both phases is present. The width of this region increases with increasing solute content [7]. If the addition of an element changes the

β-transus temperature only slightly, like in the case of Zr, we treat this element as neutral.

The transformation of the bcc β phase to the hcp α phase in titanium and titanium alloys can occur by a displacive transformation or by a diffusion-controlled nucleation and growth process depending on the cooling rate and alloy composition. The crystallographic orientation relationship between the reconstructive transformation from β → α which is also schematically represented in Fig. 1-3 follows the Burgers relationship [2]:

$$(110)_\beta \,||\, (0002)_\alpha$$
$$[1\bar{1}1]_\beta \,||\, [11\bar{2}0]_\alpha$$

According to this relationship, a bcc crystal can transform to 12 hexagonal variants, having different orientations with regard to the parent β crystal. This Burgers relationship is closely obeyed for both the martensite transformation and the conventional nucleation and growth process.

## 2.2 Stability of β-titanium alloys

One of the ways to quantitatively determine the influence of individual elements is the molybdenum equivalency parameter (MoE). This quantity is a combined measure of the effects of β-stabilizing elements, α-stabilizing elements, and neutral elements contained in a Ti alloy on the beta phase stability. The equation is given by [8]:

$$\mathrm{MoE} = 1[\mathrm{Mo}]_{\mathrm{wt.\%}} + 0.67[\mathrm{V}]_{\mathrm{wt.\%}} + 0.28[\mathrm{Nb}]_{\mathrm{wt.\%}} + 0.22[\mathrm{Ta}]_{\mathrm{wt.\%}} - 1[\mathrm{Al}]_{\mathrm{wt.\%}} + \cdots$$

The constant before each element concentration (in wt. %) in equation above is the ratio of the critical concentration of Mo/El to retain 100 vol. % of the metastable bcc β-phase after quenching to room temperature. The minus sign before aluminium reflects its α-stabilizing effect. In general, a MoE value of approximately 10.0 is required to stabilize the bcc β-phase during quenching from above the beta transus temperature.

Using this equation, one can calculate MoE parameter for more complex alloys and predict the β-phase stability. This approach works for most commercially

produced alloys presented in [9]. Furthermore, it was shown in [10] that MoE parameter correlates with β-transus temperature and generally decreases with increasing MoE value. The quantity MoE is thus a convenient metric to rank the beta phase stability of not only model binary alloys but also ternary or quaternary alloys. On the other hand, one has to be careful when dealing with alloys with higher content of interstitial atoms, such as oxygen or nitrogen. Even though they are considered to be α-stabilizing elements, they generally suppress the martensitic transformation and thus decrease the martensite start temperature, as was investigated in [11]. A typical phase diagram showing both stable and metastable phases present in titanium alloys with high content of β-stabilizing elements is shown in Fig. 2-3.

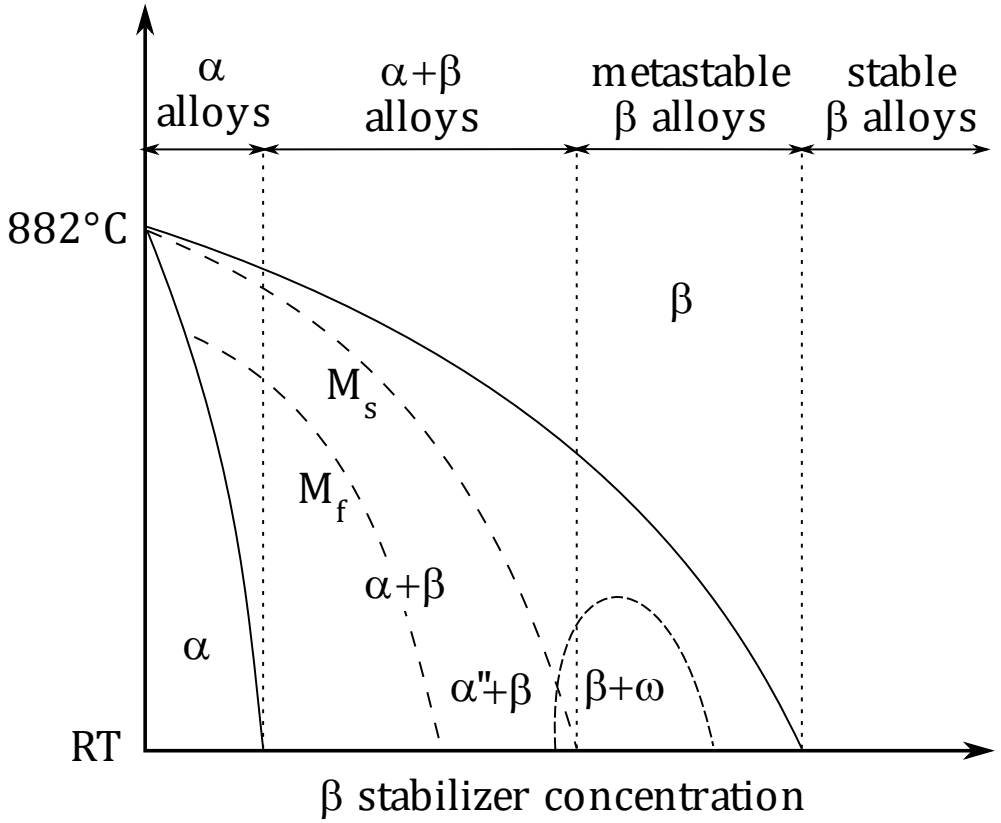


Figure 2-3 Schematical phase diagram of titanium alloys with β stabilizing elements

By splitting the phase diagram into 4 sections depending on the final microstructure of an alloy, one can distinguish between α alloys, which contain only small amount of β-stabilizing elements, α+β alloys, which usually contain both α and β phase and metastable/stable β alloys. The main difference between the last is that metastable β alloys can retain pure beta phase only after rapid quenching from β

region, but in case of the further aging process, fine α-lamellae structure will precipitate. According to the literature [12,13], such transformation can be very beneficial to increase the tensile strength but also undesirable because of the decrease of ductility. Due to the unstable nature of metastable β-alloys, several interesting effects may appear during deformation such as transformation induces plasticity (TRIP) or Twinning induced plasticity (TWIP) [14]. Non-equilibrium product phases which may occur even during quenching will be discussed in much detail in the next session.

## 2.3 Metastable phases in β-titanium alloys

Non-equilibrium or metastable phases, as distinct from equilibrium phases, are quite important in respect of many alloy systems. Equilibrium phase diagrams are usually developed by deducing the initial states of alloys which have been quenched from different temperatures to room temperature. This may seem like a reasonable approach, but one must be aware that the quenching process may lead to the formation of non-equilibrium phases. Two important examples of such non-equilibrium phases are the martensite and the athermal ω-phase. Both these phases are formed through athermal **displacive transformation** and do not rely on atomic diffusion.

As stated in [7], atomic movements in **displacive transformations** can be brought about by a homogeneous distortion, shuffling of lattice planes, static displacement waves or by a combination of these. Cooperative movements of a large number of atoms in a diffusion-less process accomplish the structural change in displacive transformations. Unlike the diffusional atomic jumps which are thermally activated, the displacive movements do not require thermal activation and cannot, therefore, be suppressed by quenching. A structural transition involving periodic displacements of atoms from their original positions can be described in terms of a displacement wave. Both the athermal martensitic and ω-transformations can, respectively, be described in terms of long wavelength and short-wavelength displacement waves. These relations will be presented in the next chapters 2.3.3 and 2.3.4

During the process of rapid cooling from the β-phase field, when a composition-dependent temperature (known as the martensite start temperature $M_S$ in

Fig. 2-3) is crossed, the bcc β-phase commences transforming spontaneously to the martensite phase whose structure may be hcp (α′) or orthorhombic (α″), depending on the alloy composition. However, another athermal process, namely that associated with the formation of the $\omega_{ath}$-phase, competes with the martensite formation. At any temperature compatible with the formation of both α′/α″ and ω-phases, there is a narrow range of composition just beyond the martensite formation regime, over which the $\omega_{ath}$-phase forms from the parent β-phase. As shown in Fig. 2-3, even $\omega_{ath}$-phase may be present at the same time as α″. If we further increase the amount of β-stabilizing element, martensitic α″ is suppressed and pure β with $\omega_{ath}$-phase can be observed.

### 2.3.1 Isothermal ω formation

The $\beta \rightarrow \omega_{ath}$ transformation is displacive, diffusion less and the $\omega_{ath}$-phase so obtained has a composition very close to that of the β-phase. Another way of ω phase formation is the isothermal aging process. The thermally activated transformation, on the other hand, is accompanied by solute rejection by diffusional processes from the ω phase to the β-phase and is thus partially replacive in nature. As stated in [15], the $\omega_{iso}$ phase can be formed in the wide temperature range of approximately 150−500 °C (the exact temperature range of ω formation varies between different systems depending on the alloying additions to the titanium alloys) and is usually denoted as $\omega_{iso}$. $\omega_{iso}$ phase precipitates in metastable β-Ti alloys during low-temperature heat treatments that favour the $\beta \rightarrow \omega_{iso}$ transformation over the $\beta \rightarrow \alpha$ transformation. $\omega_{iso}$ phase has been found to nucleate at defects in the β matrix left by $\omega_{ath} \rightarrow \beta$ phase transformation during heat treatment or at $\omega_{ath}$ phase locations in the β matrix with lower concentrations of β-stabilizers due to nanoscale chemical fluctuations.

### 2.3.2 β phase decomposition

Another effect associated with metastable β alloys with an amount of β stabilizing elements high enough to suppress the formation of $\omega_{ath}$ phase is the **decomposition of β** solid solution into a thermodynamically stable aggregates of two bcc phases, one **solute lean** and the other **solute rich**. They are usually marked with a lean/rich index according to whether they are enriched or depleted of β-stabilizing elements. It should be noted that both phases have the same crystallographic structure

as the parent β phase and their only difference is in lattice parameters, as was measured for example in [16].

Even though this effect might seem unimportant, such decomposition occurs during the ageing of the metastable β alloys and can lead to unexpected effects, such as transformation from the β → α″ induced via heating or isothermal ageing [17]. This effect can be explained by the above presented spinodal decomposition, where in the regions with low content of β-stabilizing elements the martensite start temperature $M_S$ locally increases (as can be seen in Fig. 2-3). This may result in the formation of α″ phase via either the martensitic transformation during ageing or the subsequent cooling after aging.

### 2.3.3 Crystallographic relation between β and α″/α′ phase

The martensite transformation β → α′/α″ involves the cooperative movement of atoms by a shear/shuffle type process resulting in a microscopically homogeneous transformation of the bcc β-phase into the hexagonal/orthorhombic crystal lattice over a given volume. The transformation from β → α′/α″ is composed of two necessary components, one is the $\{11\bar{2}\}\langle 111\rangle$ **shear** and the other is the $\{110\}\langle 1\bar{1}0\rangle$ **shuffle**. According to [2], both hexagonal and orthorhombic martensitic phases originate from the same shear + shuffle mechanism. The main difference between them is that **in case of orthorhombic martensite,** the $\{110\}\langle 1\bar{1}0\rangle$ **shuffle operates to lower degree,** and therefore the orthorhombic martensite (α″) has lower symmetry than both β (bcc) and α′ (hcp) phase. This feature can be seen if we look at the subgroups of parent β phase and child α′ phase. Their space groups are $Im\bar{3}m$ and $P6_3/mmc$, respectively, and according to the literature [18], the transformation pathway from space group with higher to lower symmetry (group → subgroup) can be expressed in the following manner:

$$\mathbf{Im\bar{3}m}\ (\boldsymbol{\beta}) \rightarrow I4/mmm \rightarrow Fmmm \rightarrow \mathbf{Cmcm}\ (\boldsymbol{\alpha''}) \leftarrow \mathbf{P6_3/mmc}\ (\boldsymbol{\alpha'})$$

Here we can see that both $Im\bar{3}m$ and $P6_3/mmc$ share the same subgroup, which is the orthorhombic martensite phase $\mathbf{Cmcm}\ (\boldsymbol{\alpha''})$. The $I4/mmm$ space group represents the tetragonal distortion along the cubic $\langle 100\rangle_\beta$ direction and $Fmmm$ space group the structure with different distortions along two orthogonal cubic $\langle 011\rangle_\beta$ directions. The

final structure corresponding to Cmcm spacegroup can be finally obtained by alternating shuffle of opposite $(110)_\beta$ planes. The final amplitude of this shuffling is then reflected in the parameter of the y coordinate of atomic Wyckoff position 4c: (0, y, 1/4). For the specific values of y and lattice parameters, the Cmcm space group (α″ phase) can degenerate into a structure with higher symmetry – hcp α′ phase in this case. Such a high symmetry structure with spacegroup $P6_3/mmc$ can be considered a special case of Cmcm spacegroup when the $\{110\}\langle 1\bar{1}0\rangle$ **shuffle** proceeds until y coordinate of atomic Wyckoff position reaches 1/6 and the ratio of the lattice parameters $b/a$ is equal to $\sqrt{3}$ (to have 60° angle between three neighbouring atoms in one plane and thus hexagonal symmetry).

Nevertheless, one must be careful when dealing with shuffling in different crystallographic structures. Due to symmetry reasons, the origin of the α″ unit cell is ¼ shifted along the y-axis compared to the position of atoms in $\{110\}_\beta$ planes of the parent β phase, where the atoms are usually drawn in the corners. Because of this, the α″ structure **without shuffle** (as it would be a β phase) would have **y equal to 1/4** and the corresponding α″ structure with **full shuffle** (as it would be an α′ phase) would have the **y** parameter **equal to 1/6.** This transition primarily (but not only) made of $\{110\}_\beta\langle 1\bar{1}0\rangle_\beta$ shuffle can be imaged if we draw the corresponding Cmcm unit cell into the $(110)_\beta$ and $(0001)_{\alpha'}$ planes. The transition is represented in Fig. 2-4.

Whether α′ or α″ will appear upon quenching depends mainly on the concentration of solute atoms. In the case of Ti-Nb system, the α′/α″ solute content boundary lies around 5.7 At.% [2], which means that Nb leaner alloys with lower concentration will transform to hexagonal martensite (α′ phase) and Nb richer alloys to α″. The orientation relation between β and α″ can be described as:

$$(110)_\beta \,||\, (001)_{\alpha''}$$
$$[1\bar{1}1]_\beta \,||\, [1\bar{1}0]_{\alpha''}$$

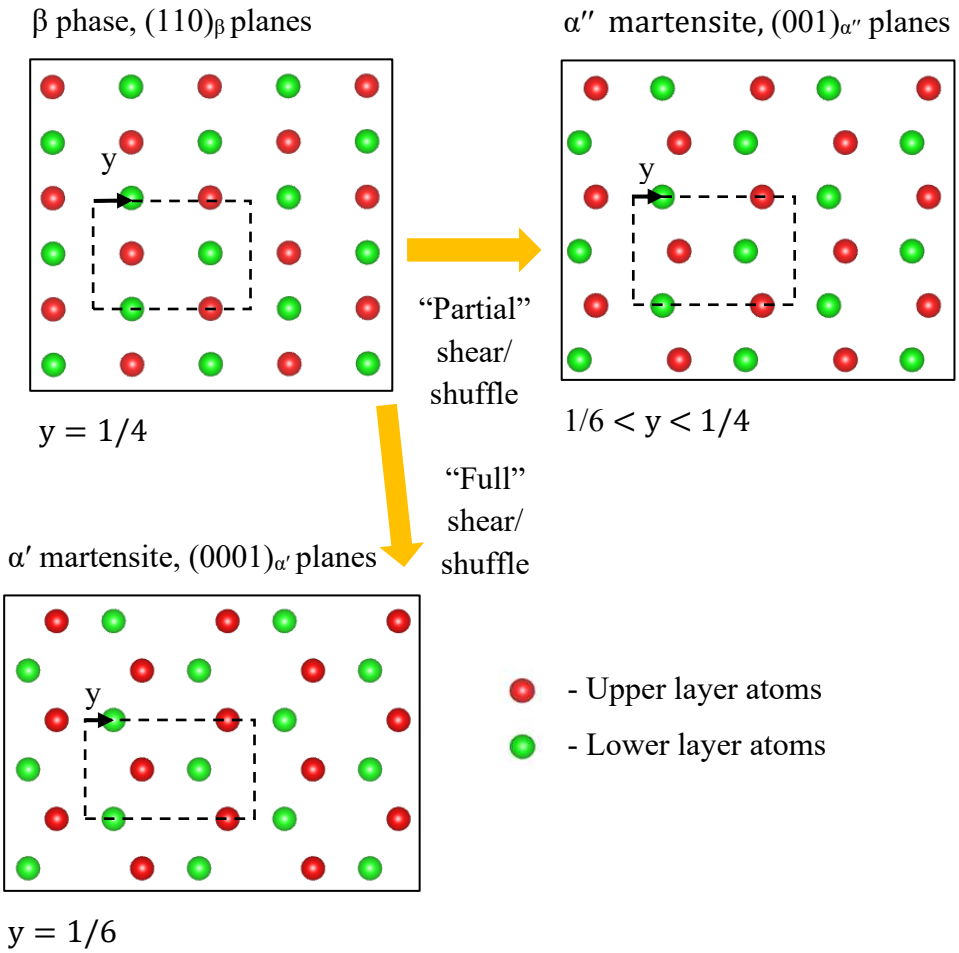


Figure 2-4 Structure correspondence between parent β phase and orthorhombic α″ or hcp α′ martensite. Drawn rectangles represent the corresponding unit cell of the Cmcm spacegroup. Reproduced from [18].

### 2.3.4 Crystallographic relation between β and ω phase

The structure of the ω-phase has been determined to be either hexagonal, belonging to the space group $P6/mmm$, or trigonal, belonging to the space group $P\bar{3}m1$, depending on the solute concentration. The equivalent positions in the unit cell of the ω structure are generally 000; 2/3 1/3 (1/2−z) and 1/3 2/3 (1/2+z). In case of ideal structure with hexagonal symmetry, z is equal to 0 and unit cell contains 2 atoms. Condition $0 < z < 1/6$ defines only partially collapsed structure with trigonal symmetry and thus contains three atoms in the unit cell. Due to its martensitic origin, the packing density (0.57) associated with the hexagonal structure of the ω-phase is lower than that for the bcc (0.68) and the hcp (0.74) structures. The crystallographic relation between β and ω phase can be described as:

$$(111)_\beta || (0001)_\omega$$

$$[011]_\beta || [11\bar{2}0]_\omega$$

One of the ways to explain the mechanism of ω formation from parent β phase is based on displacive transformation via introducing the wave vector perpendicular to $(111)_\beta$ planes: $\vec{k} = \frac{2}{3}[111]_\beta$. Such a displacive wave would cause (partial or full) collapse of B and C planes of parent β phase, as can seen from Fig. 2-5. This mechanism was firstly proposed in 1970's by De Fontaine in [19] and the theory was already confirmed by direct observation using HRTEM [20]. ω phase has attracted huge attention in previous years due to its positive effect on strength via direct $\omega_{iso}$ phase precipitation or ω controlled nano scaled α phase precipitation. Even though it generally increases the yield strength, the alloys are usually much more brittle, and their ductility rapidly decreases. The other interesting properties like the ordering of ω particles or their effect on elasticity can be found in [21,22].

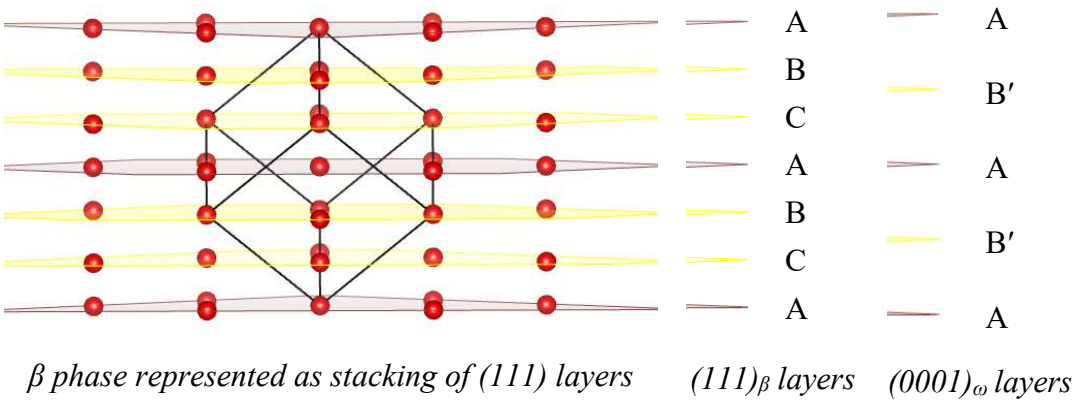


Figure 2-5 Above presented β → ω transformation can be seen as the collapse of two different $(111)_\beta$ layers (B and C). Due to the displacive nature of this transformation, the B and C layers don't have to collapse fully into 1 layer. Such a crystal structure would not have a hexagonal, but rather trigonal unit cell. Reproduced from [23].

## 2.4 Titanium alloys with increased oxygen content

Oxygen as an interstitial element together with C and N is generally considered to be an α stabilizing element. Even though there exists more kinds of interstitial sites, the most stable are octahedral ones for both α and β phase [24]. In case of the α-Ti lattice the octahedral interstitial sites are symmetrical with a size of 54.6 pm, while the octahedral interstitial sites in the β lattice are asymmetrical with the size of 20.3 pm and 83.6 pm along the <100> and <110> directions, respectively. Though the size

along the <110> direction of the octahedral interstitial sites in the β-Ti lattice is much larger than oxygen atom radius (66 pm), the oxygen dissolution in the β-Ti lattice requires more energy to push away the two Ti atoms in the <100> direction compared to that in the α-Ti lattice. Hence, the oxygen solubility in the β phase is much smaller than that in the α phase (0.8~3.8 at.% and 34 at.%, respectively)[25].

Oxygen presence also determines the deformation modes and secondary phase precipitation/formation. Its effect on mechanical properties was studied in many articles [11,26–30] (with oxygen content ranging from 0 to 3 at.%). They conclude:

- The increase of oxygen content **suppresses** the formation of $\omega_{ath}$ in near β-Ti alloys and inhibits the formation of $\omega_{ath}/\omega_{iso}$ upon further cooling/heating.
- The oxygen lowers the volume fraction of the stress induced martensite via the formation of the randomly oriented orthorhombic nanodomains upon quenching.
- The yield strength and ultimate strength increase with increasing oxygen content. The elongation initially decreases and then increases in Ti-Nb-Ta-Zr-O and Ti-Mo-O metastable β systems.
- The interaction of oxygen with dislocations in the alloy results in a pronounced yield point in the stress-strain curve. Additionally, this interaction promotes substantial deformation strengthening, leading to a high level of ductility exceeding 20%.
- High oxygen level tends to depress the activation of deformation twinning and stress-induced martensite, so the deformation mechanism is mostly based on dislocation slip.

One of the basic representatives of metastable β-Ti alloys with increased oxygen content is Ti–23Nb–2Zr–0.7Ta–1.2O (at.%), so-called gum metal alloy. It has attracteda considerable attention due to its multiple super-properties including low elastic modulus, high strength, superelasticity, excellent cold workability and invar/elinvar-like behaviour. Its nonlinear elastic behaviour has often been related to martensitic transformation, the movement of interstitial atoms, or other local structural changes; however, the precise mechanism of nonlinear elasticity in Gum Metal is still unknown [31]. The author of the study proposes that the contradicting nature of it's

mechanical properties is partly because not only one but multiple deformation mechanisms operate in Gum metals but also that the deformation mechanisms of Gum metals are strongly affected by small changes in composition, processing parameters and deformation modes.

According to [32], invar-like behaviour, i.e. a very small thermal expansion coefficient, $< 2 \times 10^{-6}\ \mathrm{K}^{-1}$, is only present after cold working: annealed specimens show a larger linear expansion coefficient, $8 \times 10^{-6}\ \mathrm{K}^{-1}$. It is well known that the small thermal expansion coefficient of Fe–Ni ferromagnetic alloys is attributed to the volume change upon magnetic transition that compensates the normal lattice vibrational contribution. However, Gum metals are paramagnetic, similarly to other Ti alloys, and thus this mechanism cannot be used to explain their low thermal expansion. They also concluded that low Young's modulus of Gum metals is due to the fact that a high oxygen concentration suppresses the formation of α″ martensite and $\omega_{ath}$ phases which both raise the Young's modulus.

Different from solution-treated samples presented above, **cold working** of Ti-Nb-Ta-Zr-O alloys with low β stability results in the formation of the ω phase which decreases the free energy of the system [29]. However, the nucleation and growth mechanism for the ω phase at low temperature has not yet been clarified in detail, because its analysis is quite difficult at low temperatures. It is considered that vacancies, areas with local strain fields and areas with compositional partitioning are possible nucleation sites for the ω phase. It is possible that the defect structures induced by cold working could promote the formation of the ω phase at low temperature. Therefore, cold working combined with oxygen addition produces a low Young's modulus compatible with high strength in Ti–Nb–Ta–Zr–O alloys, as was also presented in [11,33].

Although the exact mechanism behind the behaviour of metal gums is still not clear, its origins are most probably related to nanosized modulated domain (nanodomain) structure in the β matrix, which was firstly observed by Tahara in Ti-Nb-O based alloy [34]. They claim that the nanodomain structure is introduced by randomly distributed oxygen atoms and their local strain fields. These local fields then suppress the long-range martensitic transformation due to the presence of a nanodomain structure. It is

strongly suggested that the unique properties of Gum metals are associated with the local structure induced by the addition of oxygen. These nanodomains are often referred to as the O′ phase in the literature. More details about this phase are given in the next chapter.

### 2.4.1 O′ phase and the strain glass effect

The nano-sized modulated domains (O′ phase) were observed in several solution-treated titanium alloys, such as metastable β alloys with increased oxygen content [35], Ni-rich Ti–51.5Ni alloy [36] or even dilute binary Ti-18Mo (at.%) [20] alloy. According to the literature, the nanodomains are formed due to the **frustration created by point defects** (such as oxygen) **or dopants** (excess of Ni or Mo) in the matrix. Such frustration creates glassy nano-sized martensite-like domains that do not grow into a macroscopic martensite during cooling and instead show typical glass freezing dynamics. [34]

The more detailed mechanism of the formation of nanosized O′ phase in Ti-Nb-O and Ti-Mo alloys is described in [20,37], respectively. Even though in the former case the frustration is created by interstitial oxygen atoms and in the latter one it's because of too high Mo content exceeding a critical value, the observed crystal structure is the same in both cases and we will focus more on Ti-Nb alloys with high oxygen content.

The resulting effect of oxygen addition may sound counterintuitive at first glance. In [37], authors argue that despite the general **suppressing effect of oxygen towards β → α″** transformation upon quenching, the **oxygen as an α stabilizing element indeed stabilizes the α″ phase in the range of concentration where it can still be observed** (Ti-20Nb-(0-0.5)O at.% in this case). Important factors in understanding these observations are the interstitial oxygen atom sites and the directions of the local strain field generated by oxygen atoms in the β and α″ phases.

Oxygen atoms in the parent β phase can occupy the three types of octahedral sites and they generate local strain fields along $[100]_\beta$, $[010]_\beta$, and $[001]_\beta$ with tetragonal symmetry. The distribution of these three types of interstitial sites is assumed to be random and even in the β phase. As shown in Fig. 2-6 b, the local strain

fields along $\langle 100 \rangle_\beta$ can be relaxed by shuffling adjacent $\{110\}_\beta$ planes in the $\langle 110 \rangle_\beta$ directions (i.e., the shuffling process of the β → α″ martensitic transformation), which corresponds to the nanodomains.

In total, there are six variants of nanodomains, depending on the direction of local strain fields induced by oxygen atoms in the β phase. If the three types of interstitial sites were distributed evenly and randomly in the β phase, all six variants of the nanodomains would be induced (Fig. 2-6 (a)). These nanodomains suppress the formation of long-range α″ martensite; therefore, the β phase is stabilized by oxygen atoms and nanodomains.

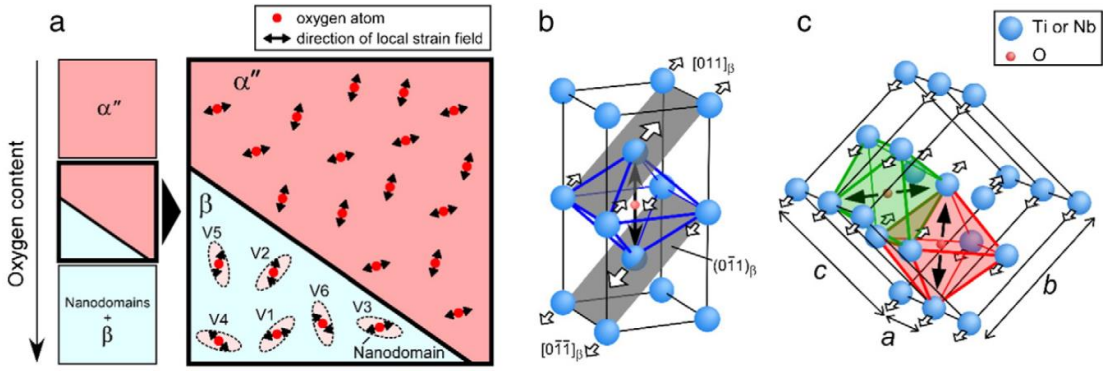


Figure 2-6 Schematic illustrations of the interstitial oxygen site and relaxation of local strain fields introduced by oxygen atoms in the (b) parent β, and (c) α″ martensite phases. Taken from [37].

On the other hand, the $\{11\bar{2}\}\langle 111 \rangle$ shearing process (b/a ratio of resulting α″ phase) in α″ martensite progresses with increasing oxygen content. As a result, oxygen atoms enhance the shuffling and shearing, transforming the α″ martensite to an hcp-like structure through the addition of oxygen. This is the mechanism presented by Tahara in [37] by which oxygen atoms stabilize α″ martensite in the α″ phase of the Ti-Nb-O alloys.

The presence of nanodomains was also reported in Ni rich TiNi alloys, which are well known for their shape memory effect. The authors considered this nanodomains to be a *"strange state in-between martensite and non-martensite"* and named it a *"strain glass"* [38].

The stain glass transition is somehow different from martensitic one. According to the third law of thermodynamics, all matter should take a long-range ordered form at low temperature so as to approach a zero-entropy state. This thermodynamic requirement is responsible for all kinds of disorder-order transitions found in nature (for example liquid–crystal transition) which are all featured by long-range ordering of certain order parameter, such as atomic configuration (for liquid–crystal transition), magnetic moment (for ferromagnetic transition), polarization (for ferroelectric transition), and lattice strain (for ferroelastic/martensitic transition).

Contrasting with the thermodynamic disorder–order transitions mentioned above, another large class of transitions called “glass transitions” exists, which is characterized by the freezing of a dynamically disordered phase into a statically disordered glass state with local order only.

A glass transition is often observed when doping sufficient point defects or inhomogeneity into a system showing normal disorder–order transition, and a glass transition appears when the long-range ordering transition is suppressed. Typical example is the formation of jelly (a structural glass) by doping enough gelatine into the water to suppress the water–ice transition. By the same reasoning, it should be possible to achieve a “strain glass transition” by doping sufficient amount of defects into a normal ferroelastic/martensitic system. Such strain glass transition should be the gradual freezing of dynamically disordered lattice strains (i.e., freezing of a “strain liquid”).

The glass is characterized by a gradual slowing-down of dynamics [3], just like the cooling of gelatine in water solution – the system becomes more and more “sticky” and eventually the dynamics is so slow that the system is virtually frozen in a disordered state without a change in average structure. The detection of a glass transition is basically a detection of its drastic slowing-down of dynamics or increase in “stickiness” with cooling without changing average structure. One of the ways how to detect such a transition is by a frequency-dependent AC modulus/loss measurement, which reveals the anomaly at $T_g$ following Vogel–Fulcher relation. Another approach was used in [39], where they studied structural evolution and mechanism of strain glass transition in TiNi alloys by anomalous small-angle X-ray scattering.

There is still much more to say about crystallography and changes which occur at different temperatures, chemical compositions, or stress conditions. The most important findings for this work were summarized in this chapter. Next, we will look at experimental techniques used in this thesis, sample preparation, the results of our work and final experimental findings.

# 3 Sample preparation

## 3.1 Arc melting and oxygen content analysis

All sample were prepared from the mixture of (pure) elements necessary to obtain desired chemical composition. In the case of oxygen-free samples, we used pure elements (Ti and Nb) in required amount. 7g buttons were remelted 6 times by arc melting in the argon atmosphere to avoid chemical inhomogeneities. Samples were then solution treated for 12h at 1200°C and then water quenched from temperature 1000 °C. A little layer of oxide on the surface of each sample was then mechanically removed by grinding on SiC papers.

In the case of samples with oxygen, all alloys have been prepared by the same way but not from the pure elements but rather master alloy Ti-45Nb, Pure Ti and $TiO_2$ powder. Samples were solution treated for 12h at 1300°C and then water quenched from temperature 1100 °C. A little layer of oxide on the surface was removed as in the oxygen free samples.

Due to the reactive behaviour of titanium and niobium with oxygen at high temperatures during arc melting and solution treatment, it is always worth to verify the oxygen content after the final heat treatment and check whether the sample didn't gain any additional O/N atoms. The oxygen and nitrogen were determined using the G8 GALILEO elementary analyser. This analyser works on the principle of sample fusion in a stream of inert gas - IGF (Inert Gas Fusion). An accurately weighed sample is introduced into a hot graphite crucible with temperature about 3000°C where it promptly melts in an inert gas (Ar in our case). The released gases are then properly analysed. Oxygen reacts with graphite, forming carbon monoxide (CO), whereas nitrogen and hydrogen are released in elemental form as $N_2$ and $H_2$, respectively. The resulting gases are conveyed to the detection system where their quantities are

determined precisely with the aid of TCD and NDIR detectors. With knowledge of the weight of the sample, the absolute content of O, N, and H in the sample is precisely determined. The results of oxygen and nitrogen measurement are presented in table 2.

Table 2. Results from the measurement of oxygen and nitrogen content in all samples. Data are presented as an average value with standard deviations.

| Sample | O [At. %] | $\sigma_O$ [At. %] | N [At. %] | $\sigma_N$ [At. %] |
|---|---|---|---|---|
| Ti8Nb | 0.21 | 0.04 | 0.06 | 0.05 |
| Ti12Nb | 0.18 | 0.01 | 0.08 | 0.10 |
| Ti12Nb1O | 0.91 | 0.05 | 0.05 | 0.02 |
| Ti12Nb2O | 1.65 | 0.11 | 0.05 | 0.01 |
| Ti12Nb3O | 2.75 | 0.01 | 0.06 | 0.01 |
| Ti16Nb | 0.18 | 0.03 | 0.02 | 0.01 |
| Ti16Nb1O | 0.89 | 0.03 | 0.08 | 0.06 |
| Ti16Nb2O | 1.81 | 0.16 | 0.03 | 0.03 |
| Ti16Nb3O | 2.64 | 0.03 | 0.04 | 0.01 |
| Ti20Nb | 0.21 | 0.05 | 0.02 | 0.01 |
| Ti20Nb2O | 1.83 | 0.48 | 0.04 | 0.01 |
| Ti20Nb3O | 2.71 | 0.09 | 0.06 | 0.04 |
| Ti24Nb | 0.23 | 0.11 | 0.03 | 0.02 |
| Ti28Nb | 0.22 | 0.11 | 0.04 | 0.02 |

As we can see from the table 2, Samples with zero nominal value of oxygen have around 0.2 at. %. This value is much lower than in case of commercially produced titanium alloys and comes from the impurities within pure elements. In the case of samples with additional oxygen, we can see that all the samples have a little less oxygen than we would expect from the nominal values established during sample preparation from pure elements/elemental powders. These errors may be related to the systematic errors made during sample preparation due evaporation of oxygen from melted $TiO_2$powder into the Argon atmosphere. This would also explain the reason why the measured oxygen content is systematically lower and not higher than we would expect. This way or another, the differences in nominal and measured values are about 0.3 at.%, what we can still consider as a good result when dealing with titanium alloys. As for the nitrogen content, its levels are about 0.4 at.% in all the prepared samples. We can thus say that no significant contamination occurred during sample preparation.

## 3.2 Samples for SEM/LM and XRD

The preparation of samples for SEM and LM was carried out in the same way. Thin slices were cut from individual solution treated samples using the Struers Accutom-50 and ATM Brillant 220 automatic saw with a diamond blade. After mounting them on an aluminum holder and securing them in a fixture, grinding and polishing were performed using the Struers Tegramin-25 instrument. By gradually increasing the grit size of SiC-based grinding papers from 220 to 4000, a smooth surface without relief was achieved, always verified by an optical microscope. The final polishing was performed using the same instrument on a metallographic polishing cloth with OP-S suspension containing approximately 20% $H_2O_2$ for 15 minutes. The prepared samples were suitable for experimental measurements.

In case of XRD measurement, all samples were thinned to the level of 0.1-0.2 mm. Prepared samples are presented in Figure 3-1.


Figure 3-1 Prepared thin samples with various compositions.

# 4 Experimental methods

## 4.1 Scanning electron microscopy – SEM

The resolution of optical microscopes is limited by the wavelength of the light source used. For detailed study of microstructure, it is therefore necessary to use a scanning electron microscope (usually abbreviated as SEM). Compared to light, the de Broglie wavelength of electrons after acceleration is much smaller, which limits the

resolution of the electron microscope not by wavelength, but by the ability to collimate and focus the electron beam to the desired location.

The basic principle of SEM is based on the emission of electrons from the electron gun. After their acceleration by high voltage, the electron beam is gradually collimated by a series of electromagnetic lenses, and it finally impacts the surface of the sample. The interaction of electrons with the material generates various types of characteristic signals, such as Auger electrons, secondary electrons (SE), and backscattered electrons (BSE), which differ in energy and point of origin [40]. X-ray radiation can also provide information about the chemical composition. Analysis of these signals allows us to obtain information about the surface morphology, chemical composition, and microstructure.

In addition to the use of electrons instead of light, SEM also differs in the way the image is formed. In contrast to an optical microscope where the entire sample is illuminated, in SEM, each small point on the sample is investigated separately. As a result, the image is formed by sequentially scanning the electron beam across the entire surface being studied. During the measurements, we used a FEI Quanta microscope equipped with Field emission gun and EBSD detector.

### 4.1.1 Secondary electrons – SE

Secondary electrons, generated through the inelastic scattering of incident electrons, are emitted from depths of approximately 5-50 nm. These electrons carry significantly lower kinetic energy of around 50 eV compared to backscattered electrons (BSE). The primary advantage of secondary electrons is their ability to image the topography of an object, which allows us to identify the relief features even in two-dimensional images. As a result, they are commonly used in the study of surface morphology.

### 4.1.2 Back scattered electrons – SE

The most important type of signal for our discipline are the backscattered electrons (BSE). They are generated at greater depths than secondary electrons (SE) (~ 100 nm), and their kinetic energy is slightly lower compared to the incident electrons. Their origin is associated with the change in trajectory of the incident

electrons due to the attractive forces of atomic nuclei. The number of BSE detected by the detector depends on the atomic number of the element, which is also called Z-contrast. Lighter elements appear darker due to this contrast, while heavier elements appear brighter. Such contrast can help us identify the phase composition, where the β phase may appear brighter due to the presence of heavy β-stabilizing elements.

Another phenomenon, particularly relevant in the study of polycrystalline materials, is the so-called orientation contrast. It arises from the fact that the scattering of incident electrons depends on the orientation of the crystal lattice with respect to the incident beam. As a result, some grains appear brighter than others, allowing us to distinguish and study their size and shape.

### 4.1.3 Electron backscatter diffraction - EBSD

Electron backscatter diffraction (EBSD) is a powerful technique used in scanning electron microscopy (SEM) to investigate the crystallographic structure of materials. It involves using an EBSD detector, which is positioned next to the sample chamber inside the SEM stand. The sample is tilted and bombarded with a scanning electron beam, and as the backscattered electrons leave the sample, they interact with the periodic atomic lattice planes of the crystal. This interaction causes the electrons to diffract at different angles according to Bragg's law, resulting in distinctive patterns known as Kikuchi patterns, which are captured by the EBSD detector. This technique provides valuable information about the crystal orientation, grain boundaries, and microstructure of materials.

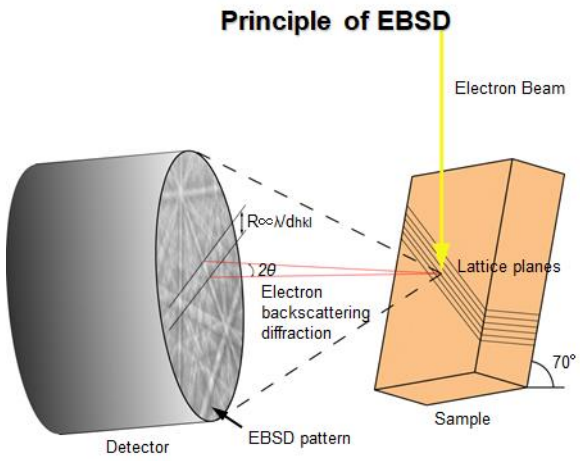


Figure 4-1 Principle of EBSD measurement. Taken from [40].

Via recoding Kikuchi patterns separately from each spot at the sample, one can reconstruct the orientational map at every grain. The data obtained by an EBSD scan are shown in the so-called inverse pole figure (IPF) map. This map shows different atomic planes perpendicular with the surface with different color. The important thing to mention is that two separate regions with the same colour can still have different orientations due to the rotational symmetry of every plane around its normal axes.

The crystal orientation can be then calculated via line indexation (Hough algorithm is usually used for easier line detection) and further voting for the most probable option. Along with three Euler orientation angles, Confidence index (CI) as a metric reflecting reliability of a given orientation is obtained for every measured point. In case where two or more non-equivalent orientations share similar Kikuchi pattern, the confidence index may be lower. Other things that reduce the quality of recorded patterns are: possible scratches on the surface of the sample, debris, low diffraction intensity, overlapping patterns due to large spot-size or big penetration volume which extends into a different grain. Another measure of indexing success is image quality (IQ), that is a measure of detected Kikuchi pattern quality. If the sample is diffracting well and IQ/CI indexes are high, several physical effect can be studied, such as recrystallization, twinning, martensitic transformations or orientation relations between separate grains. The duration of a single measurement depends on the size of the EBSD scan and the step size used, ranging from 0.5 hour up to a day.

## 4.2 Transmission electron microscopy (TEM)

TEMs create images by utilizing a high voltage electron beam. The electron gun located at the top of the TEM emits electrons that travel through a vacuum tube. Unlike light microscopes, which use glass lenses to focus light, TEMs use an electromagnetic lens to focus the electrons into a narrow beam. This beam then passes through an ultra-thin specimen, causing the electrons to scatter or hit a fluorescent screen located at the bottom of the microscope. The resulting image of the specimen appears on the screen, with various parts shown in different shades depending on their density. This image can be directly studied within the TEM or captured through photography.

Another mode very important for material science is the electron diffraction mode. Electron diffraction in a transmission electron microscope exploits controlled electron beams using electron optics. Different types of diffraction experiments provide information such as lattice constants and symmetries.

While the electron beam passes through a thin film of the material, it interacts with the sample. Part of the beam is diffracted, and part is transmitted without changing its direction. Each set of initially parallel rays (a plane wave) is focused by the first lens (objective) to a point in the back focal plane of this lens, forming a spot; a map of these directions, often an array of spots, which are called the diffraction pattern. Alternatively, the lenses can also form a magnified image of the sample. In the second case, it is a classic observation similar to light microscopy.

## 4.3 Transmission X-ray diffraction

In order to determine the crystalline structure of the material, we need to measure the integral intensity of individual reciprocal points and assign them the appropriate planes from which the given diffraction arose. This task would be very complicated to accomplish by using simple 1D detector, which usually scans only along the one direction. To overcome this issue, we decided to use Rigaku - R-axis RAPID II single crystal diffractometer; equipped with 2D detector, molybdenum anode and graphite monochromator. The arrangement od used diffractometer is presented in figure 4-2.

The arrangement of the experiment which we used for the measurement of X-ray diffraction is schematically depicted in the figure 4-2. All the important angles which we used in our analysis and which determine the positions of individual spots can be described in the following way:

- $2\theta$ angle represents the diffraction angle between primary beam and diffracted beam. Ranges from 0° to 180°.
- $\beta$ angle represents the angle between horizontal plane and a plane of incidence of monochromatized X-ray beam. This angle ranges from -90° to 270° with clockwise direction (like 6 a.m. – 6 p.m. range on the clocks). 0° angle represents diffraction in the horizonal plane when diffracted beam falls to the left side from the primary beam, as depicted in figure 4-2.

- $\varphi$ angle represents the angle of rotation of our sample, always parallel to the vertical axis. In our measurements, it ranges from -30° to 30°, 0° stands for the sample surface being perpendicular to the primary beam.

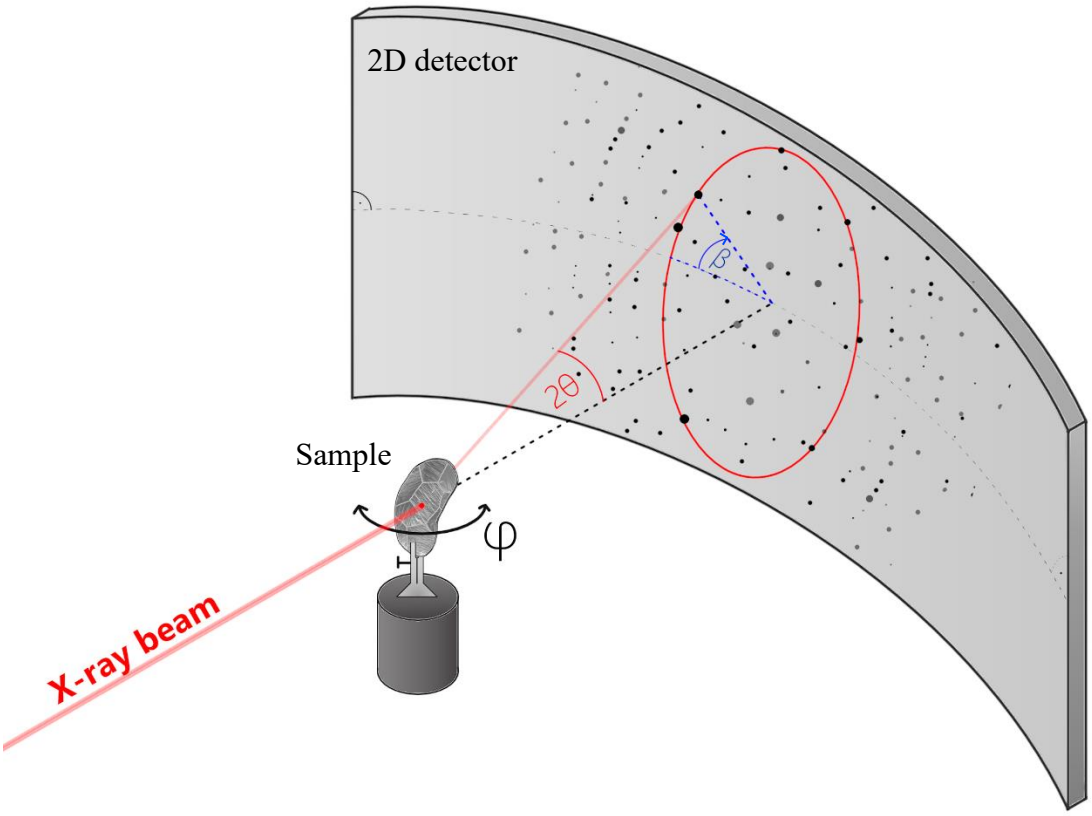


Figure 4-2 Schematic representation of experimental arrangement of measuring X ray diffraction, similar to rotation method with normal beam setting used in case of single crystals.

### 4.3.1 X-ray diffraction on fully transformed single β grain

The conventional method for determining crystal structure consists of growing a single crystal with a selected chemical composition and calculation of the structure factors out of the integrated intensities. From the calculated structure factors, we can find out what are the atomic positions and further refine the structure. In our case, we can not grow a single crystal of martensite due to its metastable nature. In reality, it is almost impossible to force the parent β phase to transform into only one variant of martensite, even though it is possible to partially suppress the formation of some variants by applying the pressure in specific direction. We thus decided to perform similar experiment to classical single crystal X-ray diffraction, but instead of

using crystal of α″ phase, we used parent single β grain which transformed into 12 variants of martensite during quenching.

The main idea of our measurement was to carefully choose one fully transformed β grain where all α″ martensite laths would be geometrically oriented with respect to the parent β grain. Because α″ variants are also oriented towards each other, we don't really need the parent β phase to be present in our sample and it should be possible to distinguish each variant by pure simulation of diffraction pattern with various parent β phase orientations.

To obtain the structure factors and subsequently calculate the atomic positions, the first necessary step was to index the reciprocal map using the geometric relations geometrical relations between all variants of α″ and parent β phase. Since only one parent β grain was observed, certain variants may have been suppressed. Such a difference in volume fraction of individual α″ variants would manifest itself in a drop in intensity. Therefore, it was crucial to distinguish individual variants and calculate structure factors for each variant separately. This requires simulation of numerous diffraction patterns with all possible orientations of parent β grain (excluding symmetrical situations) and selecting the one that best fit the reciprocal map. Our simulation followed these steps:

1. Firstly, we were looking for the peaks along horizontal and vertical direction with minimum value of intensity and prominence.
2. Secondly, all peaks were compared between each other and if any of them were too close, we preserved the one with higher intensity.

These peaks were compared to simulated reciprocal maps, each of which was simulated with a different initial orientation of the parent β phase. To avoid non-linear scaling of rotation when using spherical coordinates, we used the Icosahedron Mesh function in MATLAB to orient the structure with approximately homogeneous step size.

3. We calculated the coordinates of all reciprocal vectors of the α″ phase based on the lattice parameters obtained from integrated 1D profiles over a constant 2θ angle. Using crystallographic orientation relations between the β and α″

phases, we predicted and simulated the diffraction pattern for all 12 variants with precise 2θ and β angle determination for every reciprocal point.

4. After simulating the diffraction pattern, we calculated the number of matching diffraction pairs between the simulated and measured reciprocal maps. The higher the number of matching diffraction pairs, the closer we were to the initial structure. This allowed us to obtain a good scoring parameter for each initial orientation - the number of overlapping points - which helped us to choose the best initial orientation and predict the most probable orientation.
5. Finally, we checked the predicted pattern against the true pattern by overlaying. If the predicted orientation seemed suitable, we used it for further analysis to determine the atomic positions.

### 4.3.2 Determination of crystal structure

For determination of atomic positions, we used classical kinematic theory of diffraction, where we tried to model the structure factor using the integrated intensities and standard equation for structure factor in form

$$F_{hkl} = \sum_{n=1}^{N} f_n e^{2\pi i(hx_n + ky_n + lz_n)},$$

where $f_n$ is the atomic scattering factor for every individual atom, $hkl$ numbers characterize atomic plane and $[x_n, y_n, z_n]$ are the partial coordinate of all the atoms within the cell. In general, $F_{hkl}$ is a complex quantity: only its magnitude $|F_{hkl}|$ is related to the observed intensity. The determination of its phase, which can have any value between 0° and 360° relative to a wave scattered at the origin of the unit cell, constitutes the familiar 'phase problem'.

We assumed the measured intensities in the following form:

$$I_{measured} = I_0 . A . |F_{hkl}|^2 . Lp$$

Where $A$ stands for the absorption factor, $Lp$ is the combined Lorentz-polarization factor and $I_0$ is the scaling number which reflects the intensity. To evaluate the absorption coefficient, we used the standard equation valid for thin parallel samples [41]:

$$A = \frac{1}{\mu}\frac{1}{1-\frac{\gamma_0}{\gamma_g}}\left[e^{\left(\frac{-\mu t}{\gamma_g}\right)} - e^{\left(\frac{-\mu t}{\gamma_0}\right)}\right].$$

Where $\mu$ is the absorption coefficient [1/cm] and $\gamma_g/\gamma_0$ parameters are defined as $\gamma_g = \boldsymbol{n}.\boldsymbol{s_0}$, $\gamma_0 = \boldsymbol{n}.\boldsymbol{s}$, where $\boldsymbol{n}$ is a unit vector perpendicular to the surface of the sample pointing into the sample; $\boldsymbol{s}$ and $\boldsymbol{s_0}$ are unit vectors of incident and scattered beam.

In general, the Lorentz factor is responsible for the change of intensity caused by the time during which the corresponding lattice point is passing through the surface of the Ewald sphere. In the case of normal beam setting, the Lorentz factor has the form [42]:

$$L^{-1} = \sin(\tau)\cos(\nu).$$

Where $\tau$ and $\nu$ can be calculated from the position of the reciprocal point on the detector as $\tau = \tan^{-1}\left(\frac{\Delta y}{R}\right)$, $\nu = \tan^{-1}\left(\frac{\Delta x}{R}\right)$, where $\Delta y$, $\Delta x$ and $R = 127.26$ mm are distances from the position of primary beam on the detector and investigating reciprocal point and R stands for the radius of curvature of the detector. By knowing the size of a pixel on the detector (100 μm), we can calculate the the Lorentz factor separately for every reciprocal point.

The polarization factor $p$ arises because of the dependance of the scattered amplitude on the orientation of the electric field of the X-ray beam. The magnitude of $p$ depends on the degree of polarization of the X-ray beam. Characteristic radiation from the target in unpolarized, whereas radiation is partially polarized by reflection at a crystal monochromator. The expression for the polarization factor in the general inclination method using monochromatized radiation has the form:

$$p = \frac{(\cos^2 2\theta_M \cos^2\beta + \sin^2\beta)\cos^2 2\theta + \cos^2 2\theta_M \sin^2\beta + \cos^2\beta}{1 + \cos^2 2\theta_M}.$$

Here $\theta_M$ is the Bragg angle of the monochromator, $\theta$ that of the sample, and $\beta$ is the angle between the planes of incidence at the monochromator and at the sample. In our case, the plane of incidence at the monochromator is always horizontal and

plane of incidence at the sample can be easily read from the position of peak at the measured reciprocal map.

The final factor which we considered is the effect of thermal motion, the correction factor $T_j$ which is different for every atom. For isotropic thermal motion, $T_j$ can be writen as:

$$T_j = \exp\left(-\frac{B_j \, sin^2\,\theta}{\lambda^2}\right);$$

where $B_j$ is the 'isotropic temperature factor', od Debye – Waller factor. $B_j$ is a constant for each atom at a given temperature; it is related to the mean-square displacement of the atom in any direction from its mean position. It is usually treated as an empirical constant to be derived from a least/squares comparison of the observed and calculated intensities.

to evaluate the accuracy of our measurement, we use the standard R-factor defined as:

$$R = \frac{\sum_{hkl}\left|\left|F_{hkl}^{obs}\right| - \left|F_{hkl}^{cal}\right|\right|}{\sum_{hkl}\left|F_{hkl}^{obs}\right|} \, .$$

To avoid huge errors between measured and predicted values, we decided to exclude every value which was 3 times bigger than the calculated value. During calculation of $\left|F_{hkl}^{obs}\right|$, we basically took integrated intensities and divided the value by all the factors in the following way:

$$\left|F_{hkl}^{obs}\right| = \sqrt{\frac{I_{measured}}{I_0 . A . Lp}} .$$

These numbers were then compared with simulated values of calculated structure factors calculated as:

$$\left|F_{hkl}^{obs}\right| = \sum_{n=1}^{N} f_n e^{2\pi i(hx_n + ky_n + lz_n)} . T_n \, .$$

In order to calculate the elastic electron scattering factors separately for every atom and every scattering angle, we used standard gaussian approximation with 9 parameters taken from the book *International Tables for Crystallography* [43].

# 5 Aims of the thesis

The aims of the present thesis can summarize into several points:

- To prepare the alloys with various chemical compositions based on Ti, Nb and O elements by arc melting and measure their oxygen content.
- To study the microstructure via SEM and EBSD as well as TEM for specific samples.
- To analyse the martensite phase via X-ray diffraction method qualitatively and also quantitatively investigate the effect of oxygen.
- To discuss the of acquired results.

# 6 Results and discussion

## 6.1 Preliminary results on Ti-(8-28)Nb

As a proof of concept, we firstly produced “oxygen free” samples with Nb content ranging from 8-28 at.%. According to the literature, the critical concentration for supressing the β → α″ transformation should be around 22.5 at.%. To verify this, we checked all these samples (Ti8Nb, Ti12Nb, Ti16Nb, Ti20Nb, Ti24Nb and Ti28Nb) via XRD and SEM. Results are separately presented in the following chapters.

### 6.1.1 SEM

In Fig 6-1, we can see differently oriented lamellae of martensite in all Ti-(8-20)Nb samples. It’s hard to compare their morphology or say any further information just from the images, due to it is only a two-dimensional cut of randomly oriented variants.

Another thing which can be noticed in Ti-16Nb sample are “star shaped” features represented by dashed yellow lines. Even though it might look interesting, they are most probably just different variants of martensite laths oriented in such a way that 2 of them are separated by a mirror plane which is perpendicular to the samples surface. On the other hand, one should keep in mind that there is a strict relation between the β and martensite phase, which governs the mutual orientation between all variants of martensite. Due to this, we can distinguish them by channelling contrast created by BSE.

From the bottom two pictures, it is evident that the only present phase in case of Ti-24/28Nb alloys is β phase and no martensite was observed. This agrees with the literature, where is stated that exceeding the 22.5 at.% of Nb should stabilize β phase enough to suppress β → α″ transformation during quenching. Another thing to notice are the grains themselves, which due to the long solution treatment grew into the size of hundreds of micrometres, ass can be seen the bottom pictures at Figure 6-1.

Full black circular objects on the micrographs are nothing else than debris or dried colloidal silica, as we checked with SE detector.

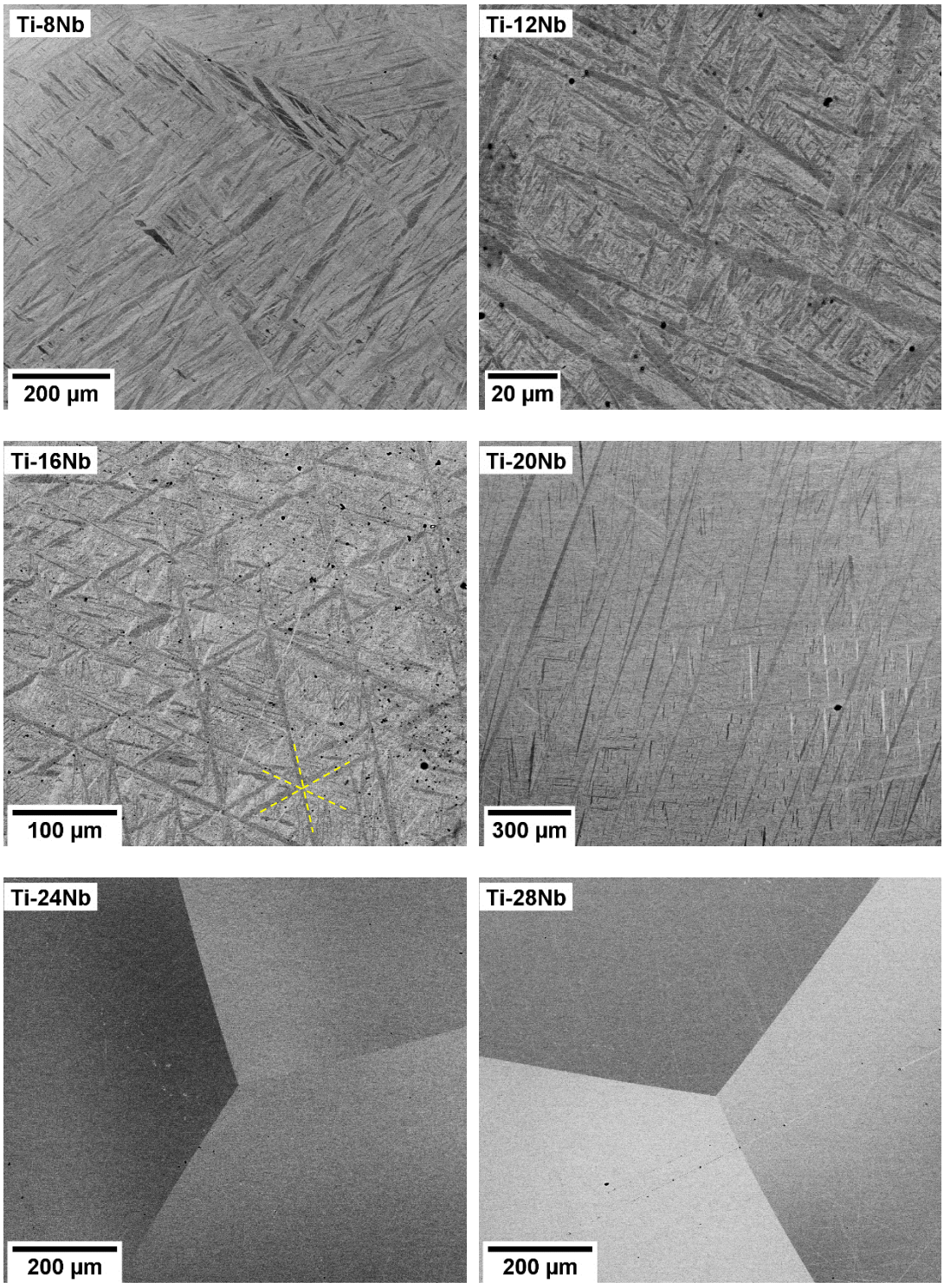

Figure 6-1 Micrographs of all oxygen-free samples taken via SEM. Different intensities is produced by channelling contrast between grains of β or α″ phase.

The very rough estimate of the width of the widest martensite laths from the picture was measured to be around 30 µm, 20 µm, 15 µm and 15 µm in Ti8Nb, Ti12Nb, Ti16Nb and Ti20Nb alloy, respectively. Due to that bigger individual laths are more prone to twinning, as will be shown in the EBSD chapter, we can qualitatively

say that the samples which are more β stabilized are less prone to twinning due to more homogeneous distribution of α″ laths with smaller width. It can be also the case that it is all affected by $M_S$ temperature. Lower the concentration of β stabilizing elements is, higher the $M_S$ temperature becomes and thus α″ lamellae start to grow at higher temperatures. Because alloys with higher niobium content have lower $M_S$ temperature, α″ martensite laths will not grow to such large dimensions and thus the critical stress necessary for the induction of deformation by twinning will not be overcome. However, to confirm this hypothesis, further experiments should be done under compression/tension, what is out of scope of this thesis.

### 6.1.2 XRD

Since we wanted to study the structure of observed α″ phase, we firstly needed to identify all present phases in our samples. In order to observe the present phases, we integrated the intensity from 2D detector over constant $2\theta$ angle and plotted the intensity vs. $2\theta$ angle in logarithmic scale, as presented in the figure 6-2. Additional graph at the bottom is showing the peaks positions with logarithmically scaled intensities predicted for powder diffration for every phase which we may expect to be present in the samples, but each with a specific lattice constant. Because the lattice parameters of α″ martensite depend on Nb content in the sample, the predicted lines cannot perfectly fit to all the structures of martensite in all the samples.

As we can see from fig. 6-2, both ω phase and α″ are present in Ti-(8-16)Nb alloys. The fact that we can't observe all ω peaks is most probably due to low ω fraction and low intensity produced by these diffractions compared to diffraction at 25°, as can be seen from the bottom graph. Another problem which usually arises when having more phases in one sample is overlap of several peaks. In this case, we can only decide the presence of the phase only if a non-overlapping peak is measured. In this case, peak at 25° is a clear sign that ω phase is present in our sample. The 2D diffraction pattern around $2\theta = 25°$ can be seen in fig. 6-5. According to the schematic diagram presented in Figure 2-3, the ω phase should be present even at little higher concentrations after the suppression of α″ martensite. This was not observed in our case, as Ti-24Nb sample doesn't show any clear, non-overlapping ω peak in the range $2\theta \in (12.5°,\ 37.5°)$. It can be that Ti-24Nb sample is stabilized enough to suppress

both ω and α″, but if this is true and Ti-16Nb contains ω phase, the Ti-20Nb sample should contain ω phase as well. To confirm this contradicting result, we directly checked the diffraction pattern from 2D detector around $2\theta$ angle. Results are compared with Ti-8Nb alloy in figure 6-5. As we can clearly see, only weak streaks from α″ peaks were observed in case of Ti-20Nb sample, compare to Ti-8Nb where ellipsoidal diffraction spots are present (shape is deformed because of different scaling of axes). Even though we can not directly see the diffraction spots of ω phase, to disapprove the existence of ω phase in the sample would need further verification via TEM, as it is the only reliable method for its much higher sensitivity to such a small structures. Diffraction patters from Ti-24/28Nb alloys show that only β phase was present, which agrees with results obtained via SEM.

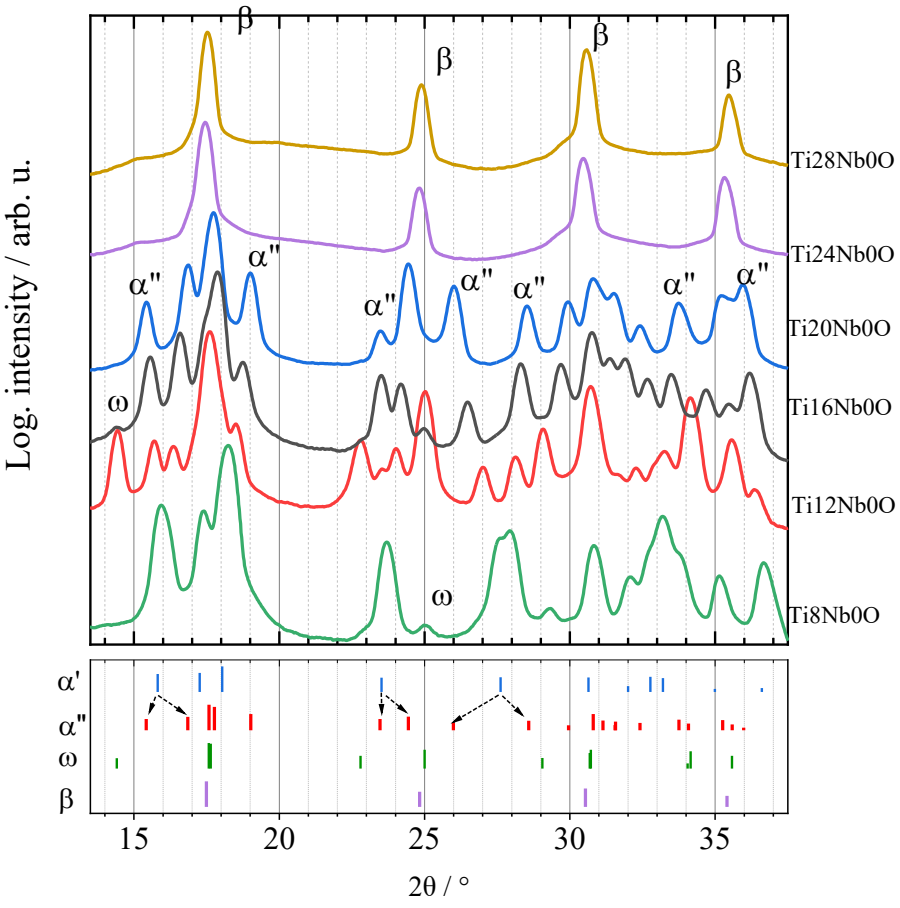


Figure 6-2. XRD integrated profile over constant $2\theta$ angle of Ti-xNb alloys. Legend at the middle right describes which curve belongs to which sample. Black arrows represent the split of several peaks due to lower symmetry of an orthorhombic structure (α″) over hcp (α′).

In order to determine how does the Nb affect the crystal structure of orthorhombic martensite, we measured the structure parameters via X'Pert Highscore plus software which considered integrated profiles as a powder diffraction and used Rietveld refinement to evaluate the basic structure parameters, such as lattice parameters. Due to that lattice parameters depend only on peak positions and not intensities, we can rely on software's results. The final plot at fig. 6-4 shows the dependence of lattice parameters on Nb content. We can see that parameter *a* is increasing, whereas both *c* and *b* a decreasing. This behaviour was explained in [44], where authors say that the difference in size of both Ti and Nb atoms is unlikely to account for the distortion leading to orthorhombic symmetry rather than hcp, since the atomic radii of both atoms are nearly the same. It has been suggested that the distortion responsible for the formation of orthorhombic structure reflects the tendency for Nb to retain the eightfold coordination obtained in β titanium. More niobium the alloy contains, more strain it requires to form fully sheard/shuffled hcp martensite. The final structure has thus orthorhombic symmetry, which require lower principal strains compared to α′.

The increase of *a* and decrease of *b* lattice parameters can be geometrically explained by $\{11\bar{2}\}\langle 111\rangle$ shear, as was proposed in the chapter about crystallography of martensitic phase. This shear can be visualized if we look at it from some of the $\{110\}_{\beta}$ planes. Figure 6-3 schematically shows the partial shear and shuffle, and above mentioned $(11\bar{2})_{\beta}$ plane.

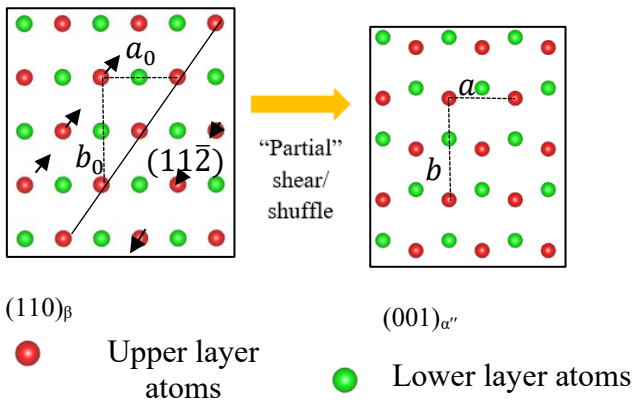


Figure 6-3 Transformation from β to α″ phase viewed from $(110)_{\beta}$ plane composed of shear (black arrows) and shuffle.

We know that lower the $b'/a'$ is, closer to hexagonal phase we are. We can see that the axial ratio $b'/a'$ decreases with increasing Nb content from 1.71 at 8 at.% of Nb to 1.53 at 20 at.% of Nb. Because hexagonal martensite has a $b'/a'$ ratio equal to cca $\sqrt{3}$ ≈1.73 and bcc β phase $\sqrt{2}$ ≈1.41, the $\{11\bar{2}\}\langle 111\rangle$ shear is more and more suppressed with increasing Nb content.

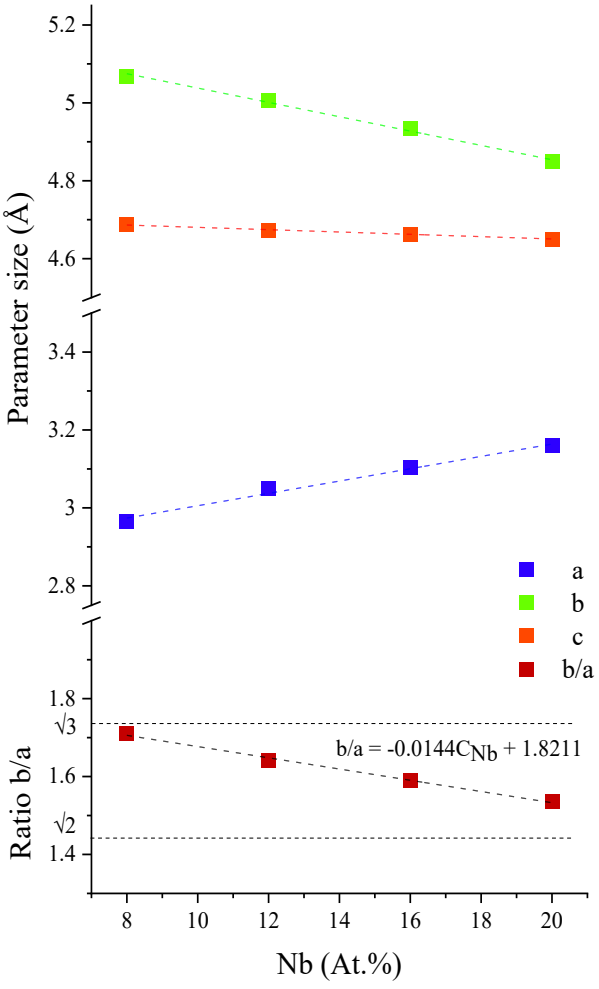


Figure 6-4. Change in the lattice parameters of martensite due to increasing content of Nb. Ratio $b'/a'$ is meant to be without units. Coloured lines represent linear fit.

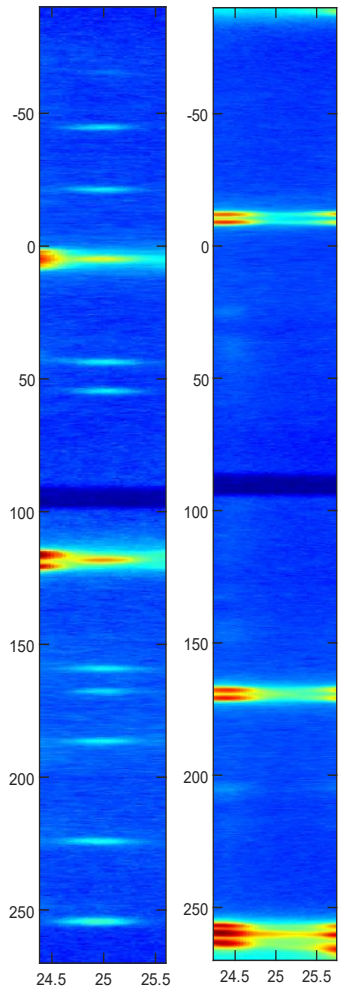


Figure 6-5. Comparison of diffraction at $2\theta = 25°$ from Ti-8Nb (left) and Ti-20Nb (right). Axes correspond to $2\theta/\beta$ angles.

Fitting the measured points by linear function gives the slope of the curve to be approximately -0.0144 per 1 at.% of Nb. If we consider this linear equation to follow from the α′/α″ (around 5.7 at.% of Nb) concentration boundary, we can roughly estimate that we should get bcc phase after addition of another $\frac{(\sqrt{3}-\sqrt{2})}{0.0144} \approx 22$ at.% of

Nb, so $5.7 + 22 \approx 27.7$ at.% of Niobium in total (or we can also simply follow the linear equation presented in Figure 6-4 and get the same result). This result is evidently in contradiction with observed β phase at 24 at.%. We can thus hypothesize that after reaching the critical concentration of Nb, the linear trend will no longer hold, but this hypothesis would need further confirmation with other samples in region close to α″/β transition.

Following the geometrical relations and the assumption that the lattice parameters of α″ are governed by $\{11\bar{2}\}\langle 111\rangle$ shear in former β phase (with a lattice parameter $a$), we could easily evaluate what difference in ratio of $b'/a'$ would this type of shear cause. However, this type of shear leads to the monoclinic distortion between adjacent $(100)_{\alpha''}$ and $(010)_{\alpha''}$ planes, which contradicts our results where we measured unit cell having orthorhombic symmetry. In the proposed transformation mechanism, the change of right angle between $[011]_{\beta}$ and $[100]_{\beta}$ can't be avoided by any specific magnitude of positive shearing distance (neglecting the twinning). In addition, such monoclinic transformation would be seen from XRD profiles, and above presented results are the proof that we didn't observe any phase with such crystal structure.

This crystallographic problem casts a bad light on proposed transformation mechanism, where the closest $(11\bar{2})_{\beta}$ planes only shear along each other in the $\langle 111\rangle$ direction. In order to correct this distortion, we decided to propose another approach joining the old $\{11\bar{2}\}\langle 111\rangle$ shear with a homogeneous strain, which would restore the 90° angle between adjacent $(100)_{\alpha''}$ and $(010)_{\alpha''}$ planes and kept the $\langle 111\rangle_{\beta}$ direction unrotated – the compressive strain parallel to the $\langle 11\bar{2}\rangle_{\beta}$ direction.

## 6.2 Alloys Ti-12Nb-(0-3)O

To see the influence of oxygen, we prepared 4 samples with constant Nb content (12 At.%) and varying oxygen content. Results are presented in the following chapter.

### 6.2.1 Polarized light microscopy

To see the microstructure of β/α″ phase in our samples, we performed measurements on SEM and Light microscope. Due to that martensite phase has the size of several hundreds of μm and can be nicely seen under polarized light due to

polarization effects associated with crystal orientation, we decided to present also several photos taken by this method.

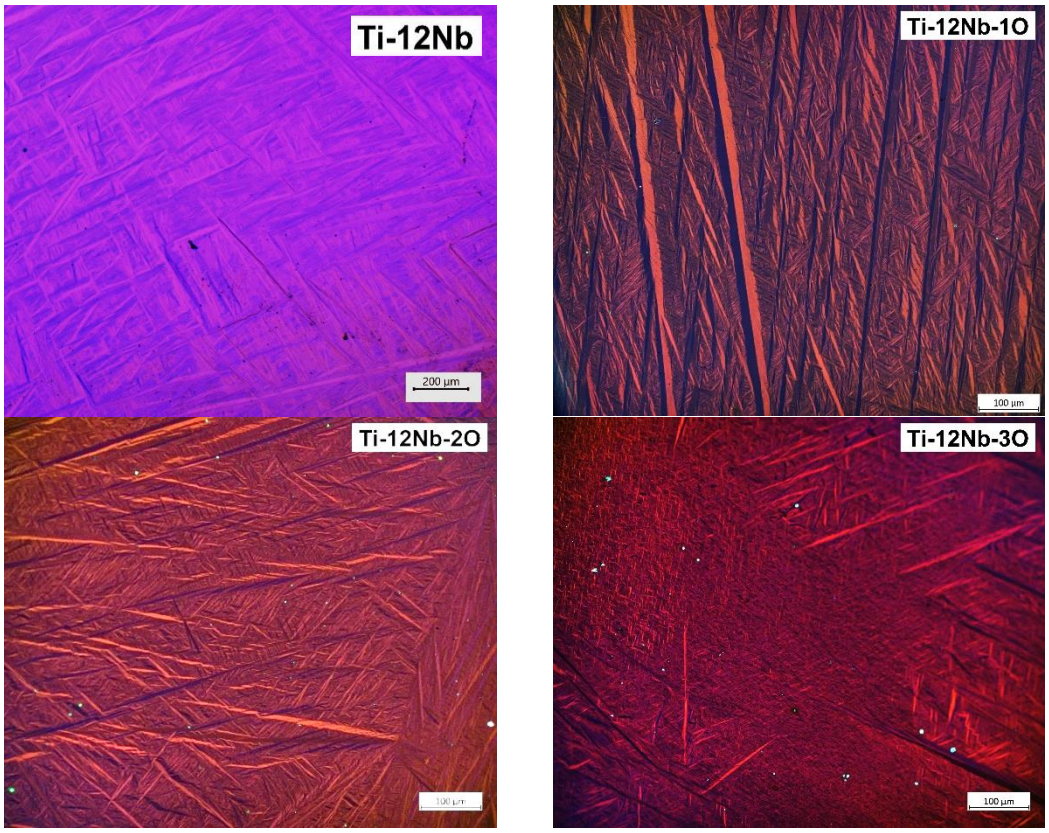


Figure 6-6 Micrographs of Ti-12Nb-xO samples

As we can see from the pictures at figure 6 – 6, all the micrographs have martensite present. Due to inhomogeneous distribution of α″ laths, we rather didn't evaluate anything quantitative information from the pictures. As we can see from Ti-12Nb-3O sample, α″ laths are much less homogeneously distributed compared to alloys with less oxygen. It is hard to say whether it is a direct effect of oxygen, but it is tempting to think that due to suppressive effect of oxygen towards β → α″ transformation, the oxygen atoms could decrease the possibility of long-range shear/shuffle and act like a barrier against growth of martensite. Another effect can be the Nb inhomogeneity, but because of relatively long-lasting solution treatment at high temperature, we do not expect that to be the case.

### 6.2.2 XRD

XRD measurements can reveal the true phase composition of our samples. As we can see from fig. 6-7, the ω phase was observed only in two samples. In case of

oxygen free Ti-12Nb and Ti-12Nb-1O, where in the last case we can see very small peak at $2\theta = 25°$. In case of Ti-12Nb-2/3O alloys, none of the ω peaks was observed. The martensite phase with many overlapping peaks was present in all the samples, as we can also see from the images presented in the last chapter. This is a clear proof that addition of oxygen supressed the ω phase formation in diluted Ti-Nb alloys.

From the pure XRD profiles we cannot see any significant change in structure parameters, as we would probably expect and as was also measured for example in [37]. This is most probably due to a weak effect of O on lattice parameters (O is an interstitial element). In the end, the effect of oxygen could be suppressed by other effects connected with change in lattice parameters, such as unperfect sample preparation connected with error in Nb content. We think that small unavoidable errors in Nb (~0.5 at.% of Nb) content indeed could cause bigger change in lattice parameters than due to the oxygen itself. Because of this, it is possible that true influence of oxygen on lattice parameters is obscured. The measured lattice parameter can be found in the appendix.

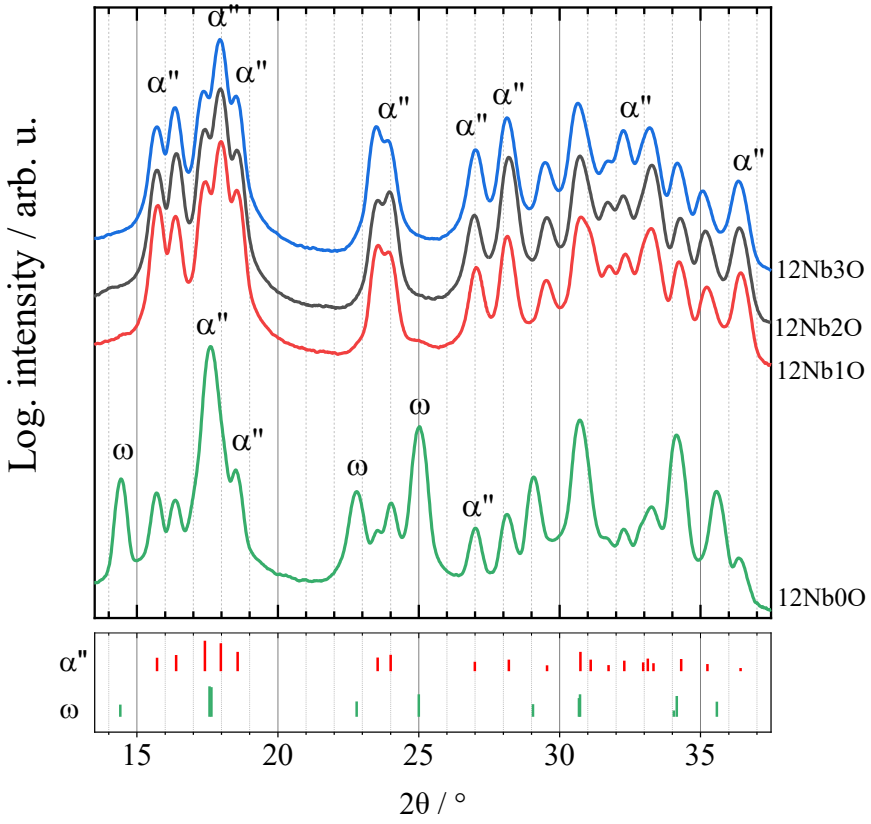


Figure 6-7 XRD integrated profiles over constant $2\theta$ angle of Ti-12Nb-(0-3)O

## 6.3 Ti-16Nb-(0-3)O

### 6.3.1 SEM

Clearly different results were obtained from Ti-16Nb-xO samples. Here we rather present micrographs taken by SEM, due to that α″ lamellae couldn't by observed by classical light microscopy.

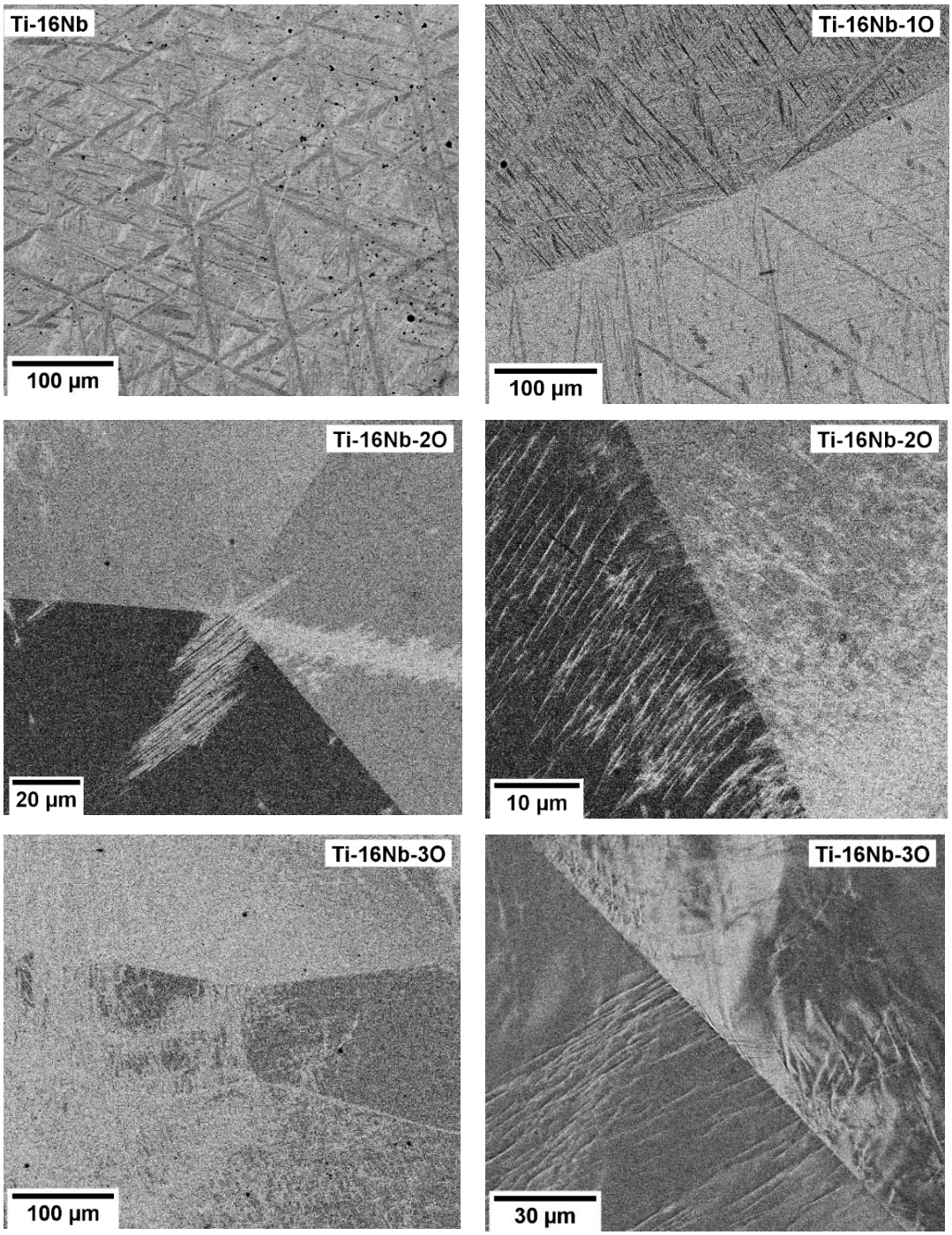


Figure 6-8 Micrographs of Ti-16Nb-xO alloys taken by SEM.

In samples with more oxygen content the β phase transformed into α″ only partially and we observed only a few regions which resemble lamellar morphology. As we can see from the figure 6-9, Ti-16Nb-2/3O alloys didn't transformed fully. Martensite like features were present at the grain boundaries, oriented in a characteristic way depending on the orientation of the parent β grain. In the first Ti-16Nb-2O picture, the triple point at the grain boundaries acts as a distortion nucleus for the formation of martensite. Gray features on the black background are very small α″ lamellae. The second picture from Ti-16Nb-2O sample shows the β grain boundary and small α″ lamellae nearby, all oriented in a similar way (in one grain) as we would expect due to direct relation with parent β grain. In the case of Ti-16Nb-3O sample, the martensite laths are very small and hard to distinguish. In the last photo of Ti-16Nb-3O sample, we can see small α″ needles at the grain boundary. The blending from a dark area to a light one within one grain on the right and striation like features on the left are most probably coming from the α″ laths and their unrevealed stress field.

### 6.3.2 XRD

XRD measurements enable us to identify even very small phases with only a little volume fraction, such as typically observed ω phase or presence of very small martensite. In Figure 6-10, we can see the diffraction profiles integrated over constant diffraction angle $2\theta$ of Ti-16Nb-(0-3)O alloys. As we can see, the 1 at.% addition of oxygen suppressed the formation of ω phase and the whole β phase transformed into α″ phase. Here we can again observe that oxygen inhibited the β → $\omega_{ath}$ transformation. After adding another 1 at.% of oxygen, the β phase remained present after quenching and oxygen atoms partially suppressed the β → α″ transformation. On the other hand, the ω phase was observed again as we can see from the peak at position 14.5°. It appears that 2 at.% oxygen addition partially suppressed the α″ and favoured the β → $\omega_{ath}$ transformation towards the martensite formation. Due to this, the unstable β phase rather transformed to the ω phase.

It can be deduced from the present phases that oxygen firstly enhanced the β → α″ transformation over the β → ω because of α stabilizing effect of oxygen, and when oxygen overcame a critical concentration, it induced the $\{110\}\langle 1\bar{1}0\rangle$ shuffle strong enough to suppress the $\{11\bar{2}\}\langle 111\rangle$ shear necessary for β → α″ transformation

in some regions. The unstable nature of the β phase was then reflected in the formation of ω phase when α″ couldn't be formed. Comparing the Ti-16Nb-2/3O samples, we can see a little decrease in the ω phase intensity. This can be another sign that after β phase retained in the sample, the oxygen addition indeed again suppressed the formation of ω phase. However, this hypothesis would need further analysis on more samples and more reliable measurement of peak intensities in order quantitatively compare them.

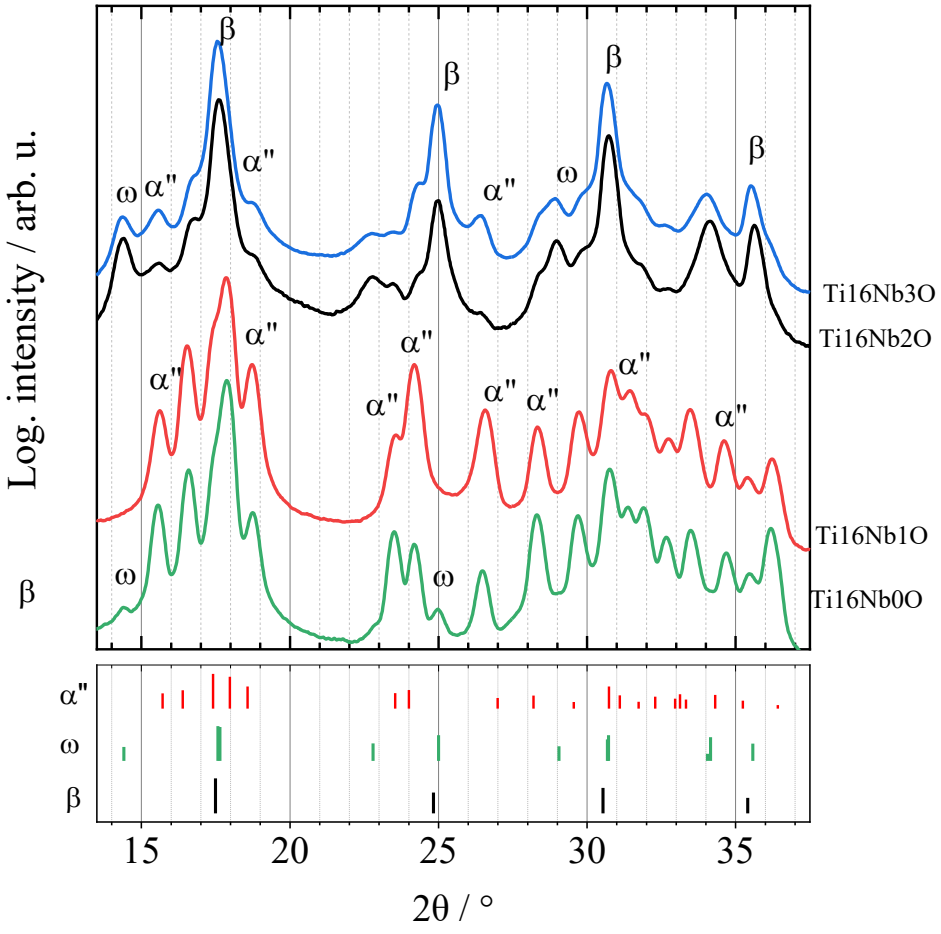


Figure 6-9 XRD integrated profiles over constant $2\theta$ angle of Ti-16Nb-(0-3)O

On the other hand, the presence of martensite and β phase in one sample allows us to evaluate the difference between these two phases and compare them how much do they follow geometrical relations. When we look at the Table 3 of lattice parameters determined from the XRD profiles, it can be clearly seen that even though there is a correspondence between $a_\beta$ and $a_{\alpha''}$, the $a_{\alpha''}$ is smaller than $a_\beta$ and $\frac{b}{\sqrt{2}}$ is bigger than

$a_\beta$ in both samples. In table 4, we can see that $\frac{c}{\sqrt{2}}$ parameter is almost the same as $a_\beta$ lattice parameter of β phase in both samples. This is a clear proof that the bcc structure gets contracted in $[100]_\beta$ direction and extends in the $[011]_\beta$ direction, but doesn't change much in the perpendicular $[0\bar{1}1]_\beta$ direction (these specific directions were chosen artificially only for demonstration, in fact we can choose any of the twelve variants of martensite and see proof the similar behavior).

Another interesting change can be observed when we try to compare the length of a base diagonal of α″ and body diagonal of β phase. If the only change of lattice parameters would be due to simple $\{11\bar{2}\}\langle 111\rangle$ shear, we wouldn't observe any change in this parameter. Furthermore, to see the change in direction parallel to the normal of $\{11\bar{2}\}_\beta$ plane, we can evaluate the distance $d_{112}$between the $\{11\bar{2}\}_\beta$ planes and corresponding $\{110\}_{\alpha''}$ planes in martensite (distance between $\{110\}_{\alpha''}$ planes should be then equal to the 2 times the distance between $\{11\bar{2}\}_\beta$ planes). This distance can be calculated using the simple equation from theory of crystallography. In case of the orthorhombic phase, it holds:

$$\frac{1}{d_{hkl}^2} = \frac{h^2}{a^2} + \frac{k^2}{b^2} + \frac{l^2}{c^2}.$$

Since cubic lattice is just a special case of orthorhombic lattice, we can put $b = a$ and $c = a$ and get the valid equation for parent bcc β phase. If no effect perpendicular to the shear is present, we should get similar results in both α″ and β phase.

Table 3. Measured lattice parameters of martensite and parent β phase from the XRD profiles at figure 6-10. Standard deviations were automatically calculated by the software.

| Sample | $\alpha''$ martensite | | | | | | | β phase | | |
|---|---|---|---|---|---|---|---|---|---|---|
| | $a$ [Å] | $\sigma_a$ [Å] | $b$ [Å] | $\sigma_b$ [Å] | $c$ [Å] | $\sigma_c$ [Å] | $d_{110}$ | $a_\beta$[Å] | $\sigma_a$ [Å] | $2d_{112}$ |
| Ti16Nb2O | 3.134 | 0.004 | 4.891 | 0.007 | 4.65 | 0.01 | 2.639 | 3.283 | 0.001 | 2.680 |
| Ti16Nb3O | 3.115 | 0.004 | 4.888 | 0.007 | 4.68 | 0.01 | 2.627 | 3.291 | 0.001 | 2.687 |

Table 4. Corresponding parameters between β and α″ phase suitable for their comparison.

| Sample | α″ martensite | | | | | β phase | |
|---|---|---|---|---|---|---|---|
| | $a$ [Å] | $\frac{b}{\sqrt{2}}$ [Å] | $\frac{c}{\sqrt{2}}$ [Å] | $\sqrt{a^2+b^2}$ [Å] | $\tan^{-1}\left(\frac{\Delta b}{\Delta a}\right)$ | $a_\beta$ [Å] | $\sqrt{3}a_\beta$ [Å] |
| Ti16Nb2O | 3.134 | 3.459 | 3.286 | 5.81 | 49.78 | 3.283 | 5.686 |
| Ti16Nb3O | 3.115 | 3.456 | 3.309 | 5.80 | 43.26 | 3.291 | 5.700 |

Calculated values are presented in tables 3 and 4. Again, we can see the discrepancy between expected and measured results - $\{110\}_{\alpha''}$ planes are closer to each other than $\{112\}_\beta$ planes, but from the proposed simple shear mechanism, we would expect the same distance. Similar thing can be seen comparing the base diagonal of α″ and body diagonal of β phase. Here we see the elongation in the $\langle 111\rangle_\beta$ direction. Those are all clues that that proposed shear mechanism is not totally correct and doesn't completely describe the pathway of lattice parameters change in β → α″ transformation. Because the distance between $\{110\}_{\alpha''}$ planes shrinks, it is a clear sign that the transformation doesn't only follow the $\langle 111\rangle_\beta$ direction. Thus, we tried to specify in what direction the transformation flows by comparing the change of corresponding *a* and *b* lattice parameter following the geometrical formula:

$$\tan^{-1}\left(\frac{\Delta b}{\Delta a}\right) = \tan^{-1}\left(\frac{b_{\alpha''} - \sqrt{2}a_\beta}{a_\beta - a_{\alpha''}}\right).$$

The angle between $[111]_\beta$ and $[100]_\beta$direction is approximately equal to 54.74°. Comparing this value to the values calculated for the lattice parameters in table 4, we can see that the measured angles are more inclined to the $[100]_\beta$direction by more than 4° and 10° for Ti16Nb2O and Ti16Nb3O, respectively.

## 6.4 Ti-20Nb-0/2/3O

The last set of samples with different amount of oxygen contains the highest content of Nb: 20 At.%. Unfortunately, as will be described in the following section, the Ti-20Nb-1O sample was found to contain lutecium impurities, most probably due to insufficiently cleaned vacuum arc melting equipment from previous colleagues. Thus, we didn't measure XRD profile on this sample.

### 6.4.1 Polarized light microscopy and SEM

In this chapter, we will describe the evolution of microstructure with increasing oxygen content in samples with constant 20 at.% of Nb, similarly as we did in the previous chapters. Results can be seen in Figure 6-10, where we present all Ti-20Nb-0-3O samples. The first picture with Ti-20Nb composition was already presented using SEM in the chapter about oxygen free samples. Here we can see the similar microstructure taken by polarized light microscopy. It can be seen than the sample fully transformed to α″ phase, and individual martensite laths can be distinguished due to change of polarization while reflecting from different variants of martensite. Another interesting thing is that we cannot recognize any twinning in the sample as we did in case of the Ti-12Nb sample. As will be discussed further, this observation is not a coincidence and is significantly related to the proportion of elongation in the $[001]_{\alpha''}$ direction as can be explained by PTMC theory.

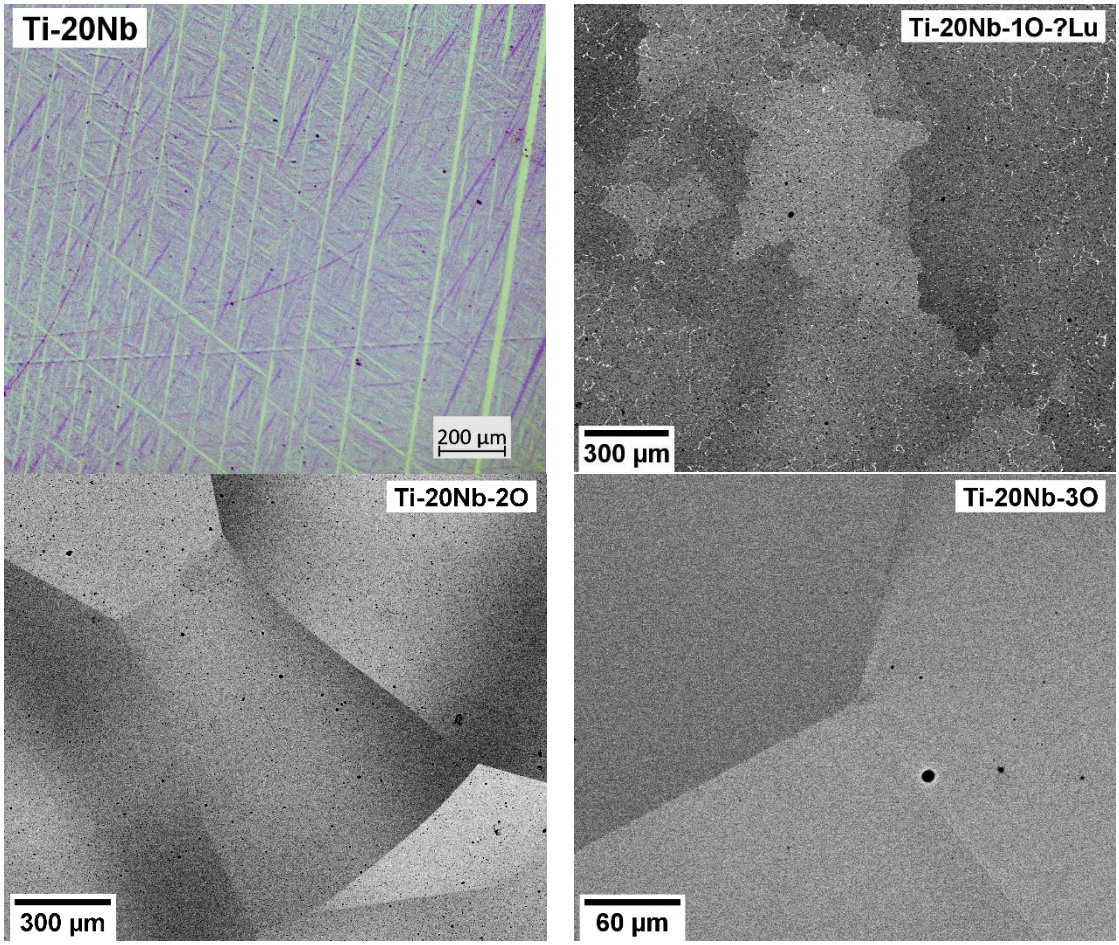


Figure 6-10 Micrographs taken by polarized light microscopy (Ti-20Nb) and SEM. The bright spots at Ti-20Nb-1O sample are lutecium particles.

In case of Ti-20Nb-1O sample, we rather used SEM and we unexpectably observed bright spots at the edges of the grains. This image was taken using the BSE detector, and because these spots appear much brighter, the first idea was that they are some heavy impurities which contaminated our sample during arc melting. To verify this assumption, we performed the EDX analysis and found out that the mysterious particles contain lutetium. It is now clear that the contamination occurred during sample preparation during arc melting due to an insufficiently cleaned crucible. After finding this we didn't perform any other experiments on this sample.

The last samples with highest amount of oxygen Ti-20Nb-2O and Ti-20Nb-3O were fully β stabilized and we didn't observe any martensite in these samples. As we can see from the bottom two pictures, the β phase is present along the whole sample and we do not see any intensity changes even at the grain boundaries. In order to detect the ω phase, we need to perform XRD analysis. Both pictures at Figure 6-10 were taken via SEM.

### 6.4.2 XRD

Real crystal structure with potential presence of ω phase can be reviled using X-ray diffraction. Compared to the α″ phase whose peaks move due to change in lattice parameters, $\omega_{ath}$ phase is not so sensitive to the chemical composition in terms of change in lattice parameters.

As mentioned in the previous chapter. It is interesting that Ti-20Nb sample didn't contain an ω phase, even though this phase was present in all Ti-(8-16)Nb samples. Even the oxygen level is almost the same for all above mentioned samples, so there is a high possibility that ω phase was simply suppressed sooner that β→α″ transformation and thus diagram presented in Figure 2-3 is not completely correct. Only this could explain why the only present phase was the α″ martensite. After increasing the oxygen content to about 2 at.%, the martensite was fully suppressed, which agrees with BSE images made via SEM and the only detected phases were β phase and little bit of ω phase. It is worth to note that the similar behaviour could be seen in Ti-16Nb-1/2O samples, where ω phase was firstly suppressed by oxygen atoms but then at 2 at.%, after suppression of α″ phase, it appeared again. This can be the same case, when unstable β phase rather transformed to ω phase than martensite.

Oxygen induced $\{110\}\langle 1\bar{1}0\rangle$ shuffle suppressed the $\{11\bar{2}\}\langle 111\rangle$ shear necessary for β → α″ transformation and thus inhibited the β→α″ transformation.

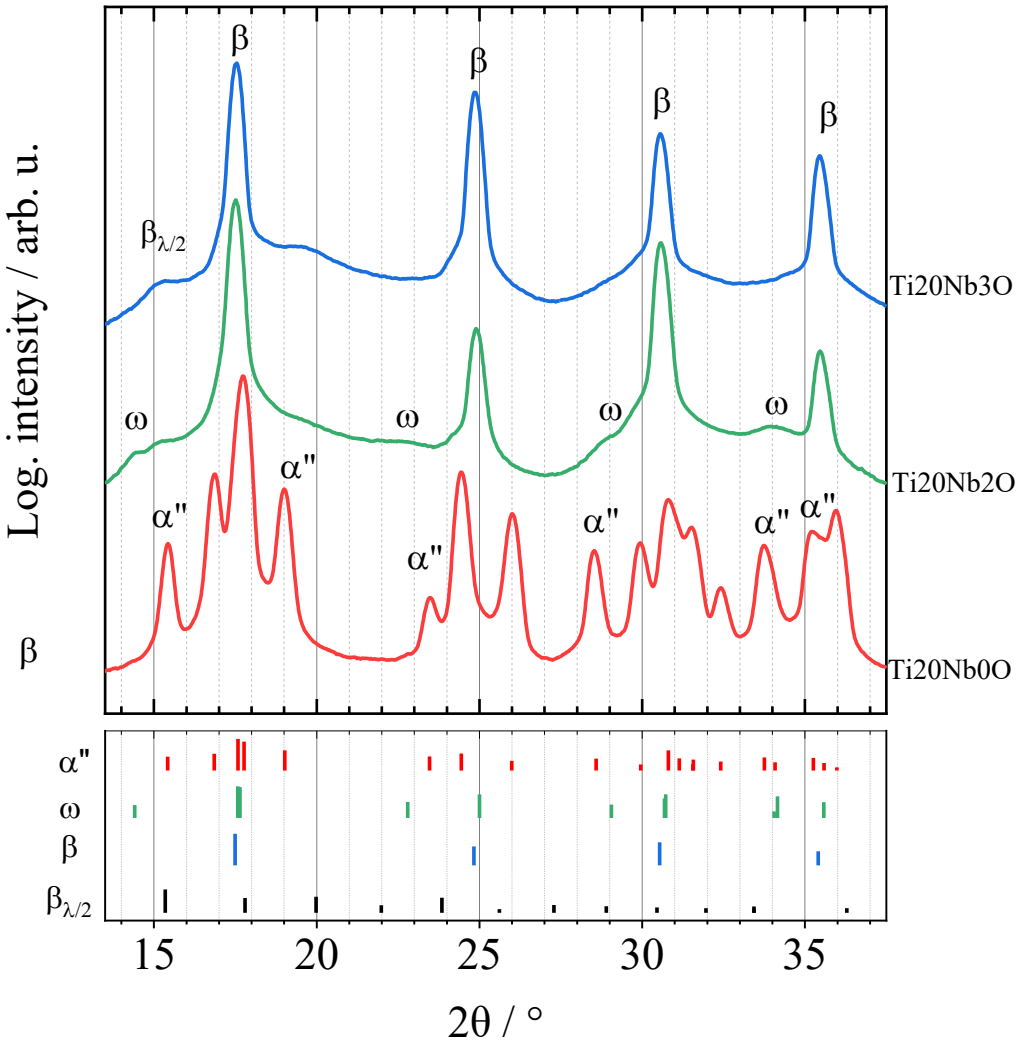


Figure 6-11 XRD integrated profiles over constant $2\theta$ angle of Ti-20Nb-0/2/3O samples.

In case of the last sample, we can see clear β peaks and no ω peaks at expected positions. This is another proof that additional oxygen suppresses ω phase in the samples with present β phase. Even though we can not see any ω peaks, there is some clear additional peak at 15.2°. This peak shouldn't belong to the ω phase as we can see from the legend at the bottom graph. In fact, this high energy peak does no belong to any different phase than already presented β phase. Simulation of the powder diffraction profile of β phase (presented at the bottom of the figure 6-12) reveals that the peak around 15.2° comes from the higher energy diffraction of photons with half

the wavelength of our primary photons from molybdenum anode. This wavelength can't be suppressed by crystal monochromator and is usually responsible for a weak background which we can ignore. However, in this case the unwanted peaks can be observed at unexpected angles what may easily lead to misinterpretation in terms of correct crystal structure determination. By looking at the $\beta_{\lambda/2}$ peaks positions we can see that even in case of Ti-20Nb-2O sample we may observe some addition peak at 15.2° right next to the ω peak as well.

Even though both samples Ti-20Nb-2O and Ti-20Nb-3O have high energy $\beta_{\lambda/2}$ $\{211\}$ peak at 15.2°, what remains unclear is the little wide peak at around 19.5° in Ti-20Nb-3O sample, which cannot be observed that clearly in the case of Ti-20Nb-2O sample. By looking at the $\beta_{\lambda/2}$ peaks positions produced by high energy wavelength, this peak can be attributed to $\beta_{\lambda/2}$ peak at around 20° comming from the $\{310\}_{\beta}$ planes. The standard peak from $\{310\}_{\beta}$ planes from normal wavelength should be located at around 40° (not shown on the graph).

## 6.5 EBSD measurement on Ti-12Nb-1O

Twinning is an important deformation mode not only in low crystal symmetry systems such as pure Ti but also in high crystal symmetry systems. It is very common among the metastable martensitic phases that they exhibit twinning during loading or quenching. This mechanism of reorientation of crystal structure without change in lattice parameters can easily accommodate strain arising during quenching or deformation and usually leads to the formation of undistorted plane. From the materials perspective, the large growing martensite lath becomes usually unstable after reaching some critical width/length due to increasing strain inside the structure and inability to withstand compressive and tensional forces acting on the lath from different directions. Because we want to be sure that all martensites follow the orientation relations used in the simulation of XRD reciprocal space, we decided to further perform child → parent reconstruction and check whether all martensite laths will transform into the β grain with the same orientations.

When we look at the figure 6-13 taken by polarized light microscopy, we can clearly see wide martensite laths oriented in different directions with respect to each

other. According to the orientation relations, there shouldn't be more than 12 different orientations if all region belongs to the same parent β grain. Some of the laths are clearly 'bend' around yellow lines, as wee can see from laths with black colour on the picture. Those are most probably twin boundaries inside α″ lamellae which arose during quenching. To verify this, we performed EBSD analysis on the same sample in the region defined by yellow rectangle (the picture is just inverted). The final EBSD map can be seen in Figure 6-14. Misorientation profile along the yellow line is represented in the Figure 6-15.

From the measurement of misorientation angle between 3 different grains of martensite, it is clear that they are misoriented about 90° angle with certain deviation around 5°. The deviations about 2° from orientation relations are normally reported in the literature [7]. It is possible that both neighbouring α″ grains have been deviated about the similar angle from the orientations relations and by measuring their difference we only summed up twice the reported number. Proof that not only macroscopic twins can be observed can be seen on the Figure 6-13 for example. Here we can see SEM image of Ti-12Nb-3O sample on the right side with two differently oriented variants α″ martensite with inner twins. Sudden periodical change in intensity is visible thanks to the channelling contrast. This indicates that black laths are twinned structure within the one primary martensite grain. In the left picture we can also distinguish twins inside some grains, mainly in the big diagonal variant with perpendicular twins inside.

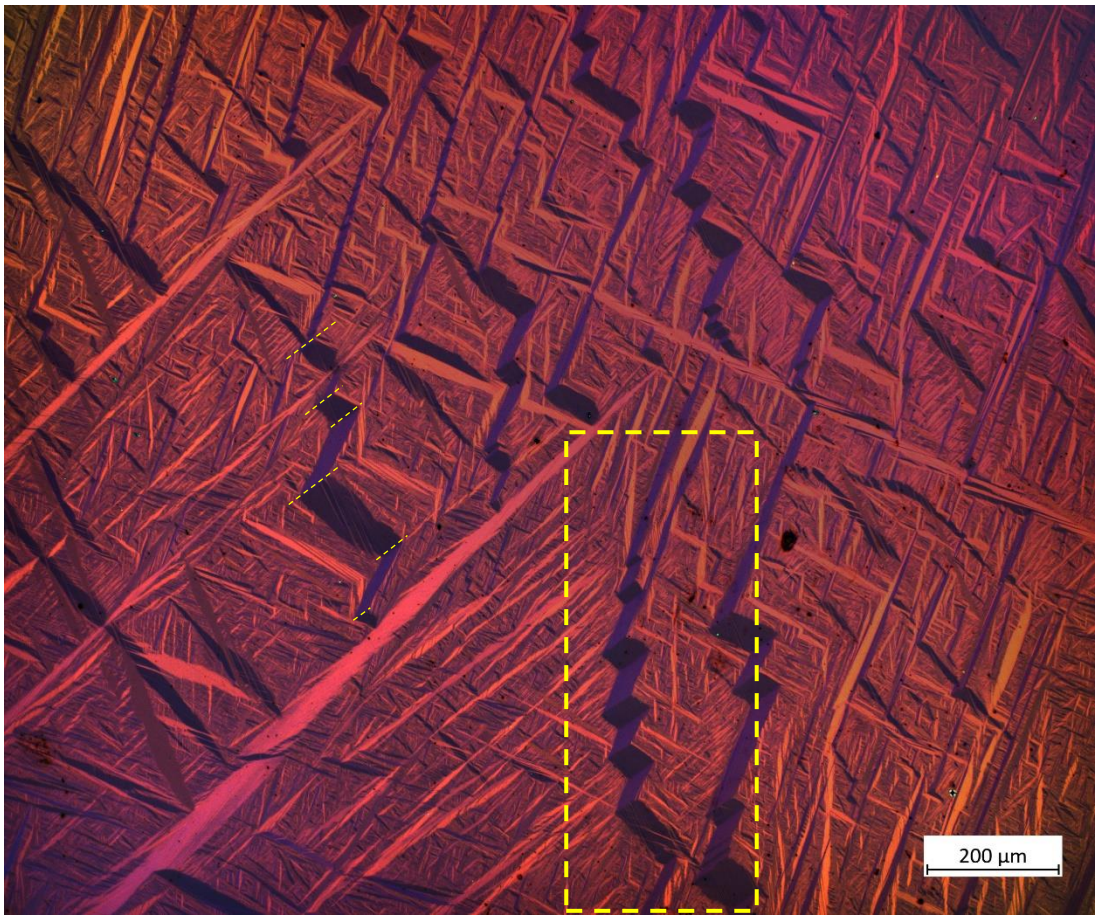


Figure 6-12. Microstructure of martensite in Ti-12Nb-1O sample. Picture was taken via polarized light microscopy. Yellow rectangle represents the region where EBSD analysis was performed.

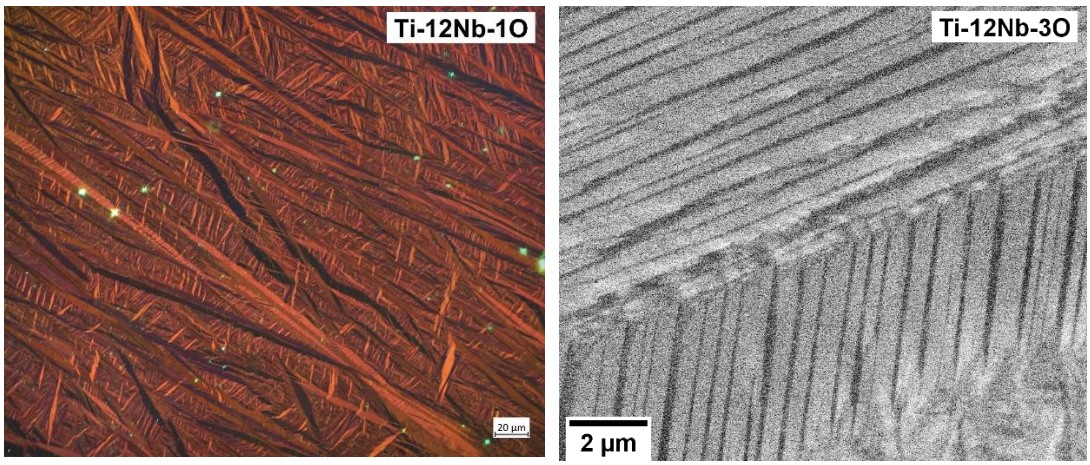


Figure 6-13 Microstructure of Ti-12Nb-1/3O under the higher magnification. Polarized light microscopy on the left, SEM on the right.

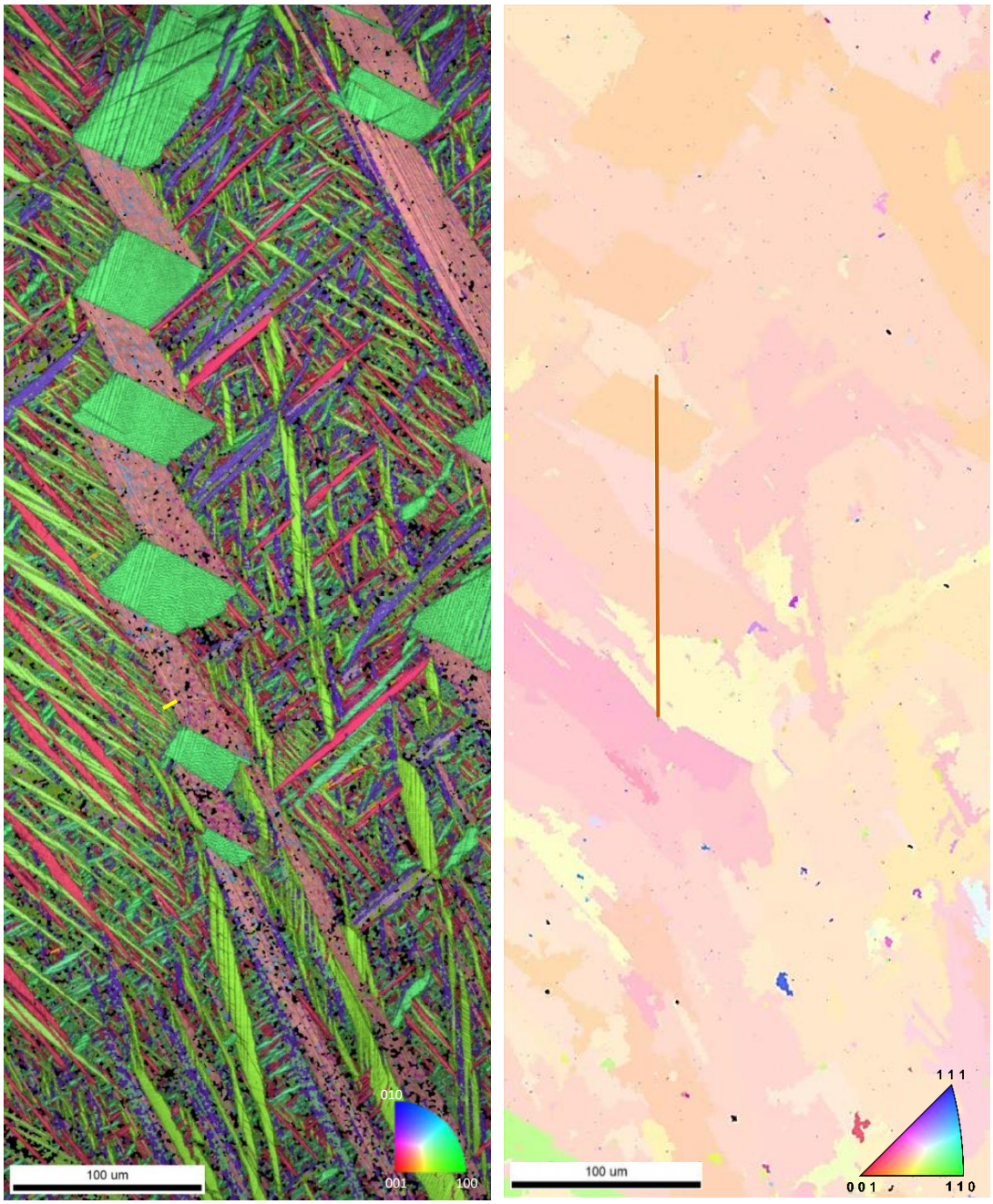

Figure 6-14. On the left size, EBSD map of Ti-12Nb-1O sample. On the right side, EBSD map after reconstruction to parent β phase following the orientation relations. EBSD map is grey scaled according to image quality number. All points with too low confidence index <0.05 were discarded. Misorientation profiles in figure 6-15 were evaluated along yellow and brown lines.

Looking at the EBSD map from Ti-12Nb-1O sample, we can see the individual part of twins coloured with pale red/green. As can be noticed also from the Figure 6-12, the red line parts are little bit longer compared to the individual green parts. Furthermore, unlike the green one ending at the boundary, red grain continues further

to the structure. Following these arguments, it is more likely that the red grain parts used to be the parent martensite which transformed during quenching via twinning mechanism into the green parts and not vice versa. Smaller green/pink/purple martensite grains on the left side are most probably other variants of the same martensite structure. Qualitatively saying, it seems that bigger the lath is, more probably the twin will occur inside the growing martensite. Another thing worth to mention is the inner structure of several bigger grains. Looking at the pale green twin grain at the top of the picture, we can notice purple bands parallel to each other, getting bigger while leaving the grain. Those can be some addition twins/martensite variants which arose during formation of twins inside the grain.

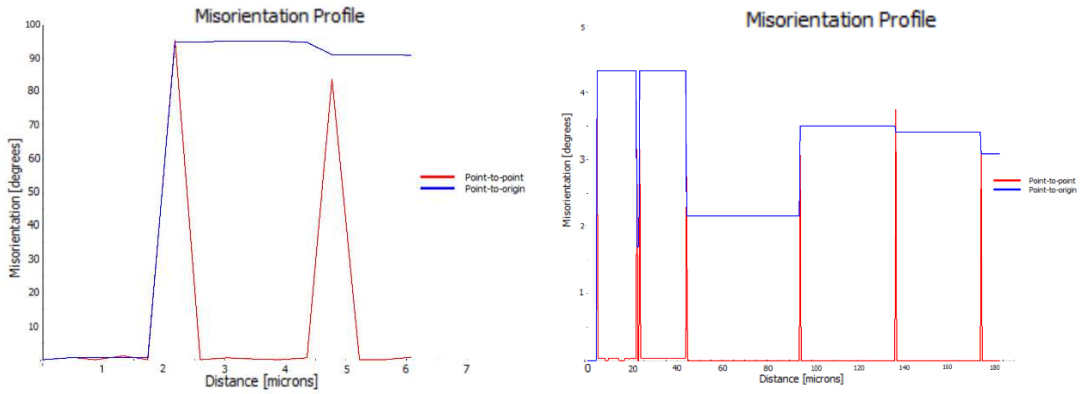


Figure 6-15 Measured misorientation angle across the EBSD map of Ti-12Nb-1O sample. The left picture represents the grains before reconstruction, the right picture after reconstruction.

To verify whether all the grains belong to the same parent β phase, we performed α″ → β reconstruction using the predefined function in OIM analysis tool. Software uses Orientation relations as and input (in our case we used the relations described in the theory) and tries to calculate the most probable parent β grain orientation. As we can see from the result picture on the right side of Figure 6-14 (Grains were dilated into the place where no data were provided). It is clear from the inverse pole figure triangle that similarly coloured grains have similar orientation. This can be even better visualized by measuring the misorientation angle across the grains (brown line in Figure 6-14), presented in the right side of Figure 6-15. The angle of misorientation stays under the 5° across the 100 $\mu m$ long line, what is the good result with the agreement that all α″ grains approximately follow the proposed relation with the parent β grain. Small grains with totally different orientations can be also noticed,

but looking at their size and arrangement we can consider them to be an error made during measurement of primary EBSD map.

## 6.6 Reciprocal map indexation

To distinguish individual variants of martensite from each other, we simulated the reciprocal space in the range from $(\bar{7}\bar{7}\bar{7})_{\alpha''}$ to $(777)_{\alpha''}$. All vectors with very low intensity were neglected at very beginning to now slow down the calculations. As was described in the chapter about the way of indexation, it can be described in several steps. Now, we will present the whole procedure on a Ti20Nb sample.

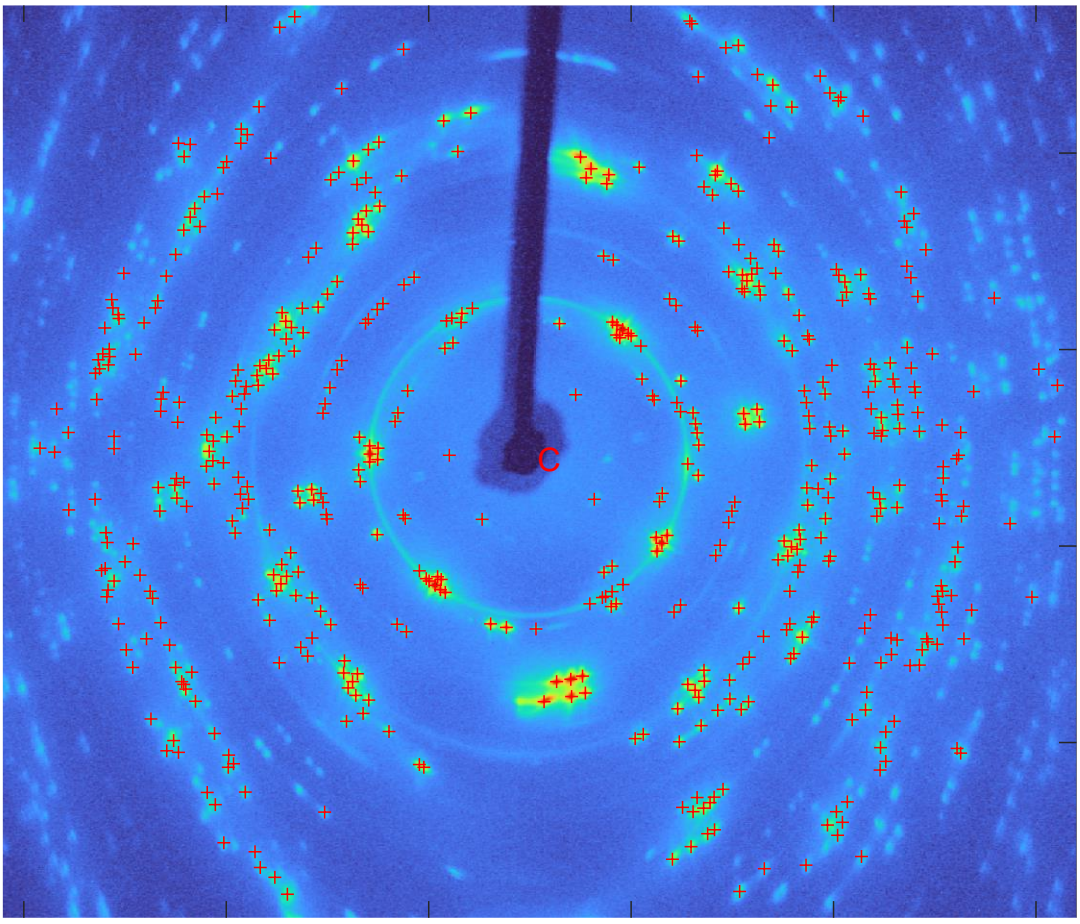


Figure 6-16. Measured signal on 2D XRD detector. Deviation in the horizontal range is equal to the typical $2\theta$ angle. Red crosses represent found location of peaks.

The first necessary step was to identified the $2\theta$ and β angles of all measured peaks. For that we used find peaks function with threshold values on peaks intensity and prominence. As we can see from Figure 6-16, not all peaks have been found by our

algorithm mainly because of the high threshold we have set on intensity to avoid unwanted peaks. However, this does not bother us because we still have quite high number of other peaks suitable for comparison with simulation.

In the next step, we let the next algorithm to simulate our experiment. Because we didn't know the initial orientation of our sample, our algorithm was simulating many diffraction patterns which would arise during rotation of the sample within [-30°, 30°] around the horizontal axis. This was done several thousand times with different initial orientations of parent β crystal – from which we always derived 12 variants of martensite according to the orientation relations. After several tens of minutes, we got the result drawn in Figure 6-17.

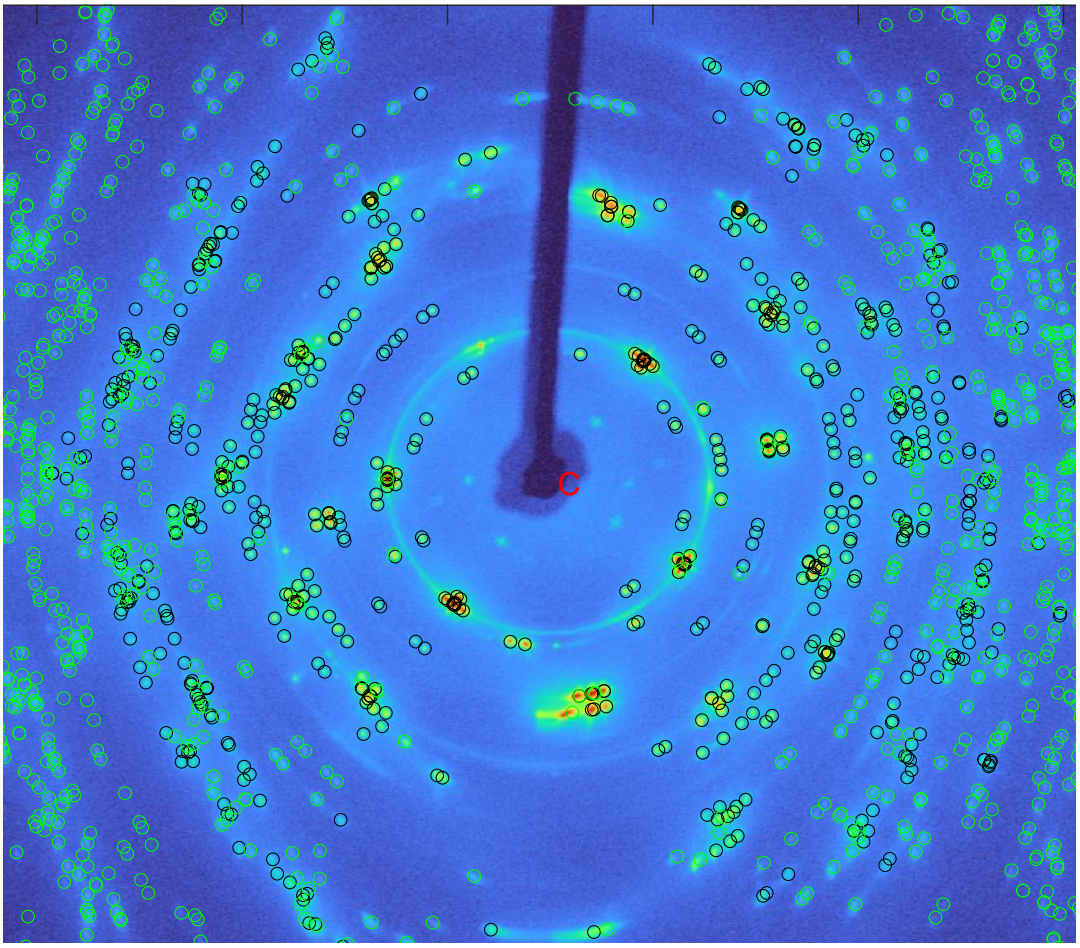


Figure 6-17 XRD measurement overlayed by black circles – matched pairs of reciprocal points generated by simulation and red crosses; and green circles – predicted positions of spots which should be measured within [-30°, 30°] rotation.

We can see from the resulting simulated patter that most points were matched with a good precision and predicted positions are with a good agreement with the

measured reciprocal map. Even though there can be found some points which are present at the map but were not predicted by the simulation, it can be the case that these spots were generated at the edge of the [-30°, 30°] range of rotation ant thus due to precision of our measurement don't have to be included in our simulation. The other limits come from the errors within experimental arrangement. We are limited by the precision of sample preparation, which due to low thickness could be easily bend and thus affect peaks width. Another factor is the precise adjustment of the eccentric position. Even though it should be located at the centre of the goniometer, it is not easy to perfectly adjust the sample title around axis perpendicular to the primary beam. This and more geometrical errors could contribute to the unprecise positioning of the sample during the experiment. Because it is hard to quantify such errors, we decided to keep them within statistical mistakes.

This is how we managed to index the reciprocal map in the case of samples which did not contain any phase other than α″. In the case of samples containing beta or omega phase, we could not successfully index the reciprocal space due to large errors caused by the presence of extraneous peaks. As a result, the possibilities of determining the crystal structure were narrowed down to only 4 samples, namely Ti-20Nb, Ti-12Nb-1/2/3O and Ti-16Nb-1O.

## 6.7 Quantitative analysis of $\{110\}_{\beta}\ \langle 1\bar{1}1\rangle_{\beta}$ shuffle via XRD

After indexing the reciprocal map successfully, we proceeded to the final step, which involved integrating individual diffraction maxima and calculating the absolute value of the structure factor. To be able to reliably determine the integral intensity of individual peaks and subtract the background, we fitted the reciprocal points with the sum of two functions: a plane and a Gaussian function. In the end, we used only the pure Gaussian function to determine the integral intensity, which we numerically integrated after determining the relevant parameters for each measured reciprocal point. The fitting function we used was an elliptic gaussian function with the option of tilting against the x-axis.

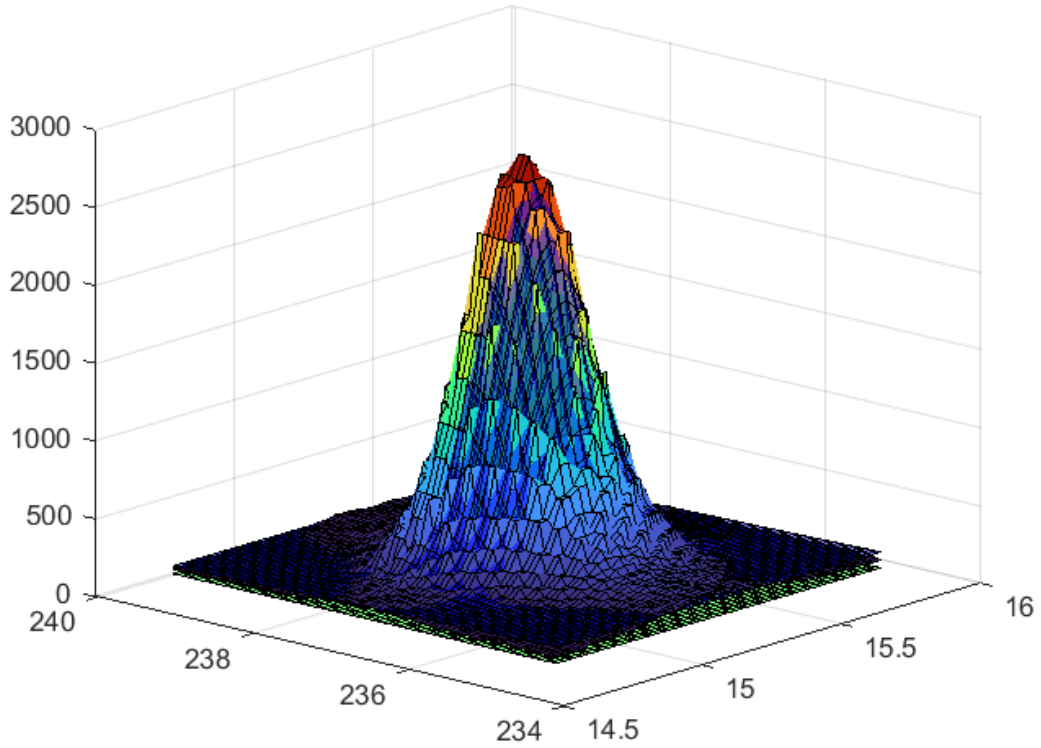


Figure 6-18 Fitted intensity curve onto one of the peak - blue function. Bottom green function is the pure Gauss function used for the integration.

The last step was to evaluate the integral intensities using the equations described in the introductory chapter. To avoid overlaps between individual peaks, we only considered integral intensities that were located far enough from other peaks predicted by the simulation. To ensure a low error rate, we also calculated an error of

Gaussian fit for each peak, which helped us to decide whether to accept or reject the given intensity for further calculation. During fitting, we used four parameters namely $I_0, y, B_{Ti}, B_{Nb}$; whose meaning was described in the theory and experimental method.

Due to the complexity of simulation and high probability of obtaining errors due to many calculation steps we decided to use and compare two approaches for calculating the crystal structure, as each of them has its limitations.

- The first method was based on averaging all observed structure factors among all 12 variants. The way of calculation is presented in the following flow chart.

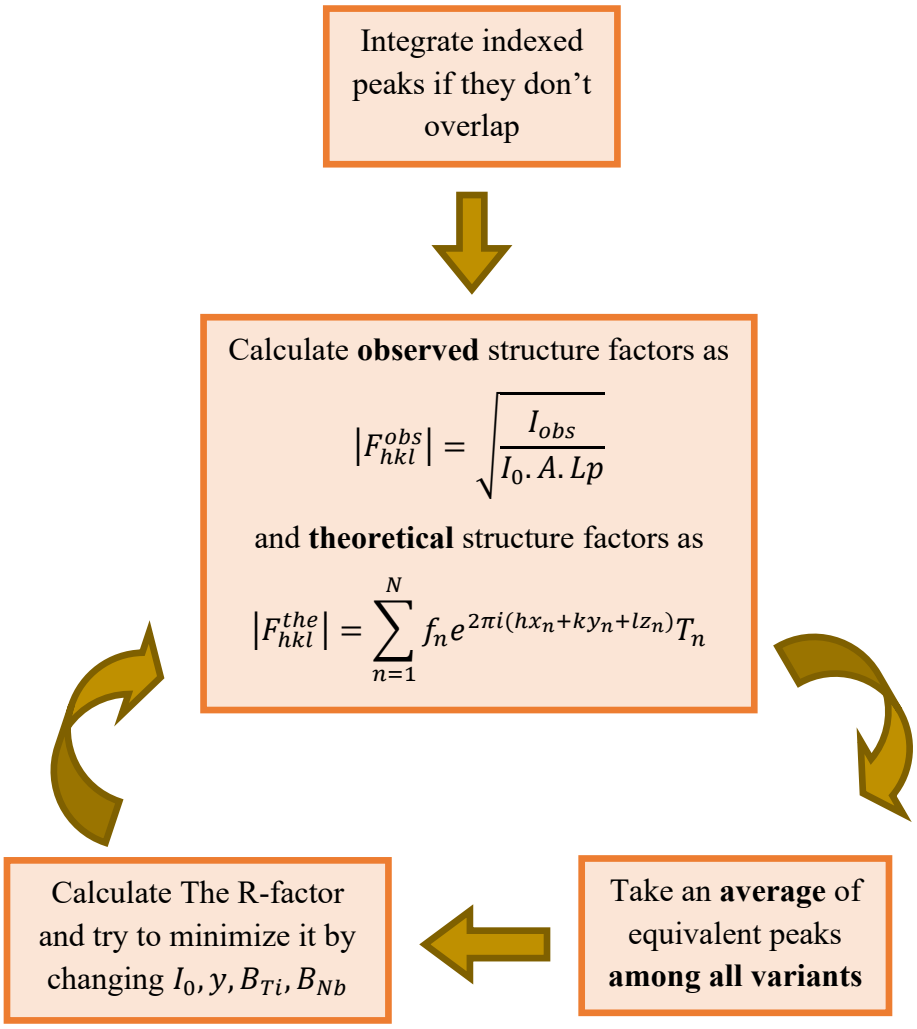


Its main advantage is that it averages and compares up to 140 integral intensities, thanks to which we avoid overfitting and thus it can provide a good view of all fitting constants. However, its main disadvantage it that it automatically assumes a

homogeneous distribution of all variants in the sample, what is a relatively strong condition. To account for this fact, the second model works a little differently.

- The second method tries to take all variants individually and calculates $I_0, y$ parameters separately for every variant, 12 times.

This approach avoids the problem of constant distribution of individual martensite variants. However, as the overlapping of individual peaks is relatively frequent, the number of integral intensities for each variant is around 10. After subsequent averaging due to symmetry, this number may decrease even more. Because of that it is hard to avoid overfitting when using four parameters in total. In order to limit our fitting at least a little, we fixed the Debye-Waller thermal factors ($B_{Ti}, B_{Nb}$) at the values that came out of the measurement using the first method. Thus, we reduced the fitting parameters from 4 to 2. The fitted parameter $y$ was the averaged across the 10 variants – The 2 variants deviating the most from the average were omitted for the statistical reasons.

The individual data created by first method are presented in the appendix, In table 5 we present quick overview how does the table look like for sample Ti-20Nb. We can see that observed and calculated structure factors match quite well. Individual errors between predicted and calculated structure factors are of the same order as the error as observed structure factors. Values with too huge error were discarded and did not contribute to the result of the fit. Observed structure factors with missing standard deviation are composed of only one integral intensity from the reciprocal map.

The summarizing factor which evaluates the quality of the fit is presented at the bottom. For the sample Ti-20Nb, it reached the lowest value among all the samples, approximately $0.04$. According to the literature [45], measured structure with R-factor value around 0.05 or lower is considered a good solution. From our point of view not only R-factor but also the number of data should be a relevant parameter for stating whether the structure was solved correctly or not.

Table 5. Comparison between observed and calculated structure factors for Ti-20Nb sample with standard deviation calculated using equivalent reciprocal points. The fitting parameter $I_0$ have been kept constant – the first method approach.

| $\left\|\overline{F_{hkl}^{obs}}\right\|$ | $\left\|F_{hkl}^{the}\right\|$ | $\sigma_{\left\|\overline{F_{hkl}^{obs}}\right\|}$ | $h$ | $k$ | $l$ | $\left\|\left\|\overline{F_{hkl}^{obs}}\right\| - \left\|F_{hkl}^{the}\right\|\right\|$ |
|---|---|---|---|---|---|---|
| 16.69 | 16.50 | 0.84 | 1 | 1 | 0 | 0.20 |
| 26.82 | 26.82 | 1.55 | 0 | 2 | 1 | $< 0.01$ |
| 9.52 | 10.89 | 1.26 | 1 | 1 | 2 | 1.37 |
| 20.76 | 21.87 | 1.81 | 1 | 3 | 0 | 1.11 |
| 20.07 | 20.60 | 0.52 | 1 | 3 | 1 | 0.53 |
| 24.32 | 23.13 | 2.70 | 2 | 2 | 0 | 1.19 |
| 12.28 | 12.70 | 2.97 | 0 | 2 | 3 | 0.41 |
| 10.81 | 12.00 | 1.55 | 2 | 2 | 1 | 1.19 |
| 15.72 | 15.51 | 1.96 | 1 | 3 | 2 | 0.21 |
| 11.23 | 11.23 | – | 0 | 4 | 0 | $< 0.01$ |
| 17.17 | 17.17 | 3.38 | 0 | 4 | 1 | $< 0.01$ |
| 4.32 | 3.90 | – | 1 | 1 | 4 | 0.42 |
| 3.54 | 3.52 | – | 3 | 1 | 0 | 0.02 |
| 5.37 | 6.35 | 0.71 | 2 | 2 | 3 | 0.98 |
| $y = 0.209$ | | $I_0 = 192.26$ | | Ti-20Nb | | R = 0.04 |

The second way of fitting is based on taking individual variants separately and comparing them (averaging in the case of y parameter) after the evaluation of fitting parameters. In this case, to avoid overfitting we used only $I_0$ and $y$ as two fitting parameters. This method of calculation should thus be more reliable, as it does not assume a homogeneous distribution of individual variants. Fitted values for the ti-20Nb sample showing 10 separate variants are shown in Table 6.

Table 6 Results from fitting individual variants of martensite separately. Sample Ti-20Nb.

| Parameter | Variant | | | | | |
|---|---|---|---|---|---|---|
| | 1 | 2 | 3 | 4 | 5 | 6 |
| y | 0.207 | 0.212 | 0.209 | 0.211 | 0.210 | 0.206 |
| I | 203 | 192 | 192 | 203 | 192 | 192 |
| R – factor | 0.11 | 0.11 | 0.10 | 0.14 | 0.11 | 0.10 |

| Parameter | Variant | | | | Average | $\sigma$ |
|---|---|---|---|---|---|---|
| | 7 | 8 | 9 | 10 | | |
| y | 0.208 | 0.212 | 0.222 | 0.218 | 0.212 | 0.005 |
| I | 210 | 174 | 192 | 296 | 205 | 33 |
| R – factor | 0.06 | 0.14 | 0.05 | 0.11 | 0.10 | 0.03 |

The comparison of both approaches is presented in Table 7, where we can see predicted values of y parameter together with R parameter and a standard deviation in the case of second method. By comparing the R factors, it is clear that method 2 exhibits a higher error rate compared to Method 1. Specifically, the error rate for Method 2 is approximately 0.13, while for Method 1 it is generally lower but more variable. When comparing the y parameters obtained by both methods, it can be seen that the individual values do not differ that much and all values are within an error, except for the one sample - Ti12Nb3O. We will discuss this sample in a little more detail.

Looking at the Table 7, we can see structures determined by method 1 have R-factors lower than in the case of method 2. Comparing the individual $\sigma$ values, among all samples the Ti12Nb3O has surprisingly the lowest deviation. Also worth to mention is that in case of method 1, the R-factor is on the contrary the highest. The reader can find more details about this sample and specific numbers in the appendix of this work. However, the results of the fitted intensities indicate that the greatest variance in the $I_0$ parameter compared to all the investigated samples is exactly in this sample (Standard deviation is about 100, what is 3 times higher compared to the Ti20Nb).

Table 7. Table showing the difference between results obtained by first and second approach.

| Method | 1 – averaging the structure factors among all variants | | 2 – averagin the resulting parameters | | |
|---|---|---|---|---|---|
| Sample | y | R | $\bar{y}$ | $\sigma_y$ | $\bar{R}$ |
| Ti12Nb1O | 0.186 | 0.12 | 0.184 | 0.003 | 0.16 |
| Ti12Nb2O | 0.184 | 0.09 | 0.189 | 0.008 | 0.12 |
| Ti12Nb3O | 0.174 | 0.19 | 0.185 | 0.002 | 0.13 |
| Ti16Nb1O | 0.196 | 0.16 | 0.197 | 0.006 | 0.14 |
| Ti20Nb | 0.209 | 0.04 | 0.212 | 0.005 | 0.10 |

It is therefore highly probable that **there was no significant change of the shuffle in the Ti12Nb3O sample** compared to Ti12Nb2O or Ti12Nb1O, but **rather the suppression of certain variants of martensite** in the investigated parent β grain. It is therefore possible that when using method 1, the algorithm could not cope with fitting different volume fractions of the individual variants (as method 2 could). As a results, the fitting algorithm arbitrarily lowered the y parameter value and thus the high R-

factor value emerged. This hypothesis would need further verification, for example via EBSD technique.

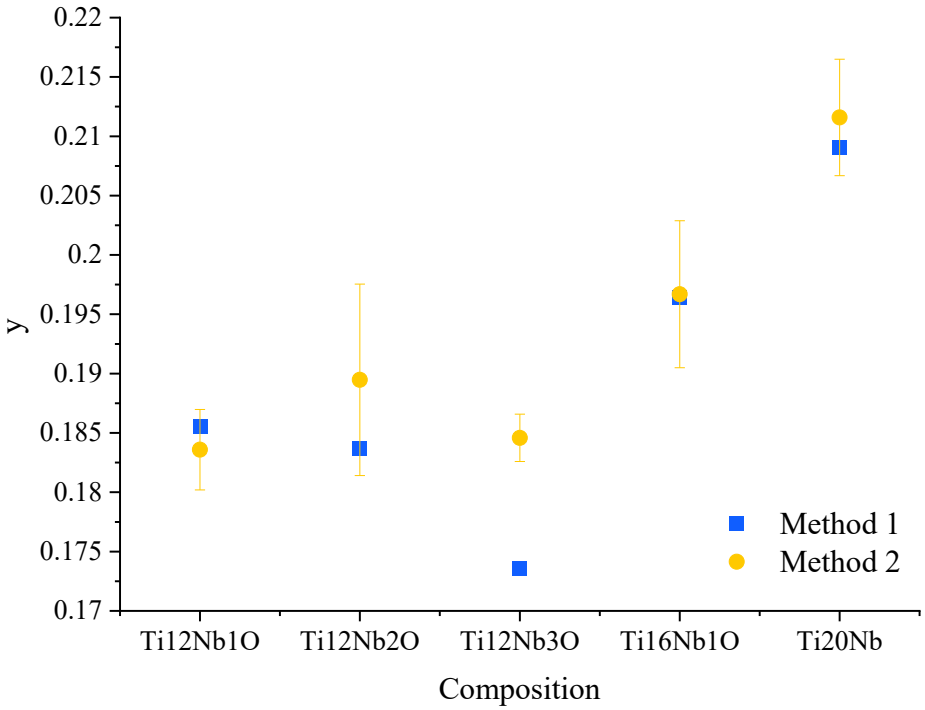


Figure 6-19 Graph showing the shuffle parameter y for the samples with different compositions. Values obtained by first and second method are presented by blue and yellow colour, respectively.

Finally, a comparison of the obtained y value for different samples is shown in Figure 6-19. Although the individual error bars are quite large, there is a clearly visible trend towards higher values of y for samples with a higher Nb concentration. Regarding the comparison of Ti-12Nb-1/2/3O samples, it appears that the values obtained by method 2 are the same within an error and the deviation from method 1 in case of Ti-12Nb-3O was already explained. To conclude this chapter, it seems that oxygen atoms don't change the crystal structure directly, but rather continuously suppress some variants depending on their orientation.

## 6.8 TEM measurement on Ti-20Nb-2O

According to the classical view on the effect of oxygen as an α stabilizing element, it should adequately increase the β transus temperature and $M_S$ temperature as well. In recent years, it has been found that this behaviour is not exactly correct and even though it was proved by measurement that oxygen really stabilize α phase and

increases the β transus temperature, this cannot be applied on the $M_S$ temperature. As we described in the theory, Oxygen atoms occupy octahedral sites inside both α and β phase, but due to lower stresses inside α phase it behaves like α stabilizing element. However, if we have an alloy with too much content of oxygen, the crystallographic change during quenching can be described as a strain-glass transition. Tensile stress acting on the atoms surrounded by oxygen causes can be relaxed by shuffle of adjacent $\{110\}_\beta$ planes in the $\langle 110\rangle_\beta$ directions (i.e., the shuffling process of the $\beta \rightarrow \alpha''$ martensitic transformation). Due to that shuffle will precedes the shear, differently oriented strains around shuffling planes (nanodomains) will partially or fully (this is still a debate in the literature [20,46,47]) suppress the $\{11\bar{2}\}\langle 111\rangle$ shear necessary for the change of lattice parameters.

Looking at the XRD profile of the samples with Ti-20Nb-0/2/3O composition, even though oxygen should normally favour the $\beta \rightarrow \alpha$ transition and increase the $M_S$ temperature, it really suppressed the formation of $\alpha''$ at 2.at % level of oxygen. At 3 at.% level, it even suppressed the formation of ω phase. To confirm whether above mentioned nanodomains are really the cause of anomalous behaviour in our samples, we prepared approximately 100 nm thick sample out of Ti-20Nb-2O alloy and performed TEM and HRTEM measurements. The results are presented in the following pages.

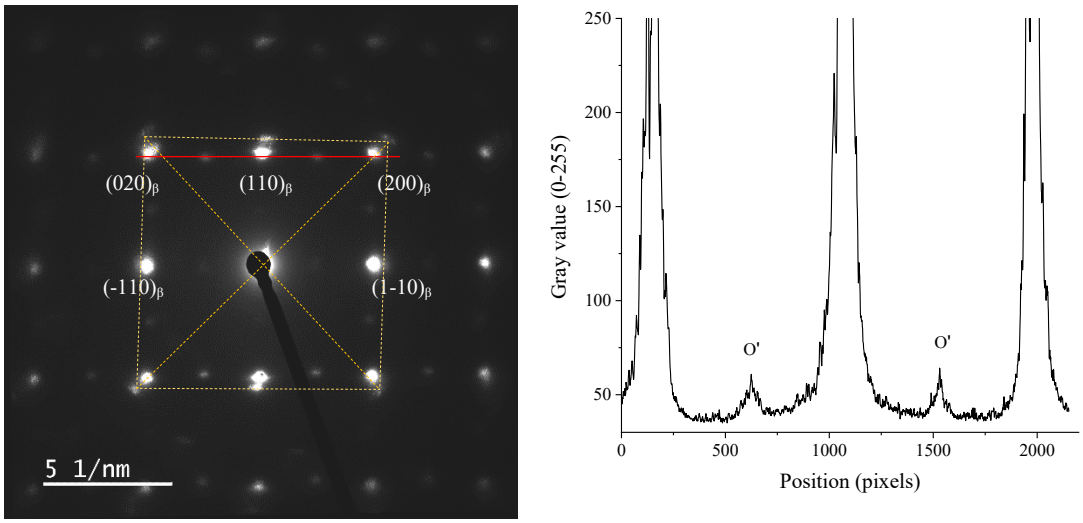


Figure 6-20. TEM Diffraction pattern of Ti-12Nb-2O sample acquired with the incident electron beam parallel to $[100]_\beta$ zone axis on the left. Gray value profile across the red line indicating the presence of O' phase is presented on the right.

As we can see from the diffraction pattern, the most intensive diffraction spots belong to the expected β phase oriented in the $[100]_\beta$ zone axis. The profile analysis along the red line at Figure 6-20 on the right clearly shows the presence of another peaks at positions perpendicular to $(1\bar{1}1)_\beta$ direction in the middle of β peaks. Exactly this structure was mentioned in the literature with peaks resulting from the shuffle of $\{110\}_\beta \langle 110\rangle_\beta$ type [20]. This phase has similar symmetry as α″ phase (both should belong to the Cmcm space group), but because the structure doesn't show a difference in $b$ and $c$ axis and follows $b_{O'} \approx c_{O'} = \sqrt{2}a_{O'}$, it is considered to be the O′ phase.

Other things that we can see from the diffraction pattern are very weak spots in the middle of the $(\bar{1}10)_\beta$ direction. Those peaks are most probably comming from the double diffraction, as we can see from the simulation pattern in Figure 6-22 made from the arrangement of atoms presented in Figure 6-21. Yellow spots represent the position of spots made by double diffraction. In the presented simulation, we considered one α″ modified in such a way that $b_{O'} \approx c_{O'} = \sqrt{2}a_{O'}$. The diffraction peaks lying above and under the $(\bar{1}11)_\beta$ peak perpendicular to the red line are considered to be just another variant of the same structure. Lastly, there are obviously some satellite peaks around β peaks. So far, we don't really know where those peaks are coming from. Whether they are just an error or a real structure within our sample would need further analysis, but the quick drawing of orange rectangle indicates the structure has different lattice parameters along both axes. The classical way to visualize different particles within the matrix is to perform dark field imaging. This method unfortunately was not that successful in our case, most probably because the particles are too small and do not diffract very well. Thus, it was not possible to reach the satisfactory signal to noise ratio. In the next part, we will take a closer look on another way how to directly visualize the O′ phase using the high-resolution transmission electron microscopy (HRTEM) technique.

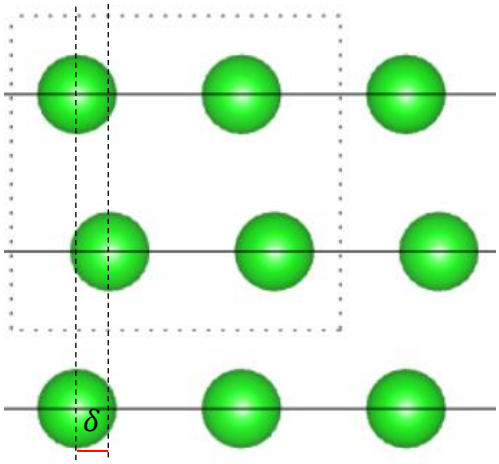


Figure 6-21 One of the $\{110\}_\beta \langle 110\rangle_\beta$ shuffles viewed from $[100]_{O'}$ axis. degree of shuffle is represented by $\delta$. Dotted rectangle is a unit cell of $\alpha''$ phase. Solid black lines coincide with parent β phase $\{110\}_\beta$ planes.

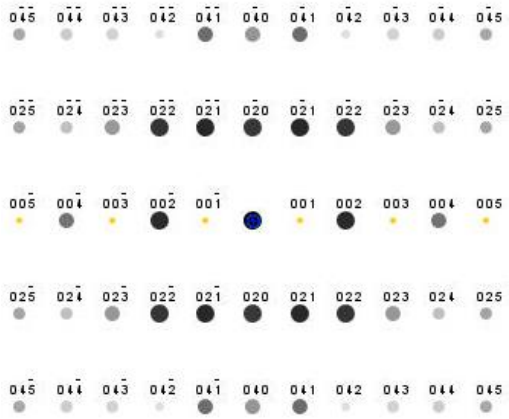

Figure 6-22. Simulated diffraction pattern of O′ phase with lattice parameters $b_{O'} \approx c_{O'} = \sqrt{2}a_{O'}$ and Wyckoff parameter of shuffle y=0.2. viewed from $[100]_{O'}$ zone axis. Black dots represent diffraction pattern, yellow dots are double diffraction

High resolution Transmission electron microscopy offers incredible way to visualize the crystal structure directly from the atomic columns. Using the magnification of 800k and more, we were able to take a real image of the structure which we are studying. One such HRTEM image can be seen in Figure **6-23**, acquired with the incident electron beam parallel to the $[100]_\beta$ direction in the parent β grain. Even though it is possible to distinguish individual atomic columns in some places, this resolution is not enough to really see the atomic shuffle presented in Figure 6-21. To really distinguish potential parts where the proposed shear could have happened, we performed Fast furrier transformation (FFT) of the picture to see whether we have some frequencies like those we got by pure diffraction. The resulting transformation is presented in the Figure **6-23**. There we can see weak diffraction spots at expected positions (encircled by red dots). Apart from this, we can also see regular β peaks at expected positions and again the satellite peaks at the edge of (002)β peaks along the diagonal.

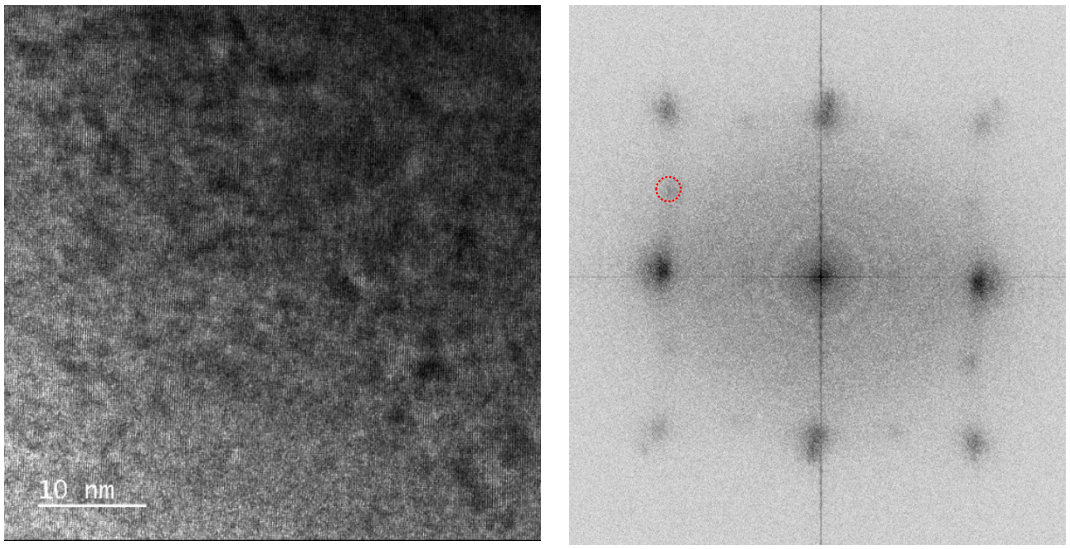


Figure 6-23. HRTEM image taken from $[100]_{\beta}$ zone axis (left). Colour inverted FFT transformation image with encircles diffraction spots coming from the O′ phase (right).

Using this Fourier transformation picture, we enhanced the intensity of the image in the region that corresponds to the diffraction coming from the O′ phase (in the red circle presented in the picture) and did the inverse flourier transformation. The picture generated by the IFFT algorithm and inverted (black region represent the potential O′ phase) is presented in Figure 6-24.

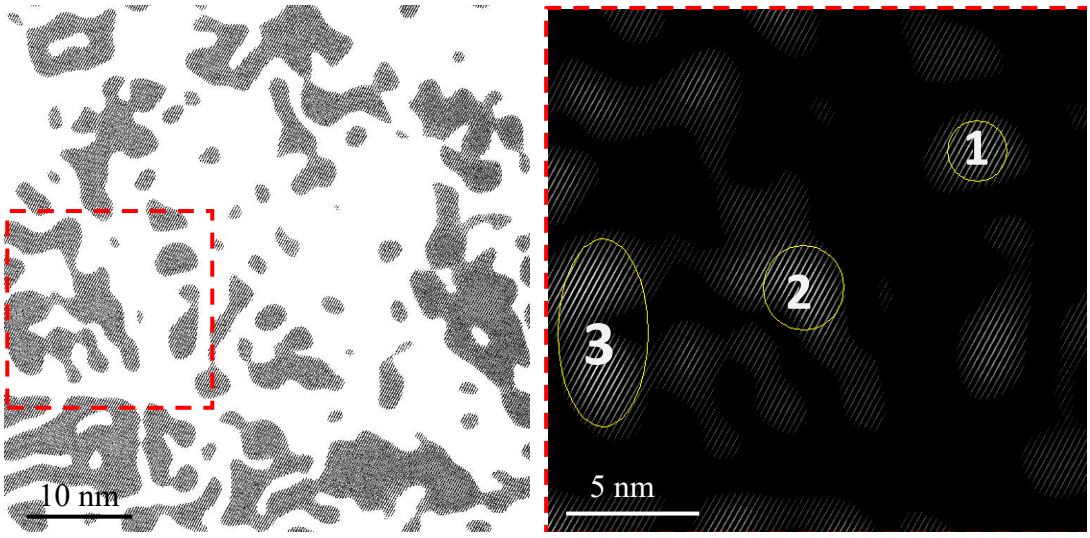


Figure 6-24 Resulting map generated by IFFT algorithm. Black regions on the left picture show potential regions where O′ phase should be present. On the right picture, we can see selected three particles which will be investigated further.

Due to results generated in Figure 6-24 are quite sensitive to the specific location of investigated point on FFT map and on the adjustment of brightness/contrast, We have decided to analyse three small particles generated by IFFT algorithm separately. All three particles were generated by IFFT algorithm the same way as the picture in Figure

6-24, but in this case we also considered the $\{110\}_{\beta}$ peaks. The results are presented in the Figure 6-25.

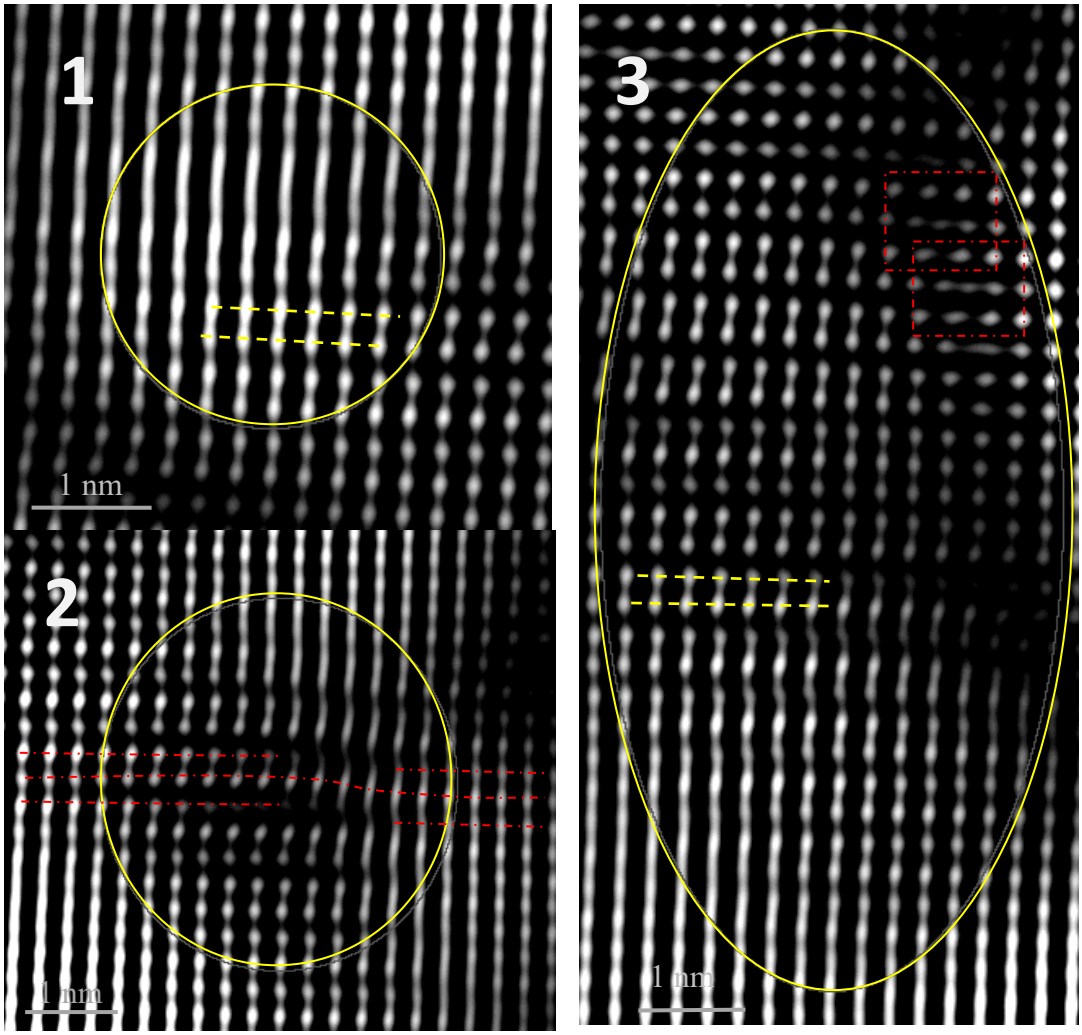


Figure 6-25 selected regions from figure 6-23 investigated by IFFT considering also $\{110\}_{\beta}$ diffraction points. 2 yellow lines represent shuffled atomic planes.

Looking at the pictures we can clearly resemble the proposed shuffle mechanism between two atomic planes, as depicted in Figure 6-21. The 1st particle shows the tweed like structure, where shuffle can be recognized as a deviation from the straight path. The second particle shows again some kind of shuffle, but in this case, it seems more like a distortion caused by the presence of dislocations or a missing atomic plane. As was mentioned in the theory, O′ can be viewed as a frozen strain within the sample made by strain glass transition. Finishing with the particle number 3, the clearest effect of shuffle mechanism can be seen here. Opposite atomic planes are not only shifted with respect to each other, but there is a clear tendency of the same

amount of shuffle on every other atomic plane. This is thus a clear proof of the shuffle mechanism inside this region viewed from the $[100]_\beta$ zone axis.

Apart from this, interesting feature can be seen when we look at the regions in the rectangle. This atomic arrangement is very similar to the structure known as crowdions. Surprisingly, we can see not only one but two, sitting happily next to each other. So far, we couldn't find any article mentioning this structure in titanium alloys. To reliably confirm or deny its existence in the structure would addition measurements. Nowadays, the technique mostly used for measuring such structures is the High-angle annular dark-field scanning transmission electron microscopy, which can offer much better resolution compared to conventional HRTEM.

# 7 Final discussion

Based on the qualitative results obtained from the measurement of oxygen-free samples, we can clearly state that the crystal structure of the orthorhombic phase changes smoothly from cubic to hexagonal with a gradual decrease in niobium concentration. From a crystallographic point of view, This is a clear proof that the metastable orthorhombic phase is an intermediate phase between the stable hcp and bcc phases, as was also observed in [48].

Considering the Ti-16Nb-2/3O samples where both α″ and β phases were present, it was found that the mechanism of transformation of lattice parameters based on gradual shear does not fully reflect the actual process of the transformation. Since the mutual distance of the $\{112\}_\beta$ planes the β structure changes, the right angle between $[100]_\beta$ and $[011]_\beta$ directions remains constant and the structure obviously elongates along the $[111]_\beta$ direction, there must be some another mechanism (or a combination of them) which would include these 2 important changes. We therefore present a new method of transformation, which is based on the old $\{11\bar{2}\}\langle 111\rangle_\beta$ shear [47] supplemented by compression in the $[11\bar{2}]_\beta$ direction and a homogeneous (in the corresponding $\{110\}_\beta$ planes) change in volume, thanks to which a structure change along the $[111]_\beta$ diagonal could occur.

In the samples with a gradually increasing oxygen content, it is possible to notice the suppressing effect on both the β → ω transformation and the β → α″

transformation. In the case of martensite suppression, at a low niobium content, the beta structure seems to be unstable (Ti16Nb2O) and often transforms into the omega phase. However, with further increase in the oxygen concentration, the omega phase is suppressed, as observed in the Ti20Nb2/3O samples. This is a clear proof that O has a general tendency to supress both ω and α″, what is in a good agreement with the literature [20,37].

Speaking more about lattice parameters, we were not able to observe any significant influence of oxygen on the crystal structure of martensite either by means of a simple analysis of the lattice parameters or by studying the atomic positions within the unit cell. However, We indirectly observed from our simulation that the sample with higher oxygen concentration (Ti12Nb3O) has some variants of martensite suppressed more than other and their volume fraction is inhomogeneous. **This behaviour indicates that oxygen is not similar to Nb, which continuously changes the structure from one phase to another, but rather acts like a point defect which creates stress field around**, as was proposed in the literature about strain glass transition [35]**.** These stress fields further suppress the potential formation of other structures that are dependent on long-range transformation, such as the martensitic phase. This idea is also with a good agreement when considering the effect on nanosized ω phase. Due to athermal ω particles are much smaller than martensite, it is harder for the oxygen atoms to fully suppress them as they usually do not grow into macroscale dimensions.

The crystal structure analysis of the $\{110\}_\beta \langle 110\rangle_\beta$ shuffle showed the expected results in case of samples with increasing content of Nb. As presented at the graph, The y parameter increases with increasing content of Nb. This is with a good agreement with shuffle mechanism, where higher values of y correspond to the structure closer to β phase.

Measurements on the samples with a constant fraction of niobium and varying amounts of oxygen show almost no changes. In the case of different oxygen concentrations, the change between the individual samples was at the level of 0.005, which corresponds to a shift around 0.015 Å. Compared to the diameter of an titanium atom, which is approximately 3 Å, this number corresponds to a shift of less than 1%

of its own size. Thus, despite the relatively huge error bars, we can reliably say that oxygen did not cause any significant change in the investigated samples and its effect will probably not be linear, as in the case of niobium, but rather immediate, as the theory of glass transition proposes.

On the other hand, 4 at. % of niobium caused a measurable change at the level of 0.015, what in turn corresponds to a shift of 1.5% of its own size. It is quite fascinating that we were able to detect such a small shift. To put it more quantitatively, If we would assume a linear effect of niobium on atomic shuffle, then 1 at.% increase of Nb would cause $0.15/4 = 0.00375$ change in shuffle. By comparing the threshold values of hcp and bcc structures, a simple calculation can give us the necessary amount of Nb for the transition from one structure to another. In this case, it would be around

$$\frac{\frac{1}{4}-\frac{1}{6}}{0.00375}\ \text{at.}\,\% \approx 22\ \text{at.}\,\%\ .$$

To conclude this calculation, it is quite unusual how close this number is to the value we obtained when calculating similar value from the lattice parameters (just to remind, $\frac{(\sqrt{3}-\sqrt{2})}{0.0144} \approx 22$ at.%). Whether this equality is a pure coincidence or not would require a deeper analysis, but the interconnection between these two mechanisms (shear and shuffle) seems to be at a much higher level than it might appear at the first glance.

# 8 Conclusion

In the presented work, we investigated the effect of niobium and oxygen on crystal structure of the martensitic phase in titanium alloys based on Ti, Nb and O. A total of 15 samples with a composition in the range of Ti-(8-28)Nb-(0-3)O at.% were produced by arc melting and then solution treated and water-quenched. X-ray diffraction was performed on the all the samples. In alloys that contained only α″ phase we also performed quantitative analysis of atomic positions via X ray diffraction. The final results can be summarized in several points:

- XRD measurements showed that oxygen suppresses both ω and α″ phase in investigated samples.

- XRD of oxygen free samples revealed the continuous change of the lattice parameter of α″ phase with the change of Nb concentration.
- SEM and XRD measurements showed that α″ and β phase may coexist, but their lattice parameters Do not follow the geometry of $\{11\bar{2}\}\langle 111\rangle_{\beta}$ shear only, but also change in $\langle 111\rangle_{\beta}$ direction and compress in the $\{11\bar{2}\}_{\beta}$ planes.
- EBSD measurement of Ti-12Nb-1O sample revealed the martensitic twins within the sample and reconstruction of parent β phase reveals that all observed α″ laths follow the common orientation relations.
- Atomic shuffle $\{110\}_{\beta}\langle 110\rangle_{\beta}$ seems to be enhanced by oxygen atoms in α″ free samples as viewed from HRTEM images processed by FFT/IFFT.
- Investigated crystal structure of α″ martensite doesn't show any significant change with increasing oxygen content - neither a change in lattice parameters nor a shift of atomic planes.
- Investigated crystal structure of α″ martensite shows continuous change in $\{110\}_{\beta}\langle 110\rangle_{\beta}$ atomic shuffle with increasing Nb content. This shuffle seems to be deeply connected with atomic shear.

# 9 Bibliography


[1] Veiga C, Davim J and Loureiro A 2012 Properties and applications of titanium alloys: A brief review *Reviews on Advanced Materials Science* **32** 133–48

[2] Lütjering G and Williams J C 2007 *Titanium* (Berlin Heidelberg: Springer-Verlag)

[3] Greenwood N N Chemistry of the Elements - 2nd Edition

[4] Hudon G and Filippou D 2020 Chapter 4 - Chemical processes for the production of titanium tetrachloride as precursor of titanium metal *Extractive Metallurgy of Titanium* ed Z Z Fang, F H Froes and Y Zhang (Elsevier) pp 47–62

[5] Agripa H, Botef I, Agripa H and Botef I 2019 *Modern Production Methods for Titanium Alloys: A Review* (IntechOpen)

[6] Suzuki R O, Ono K and Teranuma K 2003 Calciothermic reduction of titanium oxide and in-situ electrolysis in molten CaCl2 *Metall Mater Trans B* **34** 287–95

[7] Banerjee S Phase Transformations, Volume 12 - 1st Edition

[8] Bania P J 1994 Beta titanium alloys and their role in the titanium industry *JOM* **46** 16–9

[9] Cotton J D, Briggs R D, Boyer R R, Tamirisakandala S, Russo P, Shchetnikov N and Fanning J C 2015 State of the Art in Beta Titanium Alloys for Airframe Applications *JOM* **67** 1281–303

[10] Kolli R P and Devaraj A 2018 A Review of Metastable Beta Titanium Alloys *Metals* **8** 506

[11] Stráský J, Preisler D, Seiner H, Bodnárová L, Janovská M, Košutová T, Harcuba P, Šalata K, Halmešová K, Džugan J and Janeček M 2022 Achieving high strength and low elastic modulus in interstitial biomedical Ti–Nb–Zr–O alloys through compositional optimization *Materials Science and Engineering: A* **839** 142833

[12] Williams J C and Blackburn M J THE INFLUENCE OF MISFIT ON THE MORPHOLOGY AND STABILITY OF THE OMEGA PHASE IN TITANIUM--TRANSITION METAL ALLOYS. (Journal Article) | OSTI.GOV

[13] Banerjee D and Williams J C 2013 Perspectives on Titanium Science and Technology *Acta Materialia* **61** 844

[14] Danard Y, Sun F, Gloriant T, Freiherr Von Thüngen I, Piellard M and Prima F 2020 The Influence of Twinning on the Strain–Hardenability in TRIP/TWIP Titanium Alloys: Role of Solute–Solution Strengthening *Frontiers in Materials* **7**

[15] Ballor J, Li T, Prima F, Boehlert C J and Devaraj A 2023 A review of the metastable omega phase in beta titanium alloys: the phase transformation mechanisms and its effect on mechanical properties *International Materials Reviews* **68** 26–45

[16] Ivasishin O M, Markovsky P E, Semiatin S L and Ward C H 2005 Aging response of coarse- and fine-grained β titanium alloys *Materials Science and Engineering: A* **405** 296–305

[17] Tahara M, Hasunuma K and Hosoda H 2021 Microstructure of α + β dual phase formed from isothermal α″phase via novel decomposition pathway in metastable β-Ti alloy *Journal of Alloys and Compounds* **868** 159237

[18] Bendersky L A, Roytburd A and Boettinger W J 1994 Phase transformations in the (Ti, Al)3 Nb section of the Ti□Al□Nb system—I. Microstructural predictions based on a subgroup relation between phases *Acta Metallurgica et Materialia* **42** 2323–35

[19] De Fontaine D, Paton N E and Williams J C 1971 The omega phase transformation in titanium alloys as an example of displacement controlled reactions *Acta Metallurgica* **19** 1153–62

[20] Zheng Y and Fraser H L 2016 A nano-scale instability in the β phase of dilute Ti–Mo alloys *Scripta Materialia* **116** 131–4

[21] Nejezchlebová J, Janovská M, Seiner H, Sedlák P, Landa M, Šmilauerová J, Stráský J, Harcuba P and Janeček M 2016 The effect of athermal and isothermal ω phase particles on elasticity of β-Ti single crystals *Acta Materialia* **110** 185–91

[22] Šmilauerová J, Harcuba P, Stráský J, Stráská J, Janeček M, Pospíšil J, Kužel R, Brunátová T, Holý V and Ilavský J 2014 Ordered array of ω particles in β-Ti matrix studied by small-angle X-ray scattering *Acta Materialia* **81** 71–82

[23] Collings E W 1994 *Materials Properties Handbook: Titanium Alloys* (ASM International)

[24] Ouyang P, Mi G, Li P, He L, Cao J and Huang X 2018 Non-Isothermal Oxidation Behavior and Mechanism of a High Temperature Near-α Titanium Alloy *Materials* **11** 2141

[25] Rosa C J 1970 Oxygen diffusion in alpha and beta titanium in the temperature range of 932° to 1142°C *Metall Mater Trans B* **1** 2517–22

[26] Cai Z, Cheng X, Chen J, Xiang T and Xie G 2022 Optimized mechanical properties of titanium-oxygen alloys by powder metallurgy *Journal of Materials Research and Technology* **21** 4151–63

[27] Geng F, Niinomi M and Nakai M 2011 Observation of yielding and strain hardening in a titanium alloy having high oxygen content *Materials Science and Engineering: A* **528** 5435–45

[28] Catanio Bortolan C, Contri Campanelli L, Paternoster C, Giguère N, Brodusch N, Bolfarini C, Gauvin R, Mengucci P, Barucca G and Mantovani D 2021 Effect of oxygen content on the mechanical properties and plastic deformation mechanisms in the TWIP/TRIP Ti–12Mo alloy *Materials Science and Engineering: A* **817** 141346

[29] Tane M, Nakano T, Kuramoto S, Niinomi M, Takesue N and Nakajima H 2013 ω Transformation in cold-worked Ti–Nb–Ta–Zr–O alloys with low body-centered cubic phase stability and its correlation with their elastic properties *Acta Materialia* **61** 139–50

[30] Yan M, Xu W, Dargusch M S, Tang H P, Brandt M and Qian M 2014 Review of effect of oxygen on room temperature ductility of titanium and titanium alloys *Powder Metallurgy* **57** 251–7

[31] Kuramoto S, Furuta T, Hwang J, Nishino K and Saito T 2006 Elastic properties of Gum Metal *Materials Science and Engineering: A* **442** 454–7

[32] Kim H Y, Wei L, Kobayashi S, Tahara M and Miyazaki S 2013 Nanodomain structure and its effect on abnormal thermal expansion behavior of a Ti–23Nb–2Zr–0.7Ta–1.2O alloy *Acta Materialia* **61** 4874–86

[33] Tane M, Nakano T, Kuramoto S, Hara M, Niinomi M, Takesue N, Yano T and Nakajima H 2011 Low Young's modulus in Ti–Nb–Ta–Zr–O alloys: Cold working and oxygen effects *Acta Materialia* **59** 6975–88

[34] Tahara M, Kim H Y, Inamura T, Hosoda H and Miyazaki S 2011 Lattice modulation and superelasticity in oxygen-added β-Ti alloys *Acta Materialia* **59** 6208–18

[35] Zhang K, Wang K, Fu Y, Xiao W, Han J and Zhao X 2022 Strain glass transition in a metastable β Ti-Nb-O alloy with high oxygen content *Scripta Materialia* **214** 114661

[36] Sarkar S, Ren X and Otsuka K 2005 Evidence for Strain Glass in the Ferroelastic-Martensitic System Ti 50 − x Ni 50 + x *Phys. Rev. Lett.* **95** 205702

[37] Tahara M, Inamura T, Kim H Y, Miyazaki S and Hosoda H 2016 Role of oxygen atoms in α″ martensite of Ti-20at.% Nb alloy *Scripta Materialia* **112** 15–8

[38] Ren X 2014 Strain glass and ferroic glass – Unusual properties from glassy nano-domains *physica status solidi (b)* **251** 1982–92

[39] Huang Y-C, Tsao C-S and Wu S-K 2020 Structural evolution and mechanism of strain glass transition in Ti48.7Ni51.3 shape memory alloy studied by anomalous small-angle X-ray scattering *Sci Rep* **10** 9402

[40] Anon Electron Backscatter Diffraction : EBSD | Techniques | Fields | Toray Research Center | TORAY

[41] Václav V, Milena P and Pavel L Kniha Základy strukturní analýzy

[42] Arndt U W and Willis B T M 1966 *Single Crystal Diffractometry* (Cambridge: Cambridge University Press)

[43] Brown P J, Fox A G, Maslen E N, O'Keefe M A and Willis B T M 2006 Intensity of diffracted intensities *International Tables for Crystallography* (John Wiley & Sons, Ltd) pp 554–95

[44] Brown A R G and Clark D The Titanium–Niobium System | Nature

[45] Anon R factor - Online Dictionary of Crystallography

[46] Obbard E G, Hao Y L, Talling R J, Li S J, Zhang Y W, Dye D and Yang R 2011 The effect of oxygen on α″ martensite and superelasticity in Ti–24Nb–4Zr–8Sn *Acta Materialia* **59** 112–25

[47] Zheng Y, Banerjee R, Wang Y, Fraser H and Banerjee D 2022 Pathways to Titanium Martensite *Trans Indian Inst Met* **75** 1051–68

[48] Banumathy S, Mandal R K and Singh A K 2009 Structure of orthorhombic martensitic phase in binary Ti–Nb alloys *Journal of Applied Physics* **106** 093518

# List of tables



# List of figures

# List of acronyms

| | |
|---|---|
| bcc | Body centered cubic structure |
| hcp | Hexagonal closed packer structure |
| MS | Martensite start temperature |
| XRD | X-ray diffraction |
| SEM | Scanning electron microscopy |
| SE | Secondary electrons |
| BSE | Back scattered electrons |
| EBSD | Electron back scattered diffraction |
| TEM | Transmission electron microscopy |
| HRTEM | High resolution transmission electron microscopy |
| FFT | Fast Fourier transformation |
| IFFT | Inverse fast Fourier transformation |
| PTMC | The Phenomenological Theory of Martensite Crystallography |

# Appendix

This part of appendix shows a detailed look on a difference between the observed and calculated structure factors for individual samples calculated by method 1.

| $\lvert F_{hkl}^{obs}\rvert$ | $\lvert F_{hkl}^{the}\rvert$ | $\sigma$ | $h$ | $k$ | $l$ | $\left\lvert \lvert F_{hkl}^{obs}\rvert - \lvert F_{hkl}^{the}\rvert \right\rvert$ |
|---|---|---|---|---|---|---|
| 25.93 | 24.32 | 4.57 | 1 | 1 | 0 | 1.61 |
| 42.40 | 41.42 | 8.04 | 0 | 2 | 0 | 0.98 |
| 45.01 | 51.26 | 1.15 | 1 | 1 | 1 | 6.26 |
| 36.44 | 39.38 | 7.44 | 0 | 2 | 1 | 2.94 |
| 41.40 | 34.82 | 7.94 | 2 | 0 | 0 | 6.58 |
| 27.83 | 30.61 | 6.30 | 1 | 3 | 0 | 2.78 |
| 10.44 | 10.49 | 2.26 | 1 | 3 | 1 | 0.05 |
| 28.87 | 25.71 | 11.00 | 1 | 1 | 3 | 3.17 |
| 22.99 | 19.85 | 4.34 | 0 | 2 | 3 | 3.13 |
| 18.14 | 18.14 | 5.61 | 2 | 2 | 0 | $< 0.01$ |
| 16.13 | 25.38 | 5.76 | 2 | 0 | 2 | 9.25 |
| 22.42 | 22.42 | 4.79 | 1 | 3 | 2 | $< 0.01$ |
| 25.40 | 22.54 | 4.86 | 0 | 4 | 1 | 2.86 |
| 16.14 | 13.51 | 3.93 | 2 | 2 | 2 | 2.63 |
| 2.97 | 5.39 | – | 3 | 1 | 0 | 2.42 |
| $y = 0.185$ | | $I_0 = 192.09$ | | Ti-12Nb-1O | | R = 0.12 |

| $\lvert F_{hkl}^{obs}\rvert$ | $\lvert F_{hkl}^{the}\rvert$ | $\sigma$ | $h$ | $k$ | $l$ | $\left\lvert \lvert F_{hkl}^{obs}\rvert - \lvert F_{hkl}^{the}\rvert \right\rvert$ |
|---|---|---|---|---|---|---|
| 27.38 | 25.55 | 6.27 | 1 | 1 | 0 | 1.83 |
| 42.00 | 41.34 | 11.35 | 0 | 2 | 0 | 0.65 |
| 45.07 | 52.61 | 2.83 | 1 | 1 | 1 | 7.54 |
| 41.50 | 41.50 | 9.40 | 0 | 2 | 1 | $< 0.01$ |
| 17.24 | 18.10 | 3.68 | 1 | 1 | 2 | 0.86 |
| 31.37 | 33.77 | 7.91 | 1 | 3 | 0 | 2.40 |
| 37.64 | 28.61 | – | 1 | 1 | 3 | 9.02 |
| 22.73 | 22.73 | 4.47 | 0 | 2 | 3 | $< 0.01$ |
| 19.70 | 19.99 | 2.01 | 2 | 2 | 0 | 0.29 |
| 27.29 | 28.88 | 4.94 | 2 | 0 | 2 | 1.59 |
| 21.65 | 20.65 | 5.93 | 2 | 2 | 1 | 1.00 |
| 26.54 | 26.00 | 10.31 | 1 | 3 | 2 | 0.54 |
| 22.82 | 25.94 | 6.09 | 0 | 4 | 1 | 3.12 |
| 15.74 | 15.73 | 2.78 | 2 | 2 | 2 | 0.01 |
| 2.09 | 2.09 | – | 0 | 4 | 2 | $< 0.01$ |
| 23.06 | 13.33 | 21.75 | 2 | 2 | 3 | 9.73 |
| $y = 0.184$ | | $I_0 = 204.68$ | | Ti-12Nb-2O | | R = 0.09 |

| $\lvert F_{hkl}^{obs}\rvert$ $\lvert F_{hkl}^{obs}\rvert$ | $\lvert F_{hkl}^{the}\rvert$ | $\sigma$ | $h$ | $k$ | $l$ | $\left\lvert \lvert F_{hkl}^{obs}\rvert - \lvert F_{hkl}^{the}\rvert \right\rvert$ |
|---|---|---|---|---|---|---|
| 45.95 | 27.57 | 75.46 | 1 | 1 | 0 | 18.38 |
| 33.16 | 33.16 | 4.49 | 0 | 2 | 0 | 0.00 |
| 40.66 | 47.34 | 4.94 | 1 | 1 | 1 | 6.68 |
| 34.98 | 42.50 | 10.08 | 0 | 2 | 1 | 7.52 |
| 16.88 | 18.14 | 6.69 | 1 | 1 | 2 | 1.25 |
| 30.89 | 31.59 | – | 2 | 0 | 0 | 0.70 |
| 28.09 | 29.10 | 10.68 | 1 | 3 | 0 | 1.02 |
| 35.69 | 21.97 | – | 1 | 1 | 3 | 13.72 |
| 18.60 | 19.83 | 5.69 | 0 | 2 | 3 | 1.23 |
| 19.89 | 17.35 | 4.95 | 2 | 2 | 1 | 2.54 |
| 23.11 | 18.18 | 6.50 | 0 | 4 | 1 | 4.94 |
| 16.07 | 9.48 | 6.58 | 2 | 2 | 2 | 6.59 |
| 10.56 | 9.21 | 3.71 | 2 | 2 | 3 | 1.34 |
| $y = 0.174$ | | $I_0 = 192.13$ | | Ti-12Nb-3O | | R = 0.19 |

| $\lvert F_{hkl}^{obs}\rvert$ | $\lvert F_{hkl}^{calc}\rvert$ | $\sigma$ | $h$ | $k$ | $l$ | $\left\lvert \lvert F_{hkl}^{obs}\rvert - \lvert F_{hkl}^{cal}\rvert \right\rvert$ |
|---|---|---|---|---|---|---|
| 20.06 | 20.19 | 2.77 | 1 | 1 | 0 | 0.13 |
| 44.65 | 46.38 | 8.81 | 0 | 2 | 0 | 1.74 |
| 30.52 | 33.07 | 4.23 | 0 | 2 | 1 | 2.55 |
| 35.31 | 30.46 | 0.00 | 0 | 2 | 2 | 4.85 |
| 30.17 | 32.05 | 4.48 | 2 | 0 | 0 | 1.88 |
| 14.98 | 14.45 | 2.22 | 1 | 3 | 1 | 0.53 |
| 46.97 | 23.60 | – | 1 | 1 | 3 | 23.37 |
| 14.72 | 15.21 | 2.40 | 0 | 2 | 3 | 0.49 |
| 15.20 | 18.15 | 5.26 | 2 | 2 | 0 | 2.95 |
| 16.82 | 13.26 | 8.70 | 2 | 2 | 1 | 3.57 |
| 19.76 | 17.61 | 3.13 | 1 | 3 | 2 | 2.15 |
| 19.68 | 18.91 | 4.85 | 0 | 4 | 1 | 0.77 |
| 18.33 | 12.91 | 1.39 | 2 | 2 | 2 | 5.43 |
| 8.51 | 7.31 | 0.00 | 1 | 3 | 3 | 1.19 |
| 10.70 | 6.89 | 3.76 | 2 | 2 | 3 | 3.81 |
| $y = 0.196$ | | $I_0 = 192.14$ | | Ti-16Nb-1O | | R = 0.16 |

Table 8 detailed look on parameters obtained by fitting individual variant separately – method 2.

| Sample | Parameter | Variant | | | | | | | | | | Average | $\sigma$ |
|---|---|---|---|---|---|---|---|---|---|---|---|---|---|
| | | 1 | 2 | 3 | 4 | 5 | 6 | 7 | 8 | 9 | 10 | | |
| Ti20Nb | y | 0.207 | 0.212 | 0.209 | 0.211 | 0.210 | 0.206 | 0.208 | 0.212 | 0.222 | 0.218 | 0.212 | 0.005 |
| | I | 203 | 192 | 192 | 203 | 192 | 192 | 210 | 174 | 192 | 296 | 205 | 33 |
| | R – factor | 0.11 | 0.11 | 0.10 | 0.14 | 0.11 | 0.10 | 0.06 | 0.14 | 0.05 | 0.11 | 0.10 | 0.03 |
| Ti12Nb1O | y | 0.180 | 0.183 | 0.184 | 0.181 | 0.180 | 0.179 | 0.187 | 0.188 | 0.187 | 0.187 | 0.184 | 0.003 |
| | I | 127 | 261 | 117 | 192 | 218 | 192 | 143 | 192 | 287 | 100 | 183 | 62 |
| | R – factor | 0.21 | 0.09 | 0.16 | 0.13 | 0.11 | 0.44 | 0.09 | 0.11 | 0.08 | 0.13 | 0.16 | 0.11 |
| Ti12Nb2O | y | 0.192 | 0.188 | 0.181 | 0.186 | 0.209 | 0.195 | 0.187 | 0.181 | 0.189 | 0.187 | 0.189 | 0.008 |
| | I | 370 | 355 | 287 | 164 | 201 | 323 | 306 | 262 | 128 | 132 | 253 | 91 |
| | R – factor | 0.01 | 0.13 | 0.06 | 0.14 | 0.30 | 0.10 | 0.14 | 0.09 | 0.07 | 0.13 | 0.12 | 0.08 |
| Ti12Nb3O | y | 0.187 | 0.185 | 0.184 | 0.186 | 0.185 | 0.181 | 0.181 | 0.185 | 0.185 | 0.187 | 0.185 | 0.002 |
| | I | 145 | 100 | 174 | 400 | 107 | 192 | 192 | 100 | 144 | 378 | 193 | 109 |
| | R – factor | 0.10 | 0.12 | 0.10 | 0.17 | 0.15 | 0.19 | 0.09 | 0.13 | 0.14 | 0.07 | 0.13 | 0.04 |
| Ti16Nb1O | y | 0.196 | 0.205 | 0.188 | 0.196 | 0.190 | 0.195 | 0.208 | 0.192 | 0.199 | 0.196 | 0.197 | 0.006 |
| | I | 220 | 192 | 141 | 234 | 294 | 192 | 192 | 121 | 219 | 252 | 206 | 51 |
| | R – factor | 0.10 | 0.24 | 0.22 | 0.08 | 0.09 | 0.23 | 0.19 | 0.07 | 0.12 | 0.09 | 0.14 | 0.07 |

Table 9. Lattice parameters of α″ phase determined from integrated profile obtained by XRD.

| Nb [Å] | O [Å] | a [Å] | $\sigma_a$ | b [Å] | $\sigma_b$ | c [Å] | $\sigma_c$ | b/a |
|---|---|---|---|---|---|---|---|---|
| 8 | 0 | 2.964 | 0.002 | 5.068 | 0.003 | 4.687 | 0.003 | 1.710 |
| 12 | 0 | 3.047 | 0.002 | 4.999 | 0.003 | 4.679 | 0.004 | 1.641 |
| 12 | 1 | 3.034 | 0.001 | 4.988 | 0.002 | 4.683 | 0.002 | 1.644 |
| 12 | 2 | 3.039 | 0.001 | 4.976 | 0.002 | 4.686 | 0.002 | 1.637 |
| 12 | 3 | 3.041 | 0.001 | 4.995 | 0.002 | 4.703 | 0.002 | 1.643 |
| 16 | 0 | 3.103 | 0.002 | 4.935 | 0.003 | 4.663 | 0.003 | 1.590 |
| 16 | 1 | 3.084 | 0.001 | 4.915 | 0.002 | 4.651 | 0.001 | 1.594 |
| 16 | 2 | 3.134 | 0.004 | 4.891 | 0.007 | 4.647 | 0.013 | 1.561 |
| 16 | 3 | 3.115 | 0.004 | 4.888 | 0.007 | 4.680 | 0.011 | 1.569 |
| 20 | 0 | 3.160 | 0.002 | 4.850 | 0.002 | 4.650 | 0.003 | 1.535 |